Universitá degli Studi di Napoli "Federico II"

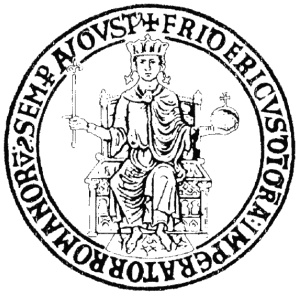

Dottorato di Ricerca in

Fisica Fondamentale ed Applicata

– XXII ciclo –

A.A. 2008/2009

The Observational Signatures of Cosmic Strings

Giuseppe Riccio

Coordinator
Prof. L. Marrucci

Supervisors
Prof. G. Longo
Prof. M.V. Sazhin

Dedication

to my beloved wife Assia

Acknowledgements

When this kind of event happens, one would thank the whole world...

I restrict myself to few people; they helped me to grow up, both as scientist and, above all, as man.

First of all, thanks to Peppe Longo: by following his lead, I have learnt what working and researching mean...

Thanks to prof. Sazhin, who welcomed me with open arms in this new adventure with cosmic strings, and to Olga, for her helpfulness when I was in Moscow...

I acknowledge the S.Co.P.E. project and its director prof. L. Merola, for allowing me to use such powerful computing facility...

Thanks to Giancarlo, always ready to help me about everything for more than ten years...

Thanks to Alfonso and Mauro, because they are what they are...

Thanks to Raffaele and Omar, because they introduced me in the data mining world and... teached me how making queries is boring...

Thanks to my family, because they let me become a man by pursuing my dreams and without imposing their own...

But mainly I would like to thank my beloved Assia. In these 3 years we lived a lot of experiences together, fulfilling the dream of creating a family too. She is always by my side, until she broke her foot to stay closer and closer to me...

Giuseppe Riccio
Napoli
January 13, 2010

Contents

List of Tables

List of Figures

Chapter 1

Introduction

Cosmic strings were postulated by Kibble in 1976 [1] as a special kind of topological defects of space-time and immediately became a hot issue in both theoretical physics and cosmology [2], [3]. In short, it can be stated that cosmic strings are infinitely long and filamentary remnants of primordial dark energy which formed in the early Universe and were then stretched by the cosmological expansion up to the point that, at present epoch, some cosmic string could cross the entire length of our observable Universe. With respect to other topological defects (such as domain walls, monopoles, textures, [4]), cosmic strings find their natural explanation in the inflationary scenario and are predicted by a wide class of elementary particle models. For instance, in the superstring theory (both in the compactification models and in theories with extended additional dimensions) cosmic strings arise as a natural consequence. While all theories predict for cosmic strings (either classical strings, or F- and D-strings; see chapter 5) an extremely long cosmological length and a negligibly small cross-section, other parameters (e.g. the linear density) strongly depend on the underlying model and can vary over a wide range [5, 6]. The detection of a cosmic strings would therefore allow to disentangle the true underlying theoretical framework and to extend our experimental knowledge in the GUT energy domain which is unavailable to modern and foreseen particle accelerators (i.e. $10^{14} - 10^{16}$ GeV). It would also allow to confirm on experimental grounds some of key points of inflation theory.

However, from the observational point of view, there are no evidences proving or disproving the existence of cosmic strings even though much work has been done and still is in progress to better defain, constrain and eventually detect their observable signatures.

One of the first predictions is that topological defects can influence the Cosmic Microwave Background (CMB) anisotropy. According to the Wilkinson Microwave Anisotropy Probe (WMAP) 5-years data [7] however, cosmic strings are not a primary source of primordial density perturbations and they are not responsible for the formation of cosmic structures. This negative result puts strong constrains on the density of string, setting it to a very small value (2$\sim$3 in the entire universe). It needs to be stressed, however, that these results were obtained from extensive multiparameter computer simulations of string networks and not from simulations of indivisual strings, as it is instead

the main goal of the present work.

Modern methods for cosmic string detection can be divided in three main types:

- Detection through gravitational lensing effects. These technique is based on extensive use of optical surveys;
- Detection through the signatures left by cosmic strings on the CMB anisotropy;
- Detection of model dependent and rare features such as, for instance, the gravitational radiation from string loops and from straight string, the interactions of strings with black holes, the decay of heavy particles emitted by string, the interaction of two strings etc [4].

The superstring theory allows for the existence of cosmic strings over a wide range of their parameters: density (varying from the scale of electroweak unification to GUT scales), velocity (from zero to the speed of light), geometry (from straight to loop like). All strings, however, share two properties which are model independent: an extremely long cosmological length and a negligibly small cross-section. As we shall see in the next chapters, the investigation of the structure of the CMB anisotropy and the search for gravitational lensing events induced by cosmic strings are so attractive because these effects should exist for all the theoretically possible cosmic strings.

Gravitational lensing events induced by strings are extremely peculiar and easy to identify. A first effect is produced by an intervening string along the line of sight which splits in two components (double images) faint background galaxies, thus forming a chain of lensed galaxies along the path of the string. Since the theory predicts that strings can be very far from the observer, very deep, multiband, whole sky (or at least with very large coverage) galaxy surveys of great photometric accuracy are needed to maximize the detection probability. Depth is required in order to push the search out to high redshift regimes ($z > 1.5$) while accurate photometry in the various band is required in order to minimize the contamination in the catalogues of candidate pairs of lensed images (which are selected by constraining the flux ratios in different bands, see [8]. Furthermore since the average distance of this multiple images will be of the order of the deficit angle (see chapter 5) of the cosmic strings, a good angular resolution and a reliable source detection algorithm are needed. Recent studies of optical surveys have not yet lead to any detection [9] but the area covered is still too small and, to keep hope alive, until dedicated surveys will become available, it is possible to use as many different surveys (both optical and in the near infrared) as long as they match the desired characteristics in terms of limiting magnitude, angular resolution and coverage. Even more reensuring is that an analysis by [10] (but see also [11]), shows that there is still a lot of room for improvement: modern optical surveys cover only $1/6$ part of the whole sky and their are not at complete beyond z=2. Therefore, approximately

only 3% of possible strings could be detected by this method (if we suppose simple homogeneous distribution of straight strings in the Universe).

The second optical method is the serendipity discovery through anomalous lensing of extended objects. The huge ratio existing between the string width and length leads to a sort of step function signature on the gravitationally lensed images of background sources. As it has been shown in [12–14], this implies that the lensing of an extended object by a cosmic string produces pairs of undistorted images and sharp edges in the isophotes of the lensed object: a phenomenon which cannot be modeled by any standard gravitational lensing from compact objects. This method was analysed in detail and summarized in a paper [10] concerning the photometric and spectroscopic study of the candidate source CSL-1 which could be rejected only at the end of a lengthy observational work. The CSL-1 case lead to elaborate a technique for cosmic string search through gravitational lensing using ultra-deep optical surveys with high resolution instruments (see, for example, [10], [11]). Taking into account the predicted number of cosmic strings it was estimated that gravitational lensing events are very rare ones: the number of so-called "chains" of gravitational lensed pairs varies from 0.3 to 3 going from the most conservative to the most optimistic models.

Other opportunities to detect Cosmic String Signatures are in the study of the anisotropy of the CMBR. As mentioned above, cosmic strings are expected to induce discontinuities in the anisotropy of the CMB (Cosmic Microwave Background) [4, 15, 16]. This method offers two advantages over the optical methods. The background source (CMB) is the most distant source in the Universe (redshift ~ 1000) or, equivalently, it is the closest source to the particle horizon of our Universe. Therefore, all the cosmic strings which are inside the observable part of the Universe will affect the CMB. The second advantage is that multifrequency all-sky surveys of the CMB already exist (WMAP data) and even better ones are planned for the immediate future (e.g. Planck mission which is currently operational). These surveys cover the whole sky, while the largest optical surveys available cover only $1/6$ part of the whole sky. So far, however, this method has been limited by the low angular resolution of CMB data (ca. ~ 10 arcminute for WMAP) and by the relatively low sensitivity which may prevent the identification of the sharp edges which are expected to trace the position of a cosmic string. It is not a surprise, therefore, that preliminary studies have allowed only to set upper limits [17].

We must stress that the optical and CMB methods provide complementary information and in order to provide definitive results they must be used in conjunction. A cosmic string inducing CMB anisotropy can in fact be at any redshift within the range 0 to 1000, while observable gravitational lensing effects can be produced only by strings laying between the epoch of galaxy formation (redshift $\sim 5 - 7$) and the present epoch.

Finally, it needs to be mentioned that other observables rely on more exotic manifestations such as, for instance, the ability of cosmic string to generate gravitational wave

radiation and the possible link between cosmic strings and the progenitors of ultra high energy cosmic rays.

Taking into account all the above at the present time, the investigation of the CMB anisotropy appears as the most effective and potentially fruitful method to search for cosmic strings signatures since it exploits one of the model independent properties of cosmic strings, namely the fact that they form conical space-time. Furthermore radio surveys sample the universe down to $z = 1000$ and cover the whole sky thus allowing to probe the whole volume inside the surface of last scattering and are potentially capable to detect 100% strings and not the mere 3% as it is the case for optical surveys.

The work outlined in the present thesis was aimed at searching for cosmic string signatures both in optical and CMB data. After a preliminary refinement of the theory behind the simulation of cosmic strings, I searched for signature left by a vertical straight cosmic string in the CMB. In such simplifying assumption, I used the S.Co.P.E. computational grid to produce a large number of simulations covering a wide range of values for the characterizing parameters of the string. By using the CMBFAST code to combine them with a CMB signal compatible with the WMAP-5 data, it was possible to generate realistic maps of the CMB temperature distribution expected in presence of a straight cosmic string. The simulated maps were then used first to test an innovative procedure aimed at amplifying the signal by effectively smoothing the noise, and then to evaluate the efficiency of some filters. The statistical analysis of the application of these filters to the simulated data lead to encouraging results and opened the way to the application of the method to the real WMAP data.

In parallel, I also begun to work on the implementation of a more reliable method for the detection of the gravitational lensing effects induced by the string (chapter 7). As it will be discussed later, this method suffers from many spurious effects mainly induced by the fact that, in order to be effective, the detection of background galaxies needs to be pushed down to very low flux limits. At these flux levels photometric errors, as well as noise statistics increase the number of spurious detections and, for instance, an application to the Sloan Digital Sky Survey leads to an huge and unrealistic number of candidate pairs. One way to minimize the contamination introduced in the catalogues by the spurious detection, is to increase the contrast by selecting pairs in the 3D space id est by attributing to each galaxy a redshift estimate. At this purpose, I started a collaboration to determine photometric redshifts of galaxies and QSOs [18]. The method is based on multiwavelength photometry and on a combination of various data mining techniques developed under the EuroVO and NVO frameworks for data gathering, preprocessing and mining, while relying on the scaling capabilities of the computing grid. This method allowed us to obtain photometric redshifts with an increased accuracy (up to 30%) with respect to the literature.

This thesis is therefore structured as it follows. The first part is dedicated to the

description of the physics underlying the theory of cosmic strings. The needed basis of cosmology (chapter 2) and CMB physics (chapter 3) are provided as well as an overview of phase transitions and topological defects (chapter 4). Successively, the features of cosmic strings (chapter 5) and of their possible signatures (chapter 6) are depicted. In chapter 7, I describe the method for the determination of photometric redshifts of galaxies and QSOs, while the description of my work on CMB data (simulations, filters, tests and real data analysis) is presented in chapter 8. The last chapter contains the conclusions of this thesis, namely a brief summary of the main results and an outline of the future developments of my research.

Chapter 2

Modern Cosmology

The Hot Big Bang model, which describes the evolution of the universe from $\sim 1/100$ seconds after the initial explosion through the present epoch, is a theory so well-attested that it deserved to be called the **standard cosmology**. It is based upon the so called *cosmological principle* (Milne, 1933), which asserts that the universe is, on large scales, both homogeneous and isotropic. An assumption which is supported by many evidences including the measured distributions of galaxies and of faint radio sources, but by far the best evidence comes from the observed uniformity of the cosmic microwave background radiation. Also, the universe must be subjected to the same physical laws everywhere, so that every observer, in every point, can apply the same laws and derive the same results. Restated in a Copernican form, the principle implys that there is no privileged position in the universe.

2.1 The expanding Universe

The line element for any spacetime consistent with the cosmological principle can be written in the Friedmann-Robertson-Walker (FRW) form[1],

$$ds^2 = dt^2 - a^2(t)d\ell, \tag{2.1}$$

where t is the physical time, $a(t)$ is the scale factor, and $d\ell$ represents the line element on a three-dimensional space of constant curvature. In spherical coordinates, this three-metric takes the form

$$d\ell^2 = \frac{dr^2}{1-kr^2} + r^2(d\theta^2 + \sin\theta d\phi^2) \tag{2.2}$$

where the constant curvature k is determined by the spatial topology and geometry of the universe (Fig. 2.1):

$$\begin{array}{lll} k > 0, & S^3 & \text{closed} \\ k = 0, & R^3 & \text{flat} \\ k < 0, & H^3 & \text{open} \end{array}$$

[1] hereafter natural units will be used

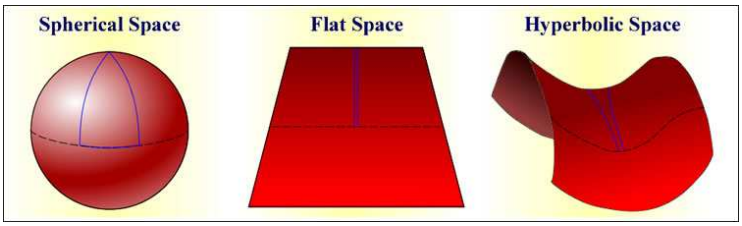

Figure 2.1: *Possible spatial topologies of universe according to the value of the curvature* k

The homogeneity of the matter content of the universe implies that the fluid flow lines are along constant (r, θ, ϕ) trajectories defining the so called comoving coordinates. Note, however, that physical distances are determined by multiplying the comoving distances by the scale factor $a(t)$. It is often useful to introduce an alternative time coordinate, the conformal time τ, defined as:

$$d\tau = \frac{dt}{a(t)} \tag{2.3}$$

so that the metric (2.1) takes the simple form

$$ds^2 = a^2(\tau)[d\tau^2 - d\ell^2], \tag{2.4}$$

Some kinematic effects follow immediately from the FRW metric (2.1). Consider two comoving particles separated by a distance ℓ. It is clear that ℓ will grow in time in proportion to $a(t)$. There will be a corresponding recessional velocity given by

$$v = H\ell, \tag{2.5}$$

where the Hubble parameter H (or 'Hubble's constant') is

$$H = \frac{\dot{a}}{a},$$

with dots denoting derivatives with respect to the cosmic time t. The relation (2.5) is known empirically as Hubble's law: the observation that distant galaxies are receding from our own with velocities proportional to their distance. The parameter H is today measured to be

$$H \approx 50 - 100 kms^{-1} Mpc^{-1},$$

with the large uncertainties arising because of the unreliability of cosmological distance measurements. We adopt the usual convention by incorporating these uncertainties in the dimensionless parameter h

$$h = H_0/100 kms^{-1}Mpc^{-1},$$

where $0.5 \leq h \leq 1.0$. Another implication of the metric (2.1) is that the light with a frequency ν will be redshifted by the usual Doppler effect, $\dot{\nu}/\nu = \dot{a}/a$. Consequently, the frequency will decay as $\nu(t) \propto a(t)^{-l}$, so the redshift of spectral lines from a distant galaxy can provide a measure of its relative age and distance. This redshift z is defined as

$$1 + z \equiv \frac{a(t_0)}{a(t_e)} = \frac{\nu_e}{\nu_0}$$

where t_e is the time the radiation was emitted at a frequency ν_e and the subscript 0 denotes quantities measured at the present day.

2.2 The Einstein equations

The scale factor $a(t)$ in the metric (2.1) is constrained to obey Einstein's equations. The energy-momentum tensor $T^{\mu\nu}$ for the matter content must have the same symmetries as the homogeneous FRW-metric (2.1), so it takes the form of a perfect fluid, that is,

$$T_{\mu\nu} = (\rho + p)u_\mu u_\nu - g_{\mu\nu} \tag{2.6}$$

where the energy density ρ and the pressure p are functions of time t only, and u^μ is the four-velocity of the comoving matter, that is, $u^0 = 1$ and $u^i = 0$. The local conservation of energy $T^{\mu\nu}_{;\nu} = 0$ then implies

$$\dot{p} + 3\frac{\dot{a}}{a}(\rho + p) = 0 \tag{2.7}$$

The second term accounts for the dilution of the energy density as the universe expands, whereas the third represents the work done by the pressure of the fluid. In order to have a complete specification of the evolution, the equation of state for the matter, $p = p(\rho)$, is needed. If the universe is filled with 'dust', i.e. non-relativistic matter with negligible pressure $p \ll \rho$, then (2.7) implies $\rho \propto a^{-3}$. On the other hand, the appropriate equation of state for radiation is that of an ideal relativistic gas, $p = \rho/3$. In this case, the density varies as $\rho \propto a^{-4}$, with the additional power of $a(t)$ due to frequency redshifting. Once matter becomes non-relativistic, it will inevitably dominate the energy density of an expanding universe because $\rho_m/\rho_r \propto a$.

The Einstein equations

$$R_{\mu\nu} - \frac{1}{2}g_{\mu\nu}R = 8\pi G T_{\mu\nu}, \tag{2.8}$$

imply the Friedmann equation

$$\left(\frac{\dot{a}}{a}\right)^2 + \frac{k}{a^2} = \frac{8\pi G}{3}\rho, \tag{2.9}$$

which, along with (2.7) and the equation of state, determines the evolution. For radiation with $p = \rho/3$, it is clear from (2.9) that in a flat universe ($k = 0$) the scale factor will go as $t^{1/2}$. The energy density will then be given by the relation

$$\rho_{crit} = \frac{3}{32\pi G t^2}, \tag{2.10}$$

where the subscript indicates that this is the density of a flat universe - the critical value lying between that for open and closed universes at the same time t. The dimensionless density parameter

$$\Omega = \frac{\rho}{\rho_{crit}}, \tag{2.11}$$

summarizes this difference with $\Omega < 1$, $\Omega = 1$ and $\Omega > 1$ corresponding to open, flat and closed universes, respectively.

For a pressureless matter-dominated flat universe, the scale factor will grow as $t^{2/3}$ and the expression for the critical density, again from (2.9), is

$$\rho_{crit} = \frac{1}{6\pi G t^2}. \tag{2.12}$$

Given the enormous timescale of cosmological evolution, it is remarkable how near unity Ω is placed by current observations. Using rotation curves for spiral galaxies out to a radius enclosing most visible matter, one can estimate the mass density associated with luminous matter, $\Omega_{lum} \leq 0.01$. However, there is considerable evidence that galactic rotation curves extend undiminished out into a dark halo, implying that Ω is almost an order of magnitude higher. Further dynamical studies on galaxy cluster scales, such as infall to Virgo, similarly suggest

$$\Omega_{clust} \approx 0.1 - 0.2.$$

Indeed, there is some evidence from very large-scale surveys for a smooth background with $\Omega_0 \approx 1$. This seems to indicate that there must be a significant dark matter component to the energy density of the universe. Primordial nucleosynthesis arguments strongly suggest that this dark matter must be mainly non-baryonic - perhaps massive neutrinos or other more exotic forms of matter (such as WIMPS: Weakly Interacting Massive Particles).

Given the expansion rate of a matter-dominated flat universe, the age of the universe measured from the initial singularity ($a = 0$) is

$$t_0 = \frac{2}{3} H_0^{-1},$$

corresponding to an age in the range 10-20 billion years. This is corroborated by radioisotope dating of the solar system, as well as by stellar and globular cluster lifetimes.

The FRW models (2.1) have cosmological horizons; it is only possible at a time t to have received light signals from particles lying within a radial distance:

$$d_H = a(t) \int_0^t \frac{dt'}{a(t')}.$$

In the radiation dominated era for a flat universe, the horizon size is $d_H = 2t$, while in the matter dominated era $d_H = 3t$.

2.3 A brief thermal history of Universe

The assumption that the early universe was in thermal equilibrium considerably simplifies its study, because its description depends only on the temperature T (assuming negligible chemical potentials for all particle species). For much of the early history of the universe, the equation of state of a relativistic ideal gas applies; the energy density at a temperature T is given by

$$\rho = \frac{\pi^2}{30} N(T) T^4, \tag{2.13}$$

where $N(T) = N_b(T) + \frac{7}{8} N_f T$, and $N_b(T)$ and $N_f(T)$ are respectively the effective number of distinct helicity states of bosons and fermions with masses $m \leq T$. For particles with $m \gg T$, the equilibrium density is exponentially suppressed. Particle species 'freeze-out' or decouple from thermal equilibrium as the universe expands and cools. This decoupling occurs when a particle's interaction rate Γ_{int} falls below the Hubble expansion rate H, defining the decoupling temperature T_d when $\Gamma_{int} \approx H$.

While the universe remains in thermal equilibrium ($\Gamma_{int} \gg H$), the expansion is adiabatic, that is, entropy is conserved,

$$\frac{d}{dt} \left(s a^3 \right) = 0,$$

where the entropy density s is given by

$$s = \frac{2\pi^2}{45} N(T) T^3.$$

For $N(T) = const.$, these relations imply that $aT = const.$ It is also possible to express the cosmic time t in terms of the temperature T, combining (2.10) and (2.13) opportunely:

$$t = \left(\frac{45}{16\pi^3 NG}\right)^{1/2} T^{-2} \approx 0.30 N^{-1/2} \frac{m_{pl}}{T^2}$$

Let us now briefly follow the thermal history of the universe backwards in time. Until about 400,000 years after the Big Bang, all matter in the universe was fully ionized. However, when the temperature dropped below the hydrogen ionization threshold of 13.6 eV, electrons and protons began to combine to form hydrogen atoms, a process termed 'recombination'. The resulting rapid fall in the free electron density reduced the electron-photon interaction rate (Thomson scattering) and matter and radiation decoupled. This occurred at approximately

$$t_{dec} \approx 5.6 \times 10^{12} \left(\Omega h^2\right)^{-1/2} s,$$
$$z_{dec} \approx 1100 - 1200.$$

The decoupled photon gas is observed today as the cosmic microwave background; it has a characteristic black-body spectrum of temperature $T = 2.7$ K and a corresponding energy density $\rho_\gamma = 4.5 \times 10^{-34}$gcm^{-3}.

Extrapolating further back in time, we come to a redshift z_{eq} when the matter and radiation densities were comparable. Taking into account the contribution of neutrinos to the total radiation background, the matter-radiation transition redshift and time are

$$t_{eq} \approx 4 \times 10^{10} \left(\Omega h^2\right)^{-2} s,$$
$$z_{eq} \approx 2 \times 10^4 \Omega h^2.$$

The density of the universe then was $\rho_{eq} = 3.2 \times 10{-}16 \left(\Omega h^2\right)^4$g cm^{-3}.

Prior to the matter-radiation transition, between about one second and three minutes after the Big Bang, the density and temperature of the primordial plasma were sufficiently high to synthesize the lightest elements: D, ^{3}He, ^{4}He and ^{7}Li. Earlier still, at $t \ll 1$ s, electron-positron pairs annihilated to leave a high temperature plasma consisting only of photons, neutrinos, electrons, protons and neutrons. Prior to $t \approx 10^{-2}$ s, a wide variety of hadronic resonances were excited, and it is here that further progress is hampered by the numerical difficulty of calculations involving strong interactions. The same applies for the preceding quark-hadron transition at about $t \approx 10^{-4}$ s, but this is not the end of the story. For $t < 10^{-4}$ s, the universe would have been filled with a plasma of quarks, leptons and gauge bosons. The common feature of such high energy particle physics models is that they exhibit asymptotic freedom, that is, as the temperature is increased, particle interactions weaken. This means that a description of the

primordial plasma should simplify greatly in earlier hotter epochs. Indeed, it is generally assumed that the equation of state for a relativistic gas (2.13) will be valid again at times earlier than $t < 10^{-10}$ s, that is, from around electroweak symmetry breaking through to the grand unification scale at 10^{-35} s and even beyond to the Planck epoch at 10^{-43} s. Fig. (2.2) briefly summarizes the thermal history of the universe as it is currently understood.

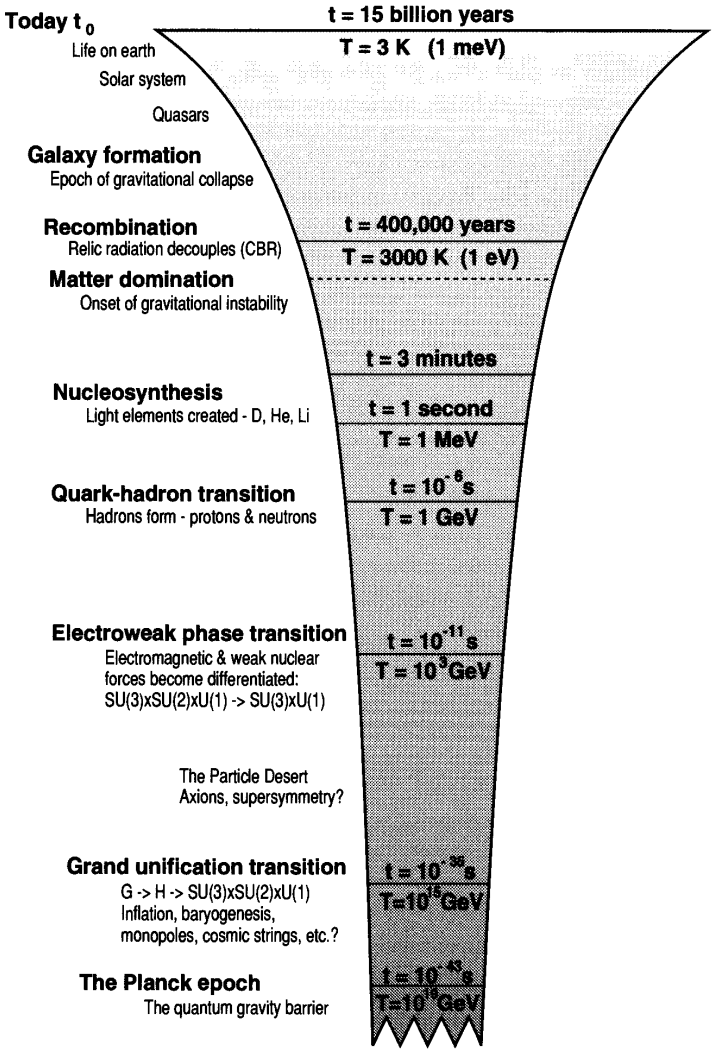

Figure 2.2: *Brief thermal history of the universe*

2.4 Primordial nucleosynthesis

Protons and neutrons may combine to form a nucleus only when the surrounding temperature is low enough to allow the nucleus to stay bound. Nucleosynthesis began with the 'freeze out' of the neutron-proton ratio at a temperature $T \approx 0.8$ MeV at $t \approx 1$s. Prior to this, weak interactions maintained thermal equilibrium which was governed by the relation

$$\frac{n_n}{n_p} \approx \exp(-\Delta m/T), \tag{2.14}$$

where the neutron-proton mass difference is $\Delta m = m_n - m_p = 1.29$ MeV. Before the decoupled neutrons could decay, most became bound into deuterium, $p + n \rightarrow D + \gamma$. Subsequently, light elements such as ^{3}He, ^{4}He and ^{7}Li were synthesized. The amount of primordial elements can be computed. Their abundance depends on the nucleon density at the time. By using nucleon density as a parameter to compare calculation with observation, one can obtain the nucleon density (Fig. 2.3).

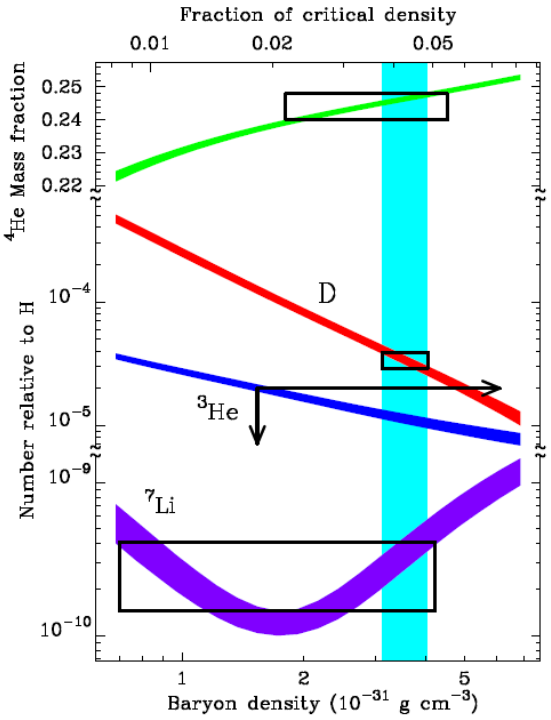

Figure 2.3: *Nuclear density as function of baryionic density*

Theoretical predictions of the Big Bang nuclesynthesis are in good agreement with

experimental data by WMAP. In particular, the Deuterium determinations are fully compatible with the value of the baryon density $\Omega_b h^2 = 0.0024 \pm 0.0009$ suggested by WMAP data. This is quite remarkable, since D is strongly dependent on the baryon content of the universe. Instead for ^{7}Li, there is still a significant discrepancy between the theory and experiments.

Chapter 3

The Cosmic Microwave Background

As it was outlined in the previous chapter, early in its history, the energy density of the Universe was divided among matter, radiation, and dark energy. The matter consisted of all known elementary particles and included a dominant component of dark matter, stable and massive particles with negligible electromagnetic interactions. Matter and radiation were in thermal equilibrium. As the Universe expanded, wavelengths were stretched so that particle energies (and hence the temperature of the Universe) decreased. The Universe was initially radiation dominated. Most of its energy density was in photons, neutrinos, and kinetic motion. After the Universe cooled to the point at which the energy in rest mass equaled that in kinetic motion (matter-radiation equality), the expansion rate slowed and the Universe became matter dominated, with most of its energy tied up in the masses of slowly moving, relatively heavy stable particles: among the baryons, mainly protons and deuterons (cfr. 2.4) plus the already mentioned dark matter particles. When the universe became sufficiently cool, electrons and protons combined to form hydrogen atoms H through the reaction

$$p + e \rightarrow \gamma + H,$$

thereby releasing $E_0 = 13.6eV$ of binding energy. Before this occurred, the photons could not travel far, as they were continuously absorbed and re-emitted by the charged particles in the universe. After recombination, the universe was neutral, photons suffered little interactions, and the background photons we see today in the CMB arrive to us from this *decoupling* very remote epoch.

3.1 The story of CMB

In 1963, Arno Penzias and Robert Wilson, two radio astronomers at Bell Labs in Crawford in New Jersey, using a sensitive microwave horn radiometer to measure radio emission from the Cassiopeia A supernova remnant, detected a uniform noise source, which was assumed to come from the apparatus. But after many months of checking the antenna and the electronics (including removal of a birds nest from the horn), they gradually concluded that the signal might actually be coming from the sky. When they heard

about a talk given by P.J.E. Peebles of Princeton predicting a 10 K blackbody cosmological background, they got in touch with the group at Princeton and realized they had detected the cosmological radiation. At the time, Peebles was collaborating with Dicke, Roll, and Wilkinson in a concerted effort to detect the microwave background. The Princeton group wound up confirming the Bell Labs discovery a few months later. Penzias and Wilson published their result in a brief paper with the unassuming title of A measurement of excess antenna temperature at $\lambda = 7.3$ cm; a companion paper by the Princeton group explained the cosmological significance of the measurement. The microwave background detection was a success of the Hot Big Bang model, which to that point had been well outside the mainstream of theoretical physics. The following years saw an explosion of work related to the Big Bang model of the expanding universe.

The history of earlier probable detections of the microwave background which were not recognized as such is less well known. Tolmans classic monograph on thermodynamics in an expanding universe was written in 1934 [19], but only in 1948 a blackbody relic of the early universe was predicted theoretically by Alpher and Herman [20]. Prior to this, in 1940, Andrew McKellar [21] had observed the population of excited rotational states of CN molecules in interstellar absorption lines, concluding that it was consistent with being in thermal equilibrium with a temperature of around 2.3 K. Walter Adams also made similar measurements (1941, [22]). Its significance was unappreciated and the result essentially forgotten, possibly due to the World War II events which had begun to divert much of physics talents towards military problems.

Alpher and Hermans prediction of a 5 K background contained no suggestion of its detectability with available technology and had little impact. Over the next decade, George Gamow and collaborators, including the same Alpher and Herman, made a variety of estimates of the background temperature which fluctuated between 3 and 50 Kelvin. This lack of a definitive temperature might have contributed to an impression that the prediction was less certain than it actually was, because it aroused little interest among experimenters even though microwave technology had been highly developed through radar work during the war. At the same time, the incipient field of radio astronomy was getting started. In 1955, an isotropic emission corresponding to a blackbody temperature of $T = 3 \pm 2$ K was found in an all-sky survey at a wavelength of $\lambda = 33$ cm [23]. This was almost certainly a detection of the microwave background, but its significance was unrealized.

The significance of this measurement was not realized, amazingly, until 1983. Finally in the early 1960s the pieces began to fall in place: Doroshkevich and Novikov (1964, [24]) emphasized the detectability of a microwave blackbody as a basic test of Gamows Hot Big Bang model. Simultaneously, Dicke and collaborators began searching for the radiation, prompted by Dickes investigations of the physical consequences of the Brans-Dicke theory of gravitation. Their efforts were however scooped by Penzias and Wilsons

discovery.

3.2 CMB features

The last two decades have seen remarkable advances in observational cosmology and quantitative cosmological constraints now come from a number of complementary probes. Amongst these, the CMB temperature and polarization anisotropies have played a particularly important role, providing the most direct observational links to the physics of the early universe since the fluctuations were mostly imprinted around the time of recombination.

The basic picture is that the angular variations in temperature that we observe today are a snapshot of the local properties (density, peculiar velocity and the total gravitational potential) of the gas of CMB photons at the time the primordial plasma recombined at redshift $z \approx 1100$. These quantities are related to the primordial perturbations, plausibly generated during an epoch of cosmological inflation, by the rather simple acoustic physics of the prerecombination plasma. The CMB anisotropies therefore encode information on the primordial perturbation itself, as well as on the matter composition and geometry of the universe. This also implies that any topological defects resulting from the formation of the universe must have left its signature.

Large-angle temperature anisotropies were first discovered by COBE-DMR in 1992 [25]. Since then, tens of instruments have mapped the anisotropies and we now have high quality measurements of the statistics of the anisotropies over three decades of angular scales. The current state-of-the-art dataset is provided by COBE's successor, the WMAP satellite, which released its five-year results in March 2008. A map of the temperature fluctuations from WMAP, after removing the effect of microwave emission from our galaxy, is shown in Fig. 3.1. The WMAP results are beautifully fit by a simple cosmological model with flat space, baryons and cold dark matter making up 4% and 21% respectively of the energy density with the remaining 75% in some form of dark energy, and Gaussian-distributed, adiabatic primordial density perturbations with an almost, but not quite, scale-invariant spectrum. The third-generation CMB satellite, Planck, will image the sky in nine wavelength bands with a best resolution below 5 arcmin. Forecasts indicate that Planck should measure several important parameters to better than 1%, and place tight constraints on inflation models.

The CMB temperature fluctuations are complemented by their linear polarization. Polarization is generated by the scattering of anisotropic radiation and for the CMB this occurs at two epochs: around recombination and, later, during the epoch of reionization. The small polarization signal (r.m.s. $\sim 5\mu K$) was first detected in 2002 by the DASI instrument [26], and has subsequently been measured by several groups.

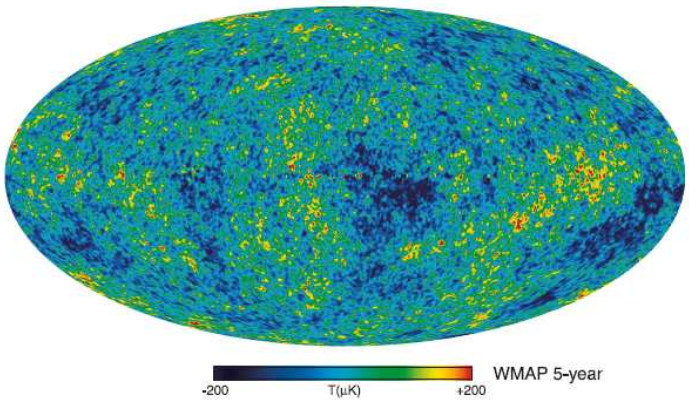

Figure 3.1: *Fluctuations in the CMB temperature, as determined from five years of WMAP data, about the average temperature of 2.725K.*

The signal-to-noise of these measurements is still poor if compared to the temperature anisotropies, but important constraints have already emerged on the epoch of reionization from WMAP. Polarization also provides the only viable route in the near-future for detecting the background of gravitational waves predicted by the inflationary models. A positive detection would be particularly interesting for all attempts aiming at realising inflation in string theory, and would rule out some alternatives to inflation such as the cyclic model.

3.2.1 The power spectrum

Blackbody radiation in a perfectly homogeneous and isotropic universe, which is always adopted as a zero-th order approximation, must be at a uniform temperature, by assumption. When perturbations are introduced, three elementary physical processes can produce a shift in the apparent blackbody temperature of the radiation emitted from a particular point in space. All temperature fluctuations in the microwave background are due to one or more among the following effects:

- A change in the intrinsic temperature of radiation at a given point in space. This will occur if the radiation density increases via adiabatic compression, just as with the behavior of an ideal gas. The fractional temperature perturbation in the radiation just equals the fractional density perturbation.

- A Doppler shift if the radiation at a particular point is moving with respect to the observer. Any density perturbations within the horizon scale will necessarily be accompanied by velocity perturbations. The induced temperature perturbation

in the radiation equals the peculiar velocity, with motion towards the observer corresponding to a positive temperature perturbation.

- A difference in gravitational potential between a particular point in space and the observer will result in a temperature shift of the radiation propagating between the point and the observer due to gravitational redshifting. This is known as the Sachs-Wolfe effect. The Sachs-Wolfe effect is often broken into two pieces, the usual effect and the so-called Integrated Sachs-Wolfe effect. The latter arises when gravitational potentials are evolving with time: radiation propagates into a potential well, gaining energy and blueshifting in the process. As it climbs out, it loses energy and redshifts, but if the depth of the potential well has increased during the time the radiation propagates through it, the redshift on exiting will be larger than the blueshift on entering, and the radiation will gain a net redshift, appearing cooler than it was when emitted.

The result of temperature fluctuations is the basic observable of the CMB: the power spectrum, i.e. CMB intensity as a function of frequency and direction on the sky $\hat{\mathbf{n}}$. Because the CMB spectrum is an extremely good blackbody with a nearly constant temperature across the sky T, we generally describe this observable in terms of a temperature fluctuation $\Omega(\hat{\mathbf{n}}) = \Delta T/T$.

Consider the multipole decomposition of the temperature field in terms of spherical harmonics Y^*_{lm}:

$$\Omega_{lm} = \int \Omega(\hat{\mathbf{n}}) Y^*_{lm}(\hat{\mathbf{n}}) d\hat{\mathbf{n}}.$$

If the sky temperature field arises from Gaussian random fluctuations, then the field is fully characterized by its power spectrum $\Omega^*_{lm}\Omega_{l'm'}$. The order m describes the angular orientation of a fluctuation mode, but the degree (or multipole) l describes its characteristic angular size. Thus, in a Universe with no preferred direction, we expect the power spectrum to be independent of m. Finally, we define the angular power spectrum C_l by

$$\langle \Omega^*_{lm}\Omega_{l'm'} \rangle = \delta_{ll'}\delta_{mm'}C_l$$

Here the brackets denote an ensemble average over skies with the same cosmology. The best estimate of C_l is then from the average over m.

Because there are only the $(2l+1)$ modes with which to detect the power at multipole l, there is a fundamental limit in determining the power. This is known as the *cosmic variance* (just the variance on the variance from a finite number of samples):

$$\frac{\Delta C_l}{C_l} = \sqrt{\frac{2}{2l+1}}.$$

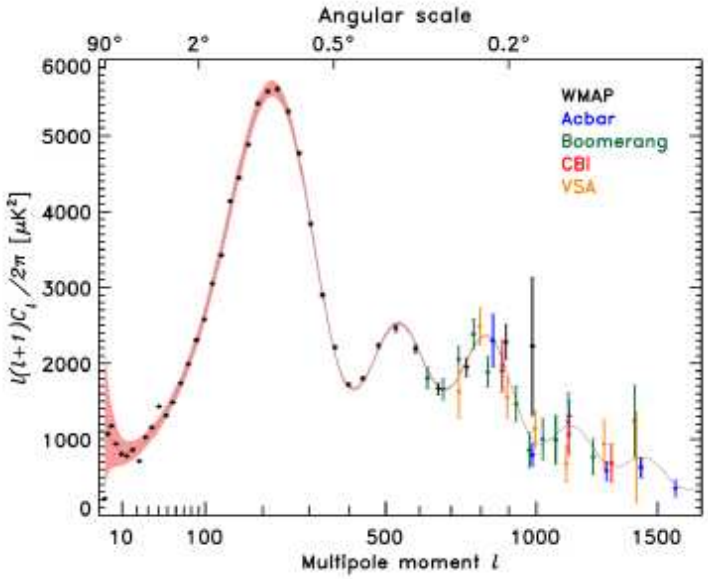

Figure 3.2: *Data from WMAP, and high-l data from other experiments are shown, in addition to the best-fit cosmological model to the WMAP data alone. Note the multipole scale on the bottom and the angular scale on the top.*

For historical reasons, the quantity that is usually plotted, sometimes termed the TT (temperature-temperature correlation) spectrum, is

$$\Delta T^2 \equiv \frac{l(l+1)}{2\pi} C_l T_{CMB}^2 \tag{3.1}$$

where T_{CMB} is the blackbody temperature of the CMB (Fig. 3.2). This is the variance (or power) per logarithmic interval in l and is expected to be (nearly) uniform in inflationary models (scale invariant) over much of the spectrum. This normalization is useful in calculating the contributions to the fluctuations in the temperature in a given pixel from a range of l values:

$$\Delta T^2 = \int_{l_{min}}^{l_{max}} \frac{(2l+1)}{4\pi} C_l T_{CMB}^2 dl.$$

Fig. 3.2 shows the current understanding of the temperature power spectrum. The region below $l \approx 20$ indicates the initial conditions. These modes correspond to Fourier modes at the time of decoupling, with wavelengths longer than the horizon scale.

At high l values -before decoupling- the CMB power spectrum is characterized by a sequence of peaks due to acoustic oscillation in the baryon-photon plasma. In fact, the matter in the universe has significant pressure because it is tightly coupled to radiation. This pressure counteracts any tendency for matter to collapse gravitationally. For-

mally, the Jeans mass[1] is greater than the mass within a horizon volume for times earlier than decoupling. During this epoch, density perturbations will set up standing acoustic waves in the plasma. Let us now consider a standing wave permeating space with frequency ω and wave number k, where these are related by the velocity of displacement (the sound speed, $v_s \approx c/\sqrt{3}$) in the plasma: $\omega = kv_s$. The wave displacement A_k for this single mode can then be written as

$$A_k(x,t) \propto \sin(kx)\cos(\omega t).$$

The displacement is maximal at time t_{dec} of decoupling for

$$k_{TT} v_s t_{dec} = \pi, 2\pi, 3\pi \ldots.$$

Note that even in this tightly coupled regime, the Universe at decoupling was quite dilute, with a physical density of less than $10^{-20} g\ cm^{-3}$. Because the photons diffuse, their mean free path is not infinitely short and this pattern does not go on without bound. The overtones are damped, and in practice only five or six such peaks will be observed, as seen in Fig. 3.2.

3.2.2 Polarization

In addition to temperature fluctuations, the simple physics of decoupling inevitably leads to non-zero polarization of the microwave background radiation although quite generically the polarization fluctuations are expected to be significantly smaller than the temperature fluctuations. Some of the CMB radiation is linearly polarized, thanks to the fact that most electrons at the surface of last scattering see a quadrupole temperature anisotropy around them. Polarization correlated with temperature anisotropies was first reported in 2002 by the DASI experiment [26]; more recently, the WMAP experiment has fully established this correlation over a large area of the sky.

Non-zero linear polarization in the microwave background is generated around the epoch of decoupling because the Thomson scattering which couples the radiation and the electrons is not isotropic but varies with the scattering angle. The total scattering cross-section, defined as the radiated intensity per unit solid angle divided by the incoming intensity per unit area, is given by

$$\frac{d\sigma}{d\Omega} = \frac{3\sigma_T}{8\pi} \left|\hat{\epsilon}' \cdot \hat{\epsilon}\right|^2$$

[1]The critical mass a volume of space must contain before it will collapse under the force of its own gravity.

where σ_T is the total Thomson cross section and the vectors $\hat{\epsilon}$ and $\hat{\epsilon}'$ are unit vectors in the planes perpendicular to the propagation directions which are aligned with the outgoing and incoming polarization, respectively.

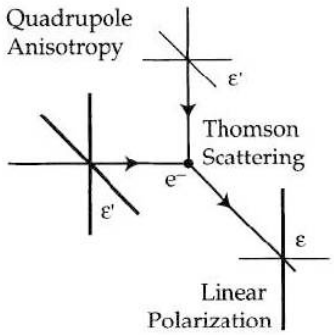

Figure 3.3: *An electron on the surface of last scattering emits linearly polarized radiation according to the quadrupole moment of its thermal environment. Thicker lines represent more intense radiation.*

It is possible to show that an unpolarized incoming radiation will be Thomson scattered into linearly polarized radiation if and only if the incoming radiation has a nonzero quadrupolar directional dependence. During the tight-coupling epoch, the radiation field has only monopole and dipole directional dependences; therefore, scattering can produce no net polarization and the radiation remains unpolarized. As this tight coupling begins to break down as the recombination begins, a quadrupole moment of the radiation field will begin to grow due to free streaming of the photons. Polarization is generated during the brief interval when a significant quadrupole moment of the radiation has built up, but the scattering electrons have not yet all recombined. Due to this competition between the quadrupole source building up and the density of scatterers declining, the amplitude of polarization in the microwave background is generically suppressed by an order of magnitude compared to the temperature fluctuations.

Observations of linear polarization are often described in terms of the Stokes parameters $I(\hat{\mathbf{n}}, \nu)$, $Q(\hat{\mathbf{n}}, \nu)$, $U(\hat{\mathbf{n}}, \nu)$ and $V(\hat{\mathbf{n}}, \nu)$. The I parameter is the total intensity, Q measures the difference in brightness between two orthogonal linear polarizations, and V measures the circular polarization. The U parameter, like Q, measures linear polarization and is defined as the difference in brightness between two linear polarizations at 45° to those used to define Q. Thomson scattering of the CMB does not generate circular polarization so we expect the primordial $V = 0$. In linear theory, their frequency dependence follows that of the temperature anisotropies; dividing by the derivative of the CMB blackbody brightness with respect to (log) temperature allows us to express the Stokes parameters as frequency-independent fractional *thermodynamic equivalent temper-*

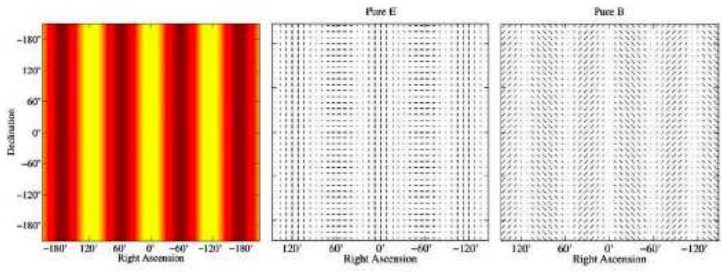

Figure 3.4: *Illustration of E and B polarization modes.* ***Left panel:*** *a standing acoustic wave, which is a single Fourier component of the scalar density perturbations.* ***Center panel:*** E*-mode polarization comes from the local temperature anisotropy in the acoustic mode, as well as Doppler boosting of radiation from matter as it moves in accordance with the mode.* ***Right panel:*** B*-mode polarization is at a* 45° *respect with* E*-mode polarization, and cannot be generated by scalar perturbations.*

atures. We shall denote the equivalent temperatures by $Q(\hat{\mathbf{n}})$ and $U(\hat{\mathbf{n}})$.

The complex polarization $Q \pm iU$ can be expanded in terms of a real scalar field $\sum_{lm} E_{lm} Y_{lm}(\hat{\mathbf{n}})$ and a real pseudo-scalar field $\sum_{lm} B_{lm} Y_{lm}(\hat{\mathbf{n}})$,

$$(Q \pm iU)(\hat{\mathbf{n}}) = \sum_{lm} (E_{lm} \mp iB_{lm})_{\mp 2} Y_{lm}(\hat{\mathbf{n}}),$$

where the summations are over $l \geq 2$ and ${}_{\mp 2}Y_{lm}(\hat{\mathbf{n}})$ are spin-∓ 2 spherical harmonics.

To gain further intuition for E modes and B modes, consider the case where the potentials $\sum_{lm} E_{lm} Y_{lm}(\hat{\mathbf{n}})$ and $\sum_{lm} B_{lm} Y_{lm}(\hat{\mathbf{n}})$ behave locally like a plane wave across a small patch of the sky (that can accurately be treated as flat). The E and B contributions to the polarization are depicted in Fig. 3.4. Quite generally, a given potential ψ generates a B mode with $Q \pm iU = \mp i\partial^2\psi$ and an E mode with $Q \pm iU = \partial^2\psi$. Since $i = e^{2i\pi/4}$, the B-mode polarization pattern is obtained from the E mode by rotating by 45° about the line of sight.

The decomposition of the polarization field into E and B parts is invariant under rotations, and the E and B multipoles transform like those for the temperature anisotropies, e.g. $E_{lm} \to \sum_{m'} D^l_{mm'} E_{lm'}$. Under the operation of parity,

$$(Q \pm iU)(\hat{\mathbf{n}}) \to (Q \mp iU)(-\hat{\mathbf{n}}),$$

so that $E_{lm} \to (-1)^l E_{lm}$ (electric parity) while $B_{lm} \to (-1)^{l+1} B_{lm}$ (magnetic parity). Rotational and parity invariance in the mean limit the non-zero two-point correlations between polarization (and temperature) multipoles to

$$\begin{aligned}
\langle E_{lm} E^*_{l'm'} \rangle &= \delta_{ll'} \delta_{mm'} C^E_l \\
\langle B_{lm} B^*_{l'm'} \rangle &= \delta_{ll'} \delta_{mm'} C^B_l \\
\langle T_{lm} E^*_{l'm'} \rangle &= \delta_{ll'} \delta_{mm'} C^{TE}_l
\end{aligned}$$

which define the power spectra C_l^E, C_l^B and C_l^{TE} (Fig. 3.5). Note that there is no correlation between B and either ΔT or E.

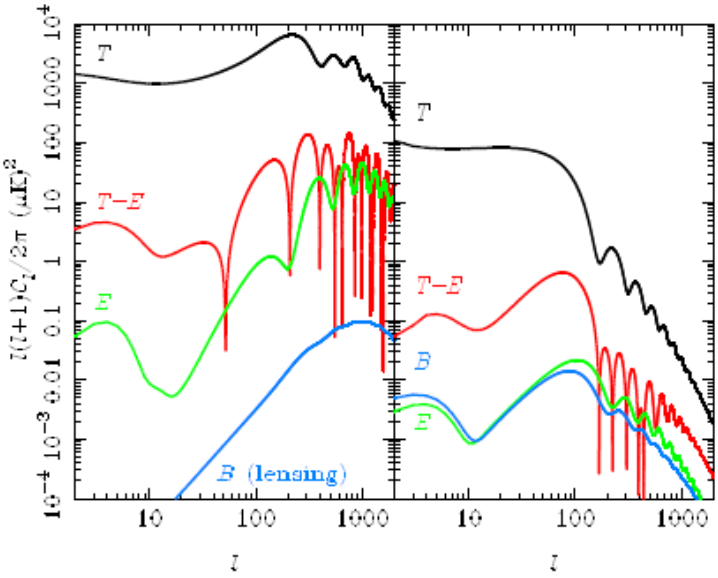

Figure 3.5: *Temperature (black), E-mode (green), B-mode (blue) and T-E cross-correlation (red) CMB power spectra from scalar perturbations (left) and tensor perturbations (gravitational waves; right).*

3.3 Exploring the CMB

Subsequent to the discovery of the CMB, hundreds of experiments have been conducted to measure and characterize the signatures of the radiation. The first experiment was the NASA Cosmic Background Explorer (COBE) satellite that orbited in 1989−1996 and which detected and quantified the large scale anisotropies at the limit of its detection capabilities. Successively, a series of ground- and balloon-based experiments quantified CMB anisotropies on smaller angular scales over the next decade. The primary goal of these experiments was to measure the angular scale of the first acoustic peak, for which COBE did not have sufficient resolution. During the 1990s, the first peak was measured with increasing sensitivity and by 2000 the BOOMERanG experiment reported that the highest power fluctuations occur at scales of approximately one degree [27]. Together with other cosmological data, these results implied that the geometry of the Universe is flat. A number of ground-based interferometers provided measurements of the fluctuations with higher accuracy over the next three years, including the Very Small Array, Degree Angular Scale Interferometer (DASI) and the Cosmic Background Imager (CBI).

DASI made the first detection of the polarization of the CMB and the CBI provided the first E-mode polarization spectrum with compelling evidence that it is out of phase with the T-mode spectrum.

In June 2001, NASA launched a second CMB space mission, the already mentioned WMAP, to take much more precise measurements of the large scale anisotropies over the full sky. The first results from this mission, disclosed in 2003, were detailed measurements of the angular power spectrum to below degree scales, tightly constraining various cosmological parameters. The results are broadly consistent with those expected from cosmic inflation as well as various other competing theories. Although WMAP provided very accurate measurements of the large angular-scale fluctuations in the CMB, it did not have the angular resolution to measure the smaller scale fluctuations which had been observed using previous ground-based interferometers.

A third space mission, the Planck Surveyor, was launched in May, 2009. Planck [28] employs both HEMT radiometers as well as bolometer technology and will measure the CMB on smaller scales than WMAP. Unlike the previous two space missions, Planck is run by ESA (European Space Agency). Its detectors got a trial run at the Antarctic Viper telescope as ACBAR (Arcminute Cosmology Bolometer Array Receiver) experiment which has produced the most precise measurements at small angular scales to date [29] and at the Archeops balloon telescope [30].

Additional ground-based instruments such as the South Pole Telescope [31] in Antarctica and the proposed Clover Project [32], Atacama Cosmology Telescope and the QUIET telescope in Chile [33] will provide additional data not available from satellite observations, possibly including the B-mode polarization.

3.3.1 The COsmic Background Explorer (COBE)

In 1974, NASA issued an Announcement of Opportunity for astronomical missions that would use a small- or medium-sized Explorer spacecraft. Though these proposals lost out to the Infrared Astronomical Satellite (IRAS), their strength made NASA further explore the idea. In 1976, NASA formed a committee of members from each of 1974's three proposal teams to put together their ideas for such a satellite. A year later, this committee suggested a polar-orbiting satellite called COBE to be launched by either a Delta rocket or the Space Shuttle. NASA accepted the proposal provided that the costs be kept under $30 million, excluding launcher and data analysis. Due to cost overruns in the Explorer program due to IRAS, work on constructing the satellite at Goddard Space Flight Center (GSFC) did not begin until 1981. To save costs, the infrared detectors and liquid helium dewar on COBE would be similar to those used on IRAS.

COBE (Fig. 3.6) was placed into sun-synchronous orbit on November 18, 1989 aboard a Delta rocket. It contained the following instruments:

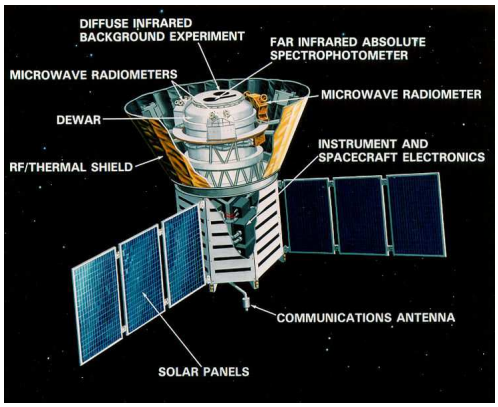

Figure 3.6: *The COBE satellite*

Instrument	Acronym	Description
Differential Microwave Radiometer	DMR	a microwave instrument that would map anisotropies in the CMB
Diffuse InfraRed Background Experiment	DIRBE	a multiwavelength infrared detector used to map dust emission
Far-InfraRed Absolute Spectrophotometer	FIRAS	a spectrophotometer used to measure the spectrum of the CMB

Table 3.1: *Instruments of COBE satellite*

A team of American scientists announced, on April 23, 1992, that they had found the primordial "seeds" (CMBE anisotropy) in data from COBE. The announcement was reported worldwide as a fundamental scientific discovery and ran on the front page of the New York Times. The DMR was able to spend four years mapping the detectable anisotropy of cosmic background radiation as it was the only instrument not dependent on the dewars supply of helium to keep it cooled. This operation was able to create full sky maps of the CMB by subtracting out galactic emissions and dipole at various frequencies (Fig. 3.7).

DIRBE also detected 10 new far-IR emitting galaxies in the region not surveyed by IRAS as well as nine other candidates in the weak far-IR that might be spiral galaxies. Galaxies detected at the 140 and $240\mu m$ were also able to provide information on very cold dust (VCD). At these wavelengths, the mass and temperature of VCD can be derived. When these data were joined with 60 and $100\mu m$ data taken from IRAS, it was found that the far-infrared luminosity arises from cold ($\approx 1722K$) dust associated with diffuse HI cirrus clouds, 15-30% from cold ($\approx 19K$) dust associated with molecular gas,

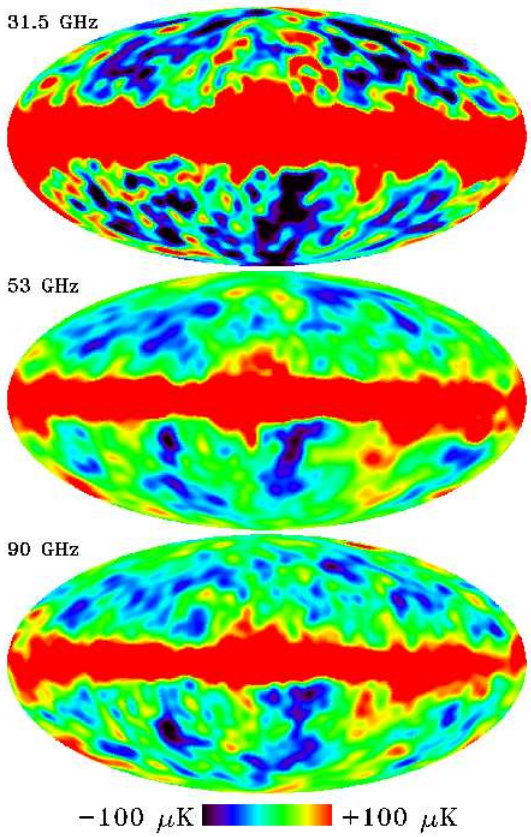

Figure 3.7: *Data obtained at each of the three DMR frequencies 31.5, 53, and 90 GHz following dipole subtraction.*

and less than 10% from warm ($\approx 29K$) dust in the extended low-density HII regions.

The objective of the FIRAS [34] instrument was to measure precisely the CMB spectrum and to observe the dust and line emission from the Galaxy. It covers the wavelength range from 0.1 to 10 mm in two spectral channels separated at 0.5 mm and has approximately 5% spectral resolution. A flared horn antenna aligned with the COBE spin axis gives the FIRAS a 7 degree field of view. Original CMB measurement results gave a CMB temperature of $2.726 \pm 0.010K$ over the wavelength range from 0.5 to 5 mm. Over this range the maximum deviation from the blackbody form is less than 0.03%, with a weighted rms value of only 0.01%. The dipole anisotropy of the CMB, presumed due to our peculiar motion relative to the Hubble flow, can be seen clearly in the FIRAS data, which show for the first time that the spectrum of the dipole is that expected from the Doppler shift acting on a blackbody spectrum. FIRAS results also

include the first nearly all-sky, unbiased, far infrared survey of the Galactic emission at wavelengths greater than $120\mu m$. The total far infrared luminosity of the Galaxy is inferred to be $1.8(\pm 0.6) \times 10^{10} L_{Sun}$.

Spectral lines from interstellar [C I], [C II], [N II], and CO were detected, and the lines of [C II] at 158 microns and [N II] at 205.3 microns were sufficiently strong to be mapped. This is the first observation of the 205.3 micron line. The [C II] line is interpreted as coming from photodissociation regions and the [N II] line as partially arising from a diffuse warm ionized medium and partially arising from dense H II regions.

The final FIRAS CMB spectrum measurements, using an improved understanding of the FIRAS calibrator, give the definitive CMB temperature: $2.725 \pm 0.002K$ [35].

3.3.2 The Wilkinson Microwave Anisotropy Probe (WMAP)

The Wilkinson Microwave Anisotropy Probe also known as the Microwave Anisotropy Probe (MAP), and Explorer 80 is a spacecraft which measures differences in the temperature of the CMB across the full sky (Fig. 3.1). Headed by Professor Charles L. Bennett, Johns Hopkins University, the mission was developed in a joint partnership between the NASA Goddard Space Flight Center and Princeton University. The WMAP spacecraft was launched on 30 June 2001, at 19:46:46 GDT, from Florida. In 2003, it was renamed WMAP in honor of David Todd Wilkinson (1935-2002), who had been a member of the mission's science team.

The WMAP measures the temperature differences in the CMB radiation. The anisotropies then are used:

- to measure universe's geometry, content, and evolution;
- to test the Big Bang model;
- to test the cosmic inflation theory.

For that, the mission is creating a full-sky map of the CMB, with a 13 arcminute resolution via multi-frequency observation. The map requires the fewest systematic errors, no correlated pixel noise, and accurate calibration, to ensure angular-scale accuracy greater than its resolution. The map contains 3,145,728 pixels, and uses the HEALPix scheme to pixelize the sphere. The telescope also measures the CMB's E-mode polarization and foreground polarization.

In 8 years, three different data releases were produced. The first, based upon one year worth of WMAP data, were produced on 11 February 2003, containing the latest calculated age, composition, and image of the universe.

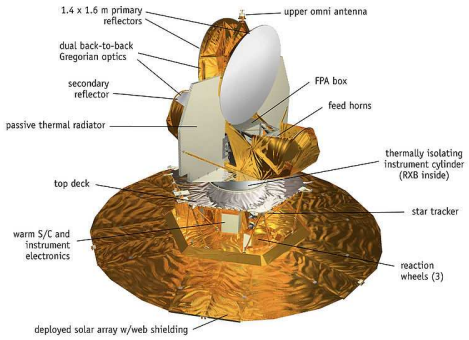

Figure 3.8: *WMAP spacecraft diagram*

The three-year WMAP data were released on 17 March 2006. The data included temperature and polarization measurements of the CMB, which provided further confirmation of the standard flat Lambda-CDM model and new evidence in support of inflation.

The five-year WMAP data were released on 28 February 2008. The data included new evidence for the cosmic neutrino background, evidence that it took over half a billion years for the first stars to reionize the universe, and new constraints on cosmic inflation. The improvement in the results came from both having an extra 2 years of measurements (the data set runs between midnight on 10 August 2001 to midnight of 9 August 2006), as well as in using improved data processing techniques and a better characterization of the instrument, most notably of the beam shapes. They also make use of the 33 GHz observations for estimating cosmological parameters; previously only the 41 GHz and 61 GHz channels had been used. Finally, improved masks were used to remove foregrounds. The measurements put constraints on the content of the universe at the time that the CMB was emitted; at the time 10% of the universe was made up of neutrinos, 12% of atoms, 15% of photons and 63% dark matter. The contribution of dark energy at the time was negligible.

In the following table, cosmological parameters calculated starting from WMAP data (also combined with measurements from Type Ia supernova (SNe) and Baryon acoustic oscillations (BAO)) are shown.

3.3.3 Planck

Planck is the latest space observatory designed to observe the CMB, using high sensitivity and angular resolution (Fig. 3.9). Planck was built in the Cannes Mandelieu Space Center by Thales Alenia Space and created as the third Medium-Sized Mission (M3) of

Parameter	Symbol	Best fit (WMAP only)	Best fit (WMAP + SNe + BAO)
Hubble's constant ($^{km}/_{Mpc \cdot s}$)	H_0	$71.9\ ^{+2.6}_{-2.7}$	70.5 ±1.3
Baryonic content	$\Omega_b h^2$	0.022 73 ±0.000 62	$0.022\ 67\ ^{+0.000\ 58}_{-0.000\ 59}$
Cold dark matter content	$\Omega_c h^2$	0.1099 ±0.0062	0.1131 ±0.0034
Dark energy content	Ω_Λ	0.742 ±0.030	0.726 ±0.015
Optical depth to reionization	τ	0.087 ±0.017	0.084 ±0.016
Scalar spectral index	n_s	$0.963\ ^{+0.014}_{-0.015}$	0.960 ±0.013
Running of spectral index	dn_s / $dlnk$	−0.037 ±0.028	−0.028 ±0.020
Fluctuation amplitude at $8h^{-1}$ Mpc	σ_8	0.796 ±0.036	0.812 ±0.026
Age of the universe (Ga)	t_0	13.69 ±0.13	13.72 ±0.12
Total density of the universe	Ω_{tot}	$1.099\ ^{+0.100}_{-0.085}$	$1.0050\ ^{+0.0060}_{-0.0061}$
Tensor-to-scalar ratio	r	< 0.43	< 0.22

Table 3.2: *Best-fit cosmological parameters from WMAP five-year results*

the European Space Agency's Horizon 2000 Scientific Programme. The projectm, initially called COBRAS/SAMBA after its approval, is named in honour of the German scientist Max Planck (1858-1947).

Figure 3.9: *The Planck satellite*

The satellite was successfully launched, along with the Herschel Space Observatory, at 13:12:02 on 14 May 2009 aboard an Ariane 5 ECA heavy launch vehicle. The launch placed the craft into a very elliptical orbit (perigee: 270 km, apogee: more than 1,120,000 km), bringing it near the L2 Lagrangian point of the Earth-Sun system, 1.5 million kilometers from the Earth. The maneuver to inject Planck into its final orbit around L2 was

successfully completed on July 3, 2009, when it entered a Lissajous orbit of 400,000 km radius around the L2 Lagrangian point.

The spacecraft carries two instruments; the Low Frequency Instrument (LFI) and the High Frequency Instrument (HFI). Both instruments can detect both the total intensity and polarization of photons, and together cover a frequency range of 30 to 857 GHz.

On September 2009, ESA announced the preliminary results from the Planck First Light Survey (performed to demonstrate the stability of the instruments and the ability to calibrate them over long periods). This results indicate that the data quality is excellent.

The final results (with all processed data) are expected to be delivered to the world-wide community towards the end of 2012.

Chapter 4

Phase transitions and Topological Defects

The Hot Big Bang model with a Friedmann-Lemaître-Robertson-Walker (FLRW) metric, as seen in chapter 2, is able to explain several features which characterize the evolution of Universe: (i) the expansion of the Universe, (ii) the origin of the cosmic background radiation, (iii) the synthesis of light elements, and (iv) the formation of large-scale structures. However, there are questions, which mainly concern the initial conditions, to which the Hot Big Bang model has been so far unable to provide correct answers. Possible answers to these issues can instead be found by introducing the idea of inflation. Inflation essentially consists of a phase of accelerated expansion, corresponding to repulsive gravity and an equation of state $3p < -\rho$, which took place at a very high energy scale. From the observational point of view, the remarkable uniformity of the CMB indicates that at the epoch of last scattering the Universe was isotropic and homogeneous, with a high degree of precision (10^{-5}). At very large scale, Universe is smooth, while at small scales today we observe large inhomogeneities.

For almost two decades, two families of models have been considered challengers for describing, within the framework of gravitational instability, the formation of large-scale structure in the Universe. Initial density perturbations can either be due to *freezing in* of quantum fluctuations of a scalar field during an inflationary period, or they may be seeded by a class of topological defects, which could have formed naturally during a symmetry breaking phase transition in the early Universe.

4.1 Inflation

The concept of inflation was introduced by Guth in 1981 [36], in order to solve a number of cosmological puzzles, particularly the horizon, flatness and monopole problems.

1. **Horizon problem:** since the Universe is of finite age, there is at any epoch t a *particle horizon* and no signal from beyond the horizon can yet have reached us. In the radiation dominated era of the standard FRW Universe, the particle horizon at time t is of radius $2t$. When we observe the cosmic microwave background radiation coming to us from opposite directions in the sky, we are seeing light

emitted from regions that were then separated by nearly 100 times the horizon distance at that time. It therefore seems very surprising that the temperature of the radiation coming from opposite directions is the same: no causal process could have established thermal equilibrium between such distant parts of the Universe.

2. **Flatness problem:** the value of Ω, defined in (2.11), is very close to unity, which implies that the Universe is flat. It is easy to verify that $\Omega = 1$ is an unstable point of the FRW evolution equation (2.9). To have Ω close to 1 today, it must have been very close indeed at early times.

3. **Monopole problem:** almost all grand unified theories predict the existence of ultra-heavy stable magnetic monopoles. Once formed, they are very hard to eliminate and so would rapidly come to dominate the energy density of the Universe, exceeding by many orders of magnitude the energy density in baryons.

All these problems can be cured by invoking the idea of inflation, a very early period of rapid expansion in which the energy density is dominated by "vacuum energy". This is achieved by introducing a scalar inflaton field σ with an appropriately chosen potential $V(\sigma)$. The energy density and pressure due to such a field in a FRW background are given by

$$\rho = \tfrac{1}{2}\dot{\sigma} + \tfrac{1}{2}a^{-2}(\nabla\sigma)^2 + V(\sigma)$$
$$p = \tfrac{1}{2}\dot{\sigma} - \tfrac{1}{6}a^{-2}(\nabla\sigma)^2 - V(\sigma).$$

If these equations are dominated by the potential term (in some sufficiently large region), then the equation of state is $p \approx -\rho$. It follows that $\rho \approx constant$ and hence, by (2.9), that the scale factor $a(t)$ increases exponentially. Actually, ρ is not exactly constant. The field σ does evolve slowly, eventually reaching a point where the conditions for inflation are no longer satisfied, bringing the period of rapid expansion to an end. During the period of accelerating expansion $\Omega \to 1$, thus solving the flatness problem. The horizon problem is also cured: during inflation, the causal horizon distance increases by a huge factor, so that the entire presently visible Universe was originally well within a single horizon volume. Finally, the expansion dilutes the density of any previously existing monopoles to an undetectably low level. Unfortunately, inflation also dilutes any other topological defects, in particular cosmic strings. At first sight, therefore, the two ideas are indeed mutually incompatible. However, it is possible to reconcile the two with models in which strings or other defects are formed during the late stages of inflation.

4.2 Topological defects

The Universe has steadily cooled down since the Planck time, leading to a series of Spontaneously Symmetry Breaking (SSB), which might have lead to the creation of topological defects.

The formation or not of topological defects during the phase transitions, followed by SSB, and the determination of the type of the defects, depends on the topology of the vacuum manifold M. The properties of M are usually described by the k^{th} homotopy group $\pi_k(M)$, which classifies distinct mappings from the k-dimensional sphere S^k into the manifold M. To illustrate that, let us consider the symmetry breaking of a group G, down to a subgroup H of G . If M= G/H has disconnected components, or equivalently, if the order k of the nontrivial homotopy group is $k = 0$, then two-dimensional defects called *domain walls*, form. The spacetime dimension d of the defects is given in terms of the order of the nontrivial homotopy group by $d = 4 - 1 - k$. If M is not simply connected, in other words if M contains loops which cannot be continuously shrunk into a point, then *cosmic strings* form. A necessary, but not sufficient, condition for the existence of stable strings is that the first homotopy group (the fundamental group) $\pi_1(M)$ of M, is nontrivial, or multiply connected. Cosmic strings are line-like defects, $d = 2$. If M contains unshrinkable surfaces, then *monopoles* form, for which $k = 1$, $d = 1$. If M contains noncontractible three-spheres, then event-like defects, *textures*, form for which $k = 3$, $d = 0$ (Tab. 4.1).

Homotopy π_n	Defect	Dim d	Appearance
$\pi_0(M) \neq 0$, M disconnected	walls	$d = 3$	sheets in space
$\pi_1(M) \neq 0$, M with non shrinkable circles	strings	$d = 2$	lines in space
$\pi_1(M) \neq 0$, M with non shrinkable 2-spheres	monopoles	$d = 1$	points in space
$\pi_3(M) \neq 0$, M with non shrinkable 3-spheres	textures	$d = 0$	events in spacetime

Table 4.1: *Topological defects in four dimensional spacetime.*

Topological defects are also very well known in solid state physics. For example the vortex lines in type II super conductors are nothing else than the equivalent of cosmic strings. Also in liquid crystals (Fig. 4.1) or super fluid Helium, a variety of topological defects form during symmetry breaking phase transitions.

The defects are called **local** if a gauge symmetry is broken and **global** if they emerge

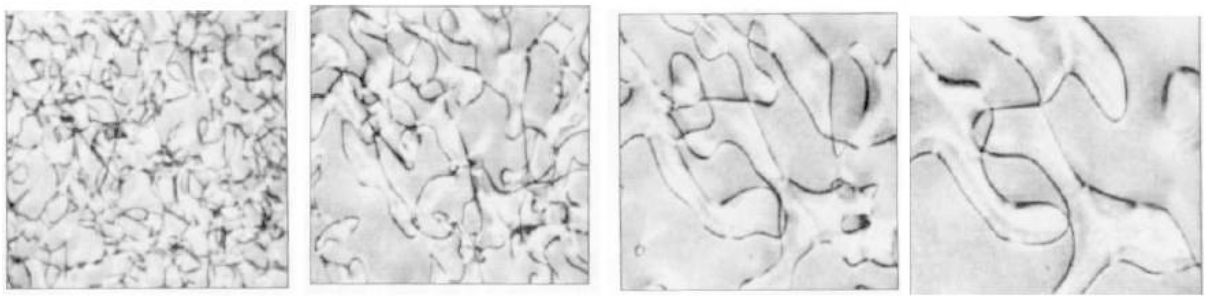

Figure 4.1: *A scaling sequence of a string network in a nematic liquid crystal after the isotropic - nematic phase transition. Time runs from left to right.*

from global symmetry breaking. The energy of local defects is strongly confined, while the gradient energy of global defects is spread out over the causal horizon at defect formation. Patterns of symmetry breaking which lead to the formation of local monopoles or local domain walls are ruled out, since they should soon dominate the energy density of the Universe and close it, unless an inflationary era took place after their formation.

Local textures are insignificant in cosmology since their relative contribution to the energy density of the Universe decreases rapidly with time. Even if the nontrivial topology required for the existence of a defect is absent in a field theory, it may still be possible to have defect-like solutions. Defects may be embedded in such topologically trivial field theories. While the stability of topological defects is guaranteed by topology, embedded defects are in general unstable under small perturbations.

4.2.1 Simmetry breaking

Spontaneous symmetry breaking is an idea originated from condensed matter physics. A familiar example is the isotropic model of a ferromagnet which, although described by a rotationally-invariant Hamiltonian, can develop a magnetic moment pointing in some arbitrary direction. In modern theories of elementary particles, symmetry breaking is described in terms of scalar fields, usually called Higgs fields. The symmetry is said to be spontaneously broken if the ground state is characterised by a nonzero expectation value of the Higgs field and does not exhibit the full symmetry of the Hamiltonian.

To examplify the idea of SSB let us consider the simple Goldstone model. Let ϕ be a complex scalar field with classical Lagrangian density

$$\mathscr{L} = (\partial_\mu \bar{\phi})(\partial^\mu \phi) - V(\phi) \tag{4.1}$$

and the potential $V(\phi)$, (Fig. 4.2)

$$V(\phi) = \frac{1}{4}\lambda[\bar{\phi}\phi - \eta^2]^2, \tag{4.2}$$

where λ and η are positive constants.

This model is invariant under the $U(1)$ group of global phase transformations (the phase is independent of the spacetime location),

$$\phi(x) \longrightarrow e^{i\alpha}\phi(x). \tag{4.3}$$

The potential (4.2) has minima lieing on a circle $|\phi| = \eta$; the ground state of the theory is characterised by a nonzero expectation value, given by

$$\langle 0\,|\phi|\,0\rangle = \eta e^{i\theta} \tag{4.4}$$

with an arbitrary phase θ. The phase transformation (4.3) changes θ into $\theta + \alpha$. Hence, the vacuum state $|0\rangle$ is not invariant under under the phase transformation (4.3) and the symmetry is spontaneously broken.

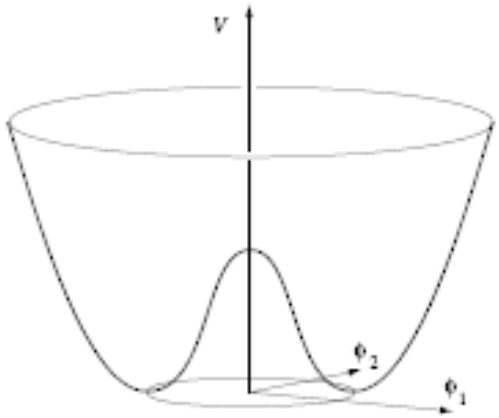

Figure 4.2: *The Mexican-hat potential for a broken $U(1)$ symmetry showing a degenerate circle of minima.*

The state of unbroken symmetry with $\langle 0\,|\phi|\,0\rangle$ corresponds to a local maximum of $V(\phi)$. All broken symmetry vacua, each with a different value of the phase θ are equivalent. Therefore, choosing the vacuum with $\theta = 0$, we can represent ϕ as

$$\phi = \eta + \frac{1}{\sqrt{2}}(\phi_1 + i\phi_2), \tag{4.5}$$

where ϕ_1 and ϕ_2 are real fields with zero vacuum expectation values. Substituting the (4.5) into the Lagrangian (4.1),

$$\mathscr{L} = \frac{1}{2}(\partial_\mu \phi_1)^2 + \frac{1}{2}(\partial_\mu \phi_2)^2 - \frac{1}{2}\lambda\eta^2\phi_1^2 + \mathscr{L}_{int}.$$

The last term, $\mathscr{L}_{int}$, is an interaction term which includes cubic and higher-order terms in the real scalar fields ϕ_1 and ϕ_2. We see that ϕ_1 corresponds to a massive particle, with a positive mass $\sqrt{\lambda}\eta$, while ϕ_2 corresponds to a massless scalar particle, the Goldstone boson. The appearance of Goldstone bosons is a generic feature of models with spontaneously broken global symmetries.

Although global symmetries are of considerable interest, the central role in particle physics is played by gauge theories with spontaneously broken symmetries. The simplest gauge theory example, known as the abelian-Higgs model, describes scalar electrodynamics with Lagrangian

$$\mathscr{L} = \mathscr{D}_\mu \phi \mathscr{D}^\mu \phi - \frac{1}{4}F_{\mu\nu}F^{\mu\nu} - V(\phi), \tag{4.6}$$

where ϕ is a complex scalar field and the covariant derivative is given by $\mathscr{D}_\mu = \partial_\mu - ieA_\mu$, with A_μ a gauge vector field. The antisymmetric tensor is $F_{\mu\nu} = \partial_\mu A_\nu - \partial_\nu A_\mu$, with e the gauge coupling, and $V(\phi)$ given by (4.2). The abelian-Higgs model is invariant under the group $U(1)$ of local gauge transformations

$$\phi(x) \to e^{i\alpha(x)}\phi(x), \quad A_\mu(x) \to A_\mu(x) + e^{-1}\partial_\mu \alpha(x).$$

The minima of the Mexican hat potential $V(\phi)$, lie on a circle of fixed radius $|\phi| = \eta$, implying that the symmetry is spontaneously broken and the complex scalar field ϕ acquires a nonzero vacuum expectation value. Following the same approach as in the Goldstone model, we can represent ϕ as $\phi = \eta + \phi_1/\sqrt{2}$, obtaining

$$\mathscr{L} = \frac{1}{2}(\partial_\mu \phi_1)^2 - \frac{1}{2}\mu^2\phi_1^2 - \frac{1}{4}F_{\mu\nu}F^{\mu\nu} + \frac{1}{2}M^2 A_\mu A^\mu + \mathscr{L}_{int},$$

where the particle spectrum contains a scalar particle (Higgs boson) with mass $m_s = \mu = \sqrt{\lambda}\eta$ and a vector field (gauge boson) with mass $m_v = M = \sqrt{2}e\eta$. The breaking of a gauge symmetry does not imply a massless Goldstone boson.

The abelian-Higgs model is the simplest model which admits string solutions, the Nielsen-Olesen vortex lines. The width of the string is determined by the Compton wavelength of the Higgs and gauge bosons, which is $\sim m_s^{-1}$ and $\sim m_v^{-1}$, respectively.

4.2.2 Thermal phase transitions and defect formation

In analogy to condensed matter systems, a symmetry which is spontaneously broken at low temperatures can be restored at higher temperatures. In field theories, the expectation value of the Higgs field ϕ can be considered as a Bose condensate of Higgs

particles. If the temperature T is nonzero, one should consider a thermal distribution of particles/antiparticles, in addition to the condensate. Minimising the free energy $F = E - TS$, we can obtain the equilibrium value of the Higgs field ϕ. Only at high enough temperatures the free energy is effectively temperature-dependent, while at low temperatures the free energy is minimised by the ordered state of the minimum energy. Let us consider for example the Goldstone model, for which the high-temperature effective potential is

$$V_{eff}(\phi, T) = m^2(T)\,|\phi|^2 = \frac{\lambda}{4}\,|\phi|^4\,, \quad m^2(T) = \frac{\lambda}{12}(T^2 - 6\eta^2).$$

The effective mass-squared term $m^2(T)$ for the Higgs field ϕ in the symmetric state $\langle\phi\rangle = 0$, vanishes at the critical temperature $T_c = 6\eta^2$. The effective potential is calculated using perturbation theory and the leading contribution comes from one-loop Feynman diagrams. For a scalar theory, the main effect is a temperature-dependent quadratic contribution to the potential. Above the critical temperature, $m^2(T)$ is positive, implying that the effective potential gets minimised at $\phi = 0$, resulting to a symmetry restoration. Below the critical temperature, the effective mass-squared term is negative, implying that the Higgs field has a nonvanishing expectation value.

Even if there is symmetry restoration and the mean value $\langle\phi\rangle = 0$, the actual value of the field ϕ fluctuates around the mean value, meaning that ϕ at any given point is nonzero. The thermal fluctuations have, to a first approximation, a Gaussian distribution, thus they can be characterised by a two-point correlation function, which typically decays exponentially, with a decay rate characterised by the *correlation length* ξ. The consequence of this is that fluctuations at two points separated by a distance greater than the correlation length ξ are independent.

Kibble [1] was first to estimate the initial density of topological defects formed after a phase transition followed by SSB in the context of cosmology. His criterion was based on the causality argument and the Ginzburg temperature, T_G[1],

$$\xi^3(T_G)\Delta F(T_G) \sim T_G,$$

being ΔF the difference in free energy density between the false and true vacua. According to the Kibble mechanism, the initial defect network is obtained by the equilibrium correlation length of the Higgs field at the Ginzburg temperature. Consequently, laboratory tests confirmed defect formation at the end of a symmetry breaking phase transition, but they disagree with defect density estimated by Kibble.

[1]The Ginzburg temperature is defined as the temperature below which thermal fluctuations do not contain enough energy for regions of the field on the scale of the correlation length to overcome the potential energy barrier and restore the symmetry

4.2.3 Topological defects in the Universe

In this section, we shall briefly describe the possible topological defects formed in the early Universe. As mentioned above, according to the topology of the vacuum manifold M, defects can be

1. domain walls;
2. strings;
3. monopoles;
4. textures.

Domain walls

The appearance of domain walls is generally associated with the breaking of a discrete symmetry. The vacuum manifold M then consists of several disconnected components. Domain walls occur at the boundaries between regions of space with values of the field ϕ in different components, with ϕ interpolating between these two values across the wall.

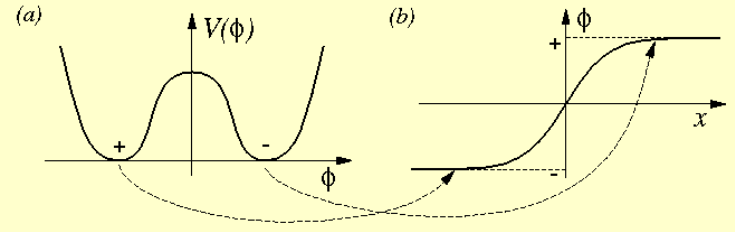

Figure 4.3: *Domain walls are associated with models in which there is more than one separated mimimum.*

The domain wall appearing in the simplest Goldstone model with the double-well potential depicted in Fig. 4.3. The width of the wall is approximately

$$\delta \sim (\sqrt{\lambda}\eta)^{-1}.$$

With a vacuum energy $\rho \sim \lambda\eta^4$ at the center of the wall, the surface energy density will be

$$\sigma \sim \rho\delta \sim \sqrt{\lambda}\eta^3.$$

Unless the symmetry breaking scale η is very small, this surface density is extremely large and implies that cosmological domain walls would have an enormous impact on the homogeneity of the Universe.

Strings

If the vacuum manifold *M* has one dimensional closed paths that cannot be contracted, there are topological string solutions in the field theory. The homotopy group $\pi_1(G/H)$ is the group formed by the equivalence classes of paths that can be deformed into each other and the group operation joins two paths to get another path. Each element of $\pi_1(G/H)$ labels a topologically distinct string solution.

An example of a field theory in which string solutions exist is based on a $U(1)$ (global or local) group which is broken down completely in the abelian-Higgs model (4.6). In the Lorentz gauge, $\partial_\mu A^\mu = 0$, the Higgs field takes the form

$$\phi \approx \eta e^{in\theta}$$

where n is an integer, the string winding number. The gauge field asymptotically approaches

$$A_\mu \approx \frac{1}{ie}\partial_\mu \ln \phi.$$

It can be demonstrated, applying the Stokes' theorem around a closed path encircling a string, that the solution cannot everywhere be rotated to the vacuum by a regular gauge transformation if $n \neq 0$.

With these asymptotic forms, it results $D_\mu\phi \approx 0$ and $F_{\mu\nu} \approx 0$ far from the string core. As a result, the energy density vanishes rapidly (exponentially) away from the core and the total energy per unit length is finite. The lowest energy string configuration has unit winding number, $n = \pm 1$. The width of the string is determined by the Compton wavelengths of the Higgs and gauge bosons $\delta_\phi \approx m_s^{-1}$ and $\delta_A \approx m_v^{-1}$ (cfr. 4.2.1). The string mass per unit length is approximately

$$\mu \sim \eta^2. \tag{4.7}$$

For GUT scale strings with $\eta \sim 10^{16}\ GeV$, this corresponds to the mass density $\mu \sim 10^{22}\ g\ cm^{-1}$. Then it is clear that the string mass per unit length μ is a fundamental parameter for the study of strings properties and their research, as we can see more in details in chapters 5 and 6.

Monopoles

Pointlike defects or monopoles arise if the manifold of degenerate vacua contains non-contractible two-surfaces (like the sphere S^2). This corresponds to the vacuum manifold *M* having a nontrivial second homotopy group $\pi_2(M) \neq I$. It is possible to demonstrate that a symmetry group G which breaks to leave a $U(1)$ symmetry intact,

$$G \longrightarrow K \times U(1),$$

must have monopole solutions. Grand unified models based on simple groups which break to leave the $U(1)_{em}$ of electromagnetism must therefore produce monopoles.

The simplest monopole is the 't Hooft-Polyakov solution which appears when $SU(2)$ is broken to $U(1)$. The three-component Higgs field far from the core of the monopole takes a "hedgehog" configuration (Fig. 4.4).

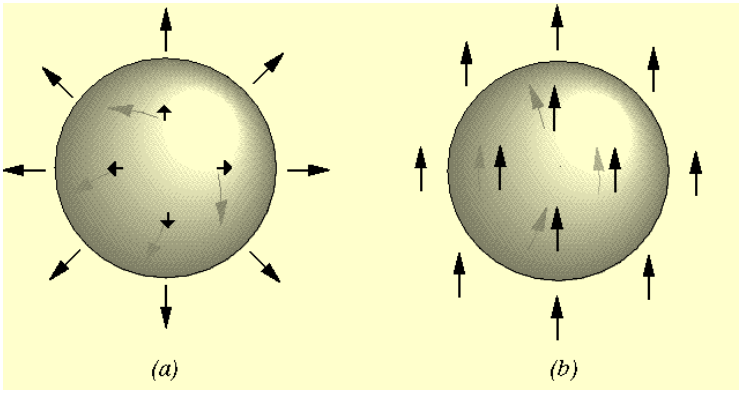

Figure 4.4: *Only the three-dimensional "hedgehog" configuration of (a) corresponds to a monopole.*

Textures

A texture is a configuration for which the field takes vacuum values everywhere but with a non trivial energy density due to the gradiant energy. In the language of algebraic topology, textures may appear when there are topologically nontrivial mappings from the three sphere S^3 into the vacuum manifold M. Textures are classified by the third homotopy group $\pi_3(M)$. They are sometimes termed non-singular solitons because the scalar field is nowhere topologically constrained to rise from the minimum of the potential $V(\phi)$.

In general textures are unstable since they like to shrink and then tunnel to a trivial vacuum state. To see this note that the energy of a texture goes as

$$E = \frac{1}{2}\int \partial^k \phi \cdot \partial_k \phi d^3x$$

If we scale $x \to \alpha x$ then the gradiant energy density goes as $1/\alpha^2$ but after the integration the energy scales like αE. Nevertheless there have been suggestions that textures are important for the formation of structure in the early universe, however the COBE measurements seem to have almost ruled this out as a scenario.

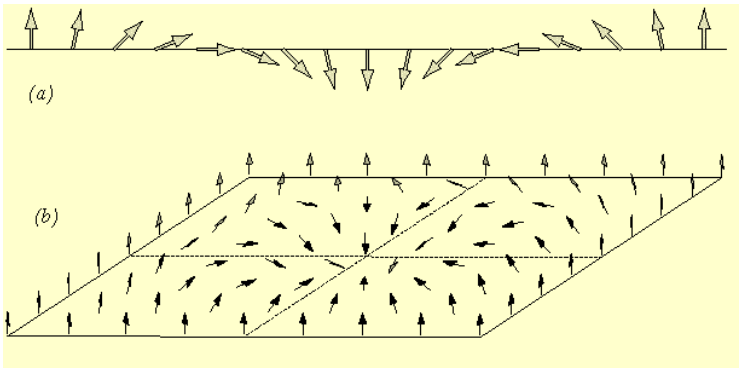

Figure 4.5: *Examples of delocalized texture configurations in one and two dimensions. The scalar field takes complex values, indicated by the phase vector in the diagram. As the field winds around the line it remains in the vacuum manifold* $|\phi| = \eta$.

Chapter 5

Cosmic Strings Theory

Cosmic strings are topological defects that, as mentioned in chapter 4, form whenever phase transitions in the early universe break axial symmetries, as originally shown by Kibble [1,37]. In short, it can be stated that cosmic strings are infinitely long and filamentary remnants of primordial dark energy which formed in the early Universe and were then stretched by the expansion of the Universe up to the point that, at present epoch, some cosmic string could cross the entire length of our observable Universe. For about two decades, motivation for their study was provided by the possibility that they could be behind the density inhomogeneities that led to the observed large-scale structures in the universe. Precision observations, particularly of the cosmic microwave background radiation, have limited strings to a sub-dominant role in structure formation. Instead, with respect to other topological defects, they find their natural explanation in the inflationary scenario and are fully predicted by a wide class of elementary particle models.

More recently, interest has been revived with the realization that there may be strong links between field theory cosmic strings, and fundamental strings. Fundamental strings are the supposed building blocks of all matter in superstring theory or its modern version, M-theory. Their behavior is expected to be quite similar to that of field theory cosmic strings, although there are some important differences that make them, at least in principle, be observationally distinguishable. Being relics of the phase transitions that produced them, cosmic strings provide us with a unique window into the early universe. If they are stable and survive for a significant amount of time, they may leave an imprint in many astrophysical and cosmological observables, and provide us with information on fundamental physics and the very early universe that would otherwise be inaccessible. The basic picture of the cosmological evolution of string networks that has emerged for the simplest (Goto- Nambu) networks is of a scaling solution with about 40 long strings always stretching across each horizon volume plus a population of loops (other string types can lead to a different behaviour).

These strings continuously source gravitational perturbations on sub-horizon scales. The one parameter in these models is the energy scale of the phase transition at which the strings are created. The astrophysical consequences of strings stem from the non-trivial gravitational field around a string [3].

The space-time around the string is locally, but not globally, flat. A string lying along

the z-direction has an equation of state $p_z = \ - \ \rho$, $p_x = p_y = 0$ and therefore there is no source term in the relativistic version of the Poisson equation for the Newtonian gravitational potential

$$\nabla^2\phi = 4\pi G(\rho + p_x + p_y + p_z) = 0.$$

and, therefore, particles in the vicinity of a static straight string feel no gravitational acceleration.

However, a moving string causes important effects on nearby matter or propagating photons. In fact the space-time metric around such a straight static string

$$ds^2 = dt^2 - dz^2 - dr^2 - r^2 d\theta^2$$

looks like a Minkowski space in cylindrical coordinates, except for the fact that θ has a restricted range $0 \leq \theta \leq 2\pi(1 - 4G\mu)$, where μ is the energy per unit length. Then the space-time is actually conical with a global *deficit angle*

$$\Delta = 8\pi\frac{G\mu}{c^4}. \tag{5.1}$$

The conical structure can be visualized as the euclidean space in which a wedge of angular size Δ is removed and its edges identified. The string passes through its vertex (Fig. 5.1).

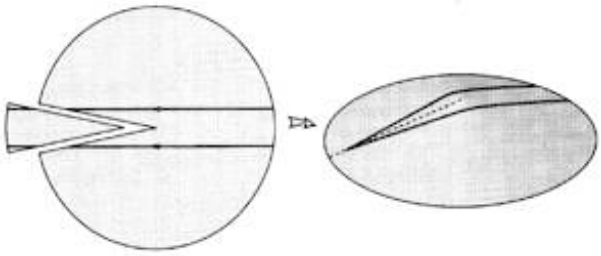

Figure 5.1: *The conical spacetime about a cosmic string is constructed by removing a wedge and identifying along its edges.*

As mentioned, the conical space-time, and hence the existence of a deficit angle, implies that the presence of a cosmic string can cause physical effects which are, at least in principle, observable. These effects will be discussed in next chapter.

5.1 Strings in the early Universe

As described in chapter 4, the simplest field theory model that produces cosmic strings has a single complex scalar field ϕ, which we can also think of as a pair of real fields $\phi_{1,2}$,

with $\phi = \phi_1 + i\phi_2$. It is assumed that that the Hamiltonian which defines the dynamics of the field is invariant under phase rotation $\phi \to \phi e^{i\alpha}$. In particular, there is a potential energy term V of the form (4.2), usually taken to be the "sombrero potential" (Fig. 4.2). At high temperatures the field fluctuations are large enough to make the central peak irrelevant, and the effective potential is symmetric with a minimum around $|\phi| = 0$. As the temperature falls, the energy will eventually become too low to permit fluctuations over the peak, at which point the field will tend to settle towards one of the ground states. The random choice of minimum in this condensation process then breaks the original axial symmetry.

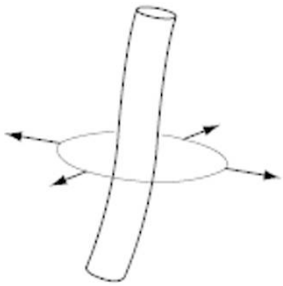

Figure 5.2: *A cosmic string. The directions of the arrows indicate the values of α. The field ϕ vanishes in the core of the string.*

When a phase transition like the one described above involves a large system, each part of it has to make a random choice of the phase angle α. Since there are terms in the energy involving the gradient of ϕ, the phase angle will tend to become more uniform as the system cools, but causality imposes that this evolution can only happen at a limited rate. As a result one expects many domains, each with an uncorrelated choice of ground state. This domains can meet, so having a finite probability of forming linear defects like cosmic strings (Fig. 5.2) around which the phase angle varies by 2π. The above is also known as the *Kibble mechanism*.

Field continuity implies that a string of this kind cannot simply come to an end: it must form a closed loop or extend to infinity (or at least beyond the region we can see), and it cannot break into segments. For this reason, strings, once formed, are hard to eliminate. The strings would eventually dominate the energy density of the universe, but energy loss mechanisms take place: the strings can decay into radiation, they may cross and exchange partners, and they may also cross themselves, forming a closed loop which may shrink and eventually disappear (Fig. 5.3). The outcome of these competing mechanisms is that the network is expected to reach a scale-invariant regime, where the network's characteristic length scale is proportional to the size of the horizon. If a random network of strings was formed in the early universe, there would always be

some strings longer than the horizon, so a few would remain even today.

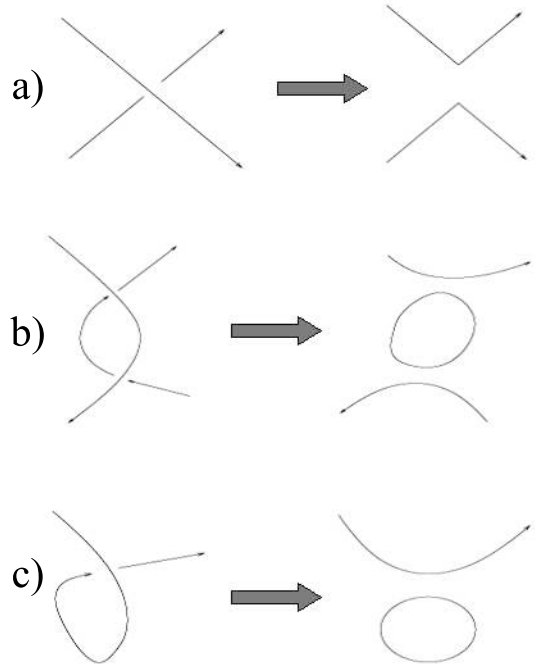

Figure 5.3: *Illustration of string intersections: (a) string-string intersection in one point, leading to the formation of two new long strings via exchange of partners; (b) string-string intersections in two points, leading to the formation of two new long strings via exchange of partners, and one closed loop; and (c) self-string intersections leading to the formation of one long string and a closed string loop.*

Since cosmic strings contain a large amount of trapped energy, in the late 80's and early 90's the possibility that they could significantly perturb the matter distribution was explored. To first order there is a single parameter quantifying the effects of strings, its energy per unit length. In the simple relativistic strings, the mass per unit length and the string tension μ/c^2 are equal, because of Lorentz invariance under boosts along the direction of the string. Cosmic strings are exceedingly thin, but very massive. Typically, for strings produced at a possible GUT transition, it is $\mu/c^2 \sim 10^{21}$ kg m-1 and the thickness is 10^{-24} m. The gravitational effects of strings are effectively governed by the dimensionless parameter $G\mu/c^4$, where G is the Newton constant. In particular, strings in the early universe would create density perturbations in which the fractional change in density is

$$\frac{\delta\rho}{\rho} \sim \frac{G\mu}{c^4},$$

that, for GUT-scale strings, is of order 10^{-6}. In what follows, we shall choose units in

which $c = 1$ and talk of the parameter $G\mu$. Unfortunately, as already it was mentioned, measurements made by the COBE and WMAP satellites have yielded very precise information about these anisotropies. In particular, the angular power spectrum shows a series of peaks, so-called "acoustic peaks" (see chapter 3), that the cosmic string scenario is not able to explain, unlike the theory of inflation. So the idea of cosmic strings as primarly sources of the density inhomogeneities has been ruled out.

5.1.1 Superstrings theory

Recently, however, there has been a revival of interest due to developments in our understanding of a very different kind of strings, the fundamental strings of the superstring theory, or its more modern incarnation, M-theory.

Superstring theory is to date the only candidate model for a consistent quantum theory of gravity that includes all other known interactions. In string theory, the fundamental constituents of nature are not point-like particles but one-dimensional "strings" whose vibrational modes produce all elementary particles and their interactions. Two important features of the theory are supersymmetry (a symmetry between bosonic and fermionic excitations that keeps quantum effects under control) and the presence of extra dimensions above the four spacetime dimensions that we observe.

In the M-theory, strings are not the only localized objects. There can be two-dimensional "membrane" or their higher-dimensional analogues, which have come to be known as *"p-branes"* (of dimension p) a particle is a 0-brane, a string a 1-brane, and so on. We have D-branes (or Dp-branes), where the D denotes the Dirichlet boundary conditions[1]. Essentially this means that in addition to closed loops of fundamental string there may be open strings whose ends are tied to D-branes. There are also anti-branes, $\overline{\text{D}}$-branes. A Dp brane and a $\overline{\text{D}p}$ have equal and opposite conserved charges, which means that they attract each other. Open strings usually give rise to matter fields while gravity comes from closed loops. This means that matter may be trapped on a Dp-brane while gravity feels all the extra dimensions [38].

The conceptual discovery of branes and their role in more exotic compactifications, where the six compact dimensions have strong gravitational potentials (and redshifts), have solved many open question of the previous theories. For example, one of the main motivations behind the brane-world scenario was to try to explain the vast difference between the Planck scale of gravity of 10^{19} GeV and the electroweak scale, which mediates radioactive decay, of 10^2 GeV. The idea was to introduce warped space-time. When space-time is warped, the invariant distance defined in special relativity, $ds^2 = dt^2 - dx^2$,

[1]The Dirichlet (or first-type) boundary condition is a type of boundary condition that, imposed on an ordinary or a partial differential equation, specifies the values a solution needs to take on the boundary of the domain.

becomes

$$ds^2 = e^{-A(\underline{y})}(dt^2 - dx^2) - d\underline{y}^2$$

where $\underline{y}$ represents the extra dimensions and $A(\underline{y})$, the "warp" factor, is a known, positive function. The warp factor is essentially a gravitational red-shift in the compact directions. In five-dimensional brane worlds this warping of space-time was used to generate a hierarchy of scales such that gravity, which propagates on both the brane and in the bulk, could be at the Planck scale whilst the usual physics, confined to the brane, could have an energy scale much smaller than this. However, the warping of space-time is more general than brane-worlds and arises in many string theory models where there are 6 compact extra dimensions. There are particular solutions in which the warp factor varies strongly as a function of the compact dimensions, $\underline{y}$, with special regions known as *throats* where it falls sharply to very small values (Fig. 5.4).

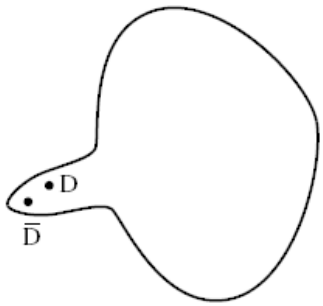

Figure 5.4: *Space with throat. In the middle we have the compactified space, with the throat on the left of the figure. The $D/\overline{D}$ branes are in the throat.*

This means that, for a four-dimensional observer the fundamental string mass per unit length would appear to be

$$\mu = e^{-A(\underline{y})}\mu_0$$

where μ_0 is the ten-dimensional scale. Consequently fundamental strings may not be at such high energies after all, even if μ_0 is at the Planck scale.

It is now believed that networks of cosmic superstrings could be a natural outcome of brane-antibrane annihilation, especially if the branes are responsible for a period of cosmic inflation [39–42].

Consider a Universe containing an extra brane and anti-brane. The brane and anti-brane are attracted to each other in the same way as an electron and positron are. However, when they annihilate, they give rise to lower-dimensional branes rather than photons. If the early universe contained an extra brane and anti-brane separated in the

compact dimension, then the distance between them plays the role of a scalar field, called the inflaton. The potential energy of these branes drives the exponential expansion and therefore the inflation. As the branes approach, the potential between them becomes steeper before they annihilate. Once they annihilate, lower dimensional branes are formed. It was shown that D-strings were generically formed in brane inflation [39].

5.2 Cosmic strings dynamics

The world history of a string can be expressed by a two-dimensional surface in the four-dimensional spacetime, which is called the string worldsheet:

$$x^\mu = x^\mu(\zeta^a), \quad a = 0, 1,$$

where ζ_0 and ζ_1 correspond to, respectively, the timelike ($\equiv \tau$) and spacelike ($\equiv \sigma$) worldsheet coordinates.

The motion of a cosmic string is obtainable from a variational principle applied to the Goto-Nambu action [43,44] which, up to an overall factor, corresponds to the surface area swept out by the string in spacetime

$$S_0[x^\mu] = -\mu \int \sqrt{-\gamma} d^2\zeta, \tag{5.2}$$

where γ is the determinant of the two-dimensional worldsheet metric γ_{ab},

$$\gamma = \det(\gamma_{ab}) = \frac{1}{2}\epsilon^{ac}\epsilon^{bd}\gamma_{ab}\gamma_{cd}, \quad \gamma_{ab} = g_{\mu\nu}x^\mu_{,a}x^\nu_{,b}. \tag{5.3}$$

Note that if the string curvature is small but not negligible, one may consider an expansion in powers of the curvature.

By varying equation (5.2), with respect to $x^\mu(\zeta^a)$, and using the relation $d\gamma = \gamma\gamma^{ab}d\gamma_{ab}$, one gets the string equations of motion

$$x^\mu_{,a}{}^{;a} + \Gamma^\mu_{\nu\sigma}\gamma^{ab}x^\nu_{,a}x^\sigma_{,b} = 0, \tag{5.4}$$

where $\Gamma^\mu_{\nu\sigma}$ is the four-dimensional Christoffel symbol,

$$\Gamma^\mu_{\nu\sigma} = \frac{1}{2}g^{\mu\tau}(g^{\tau\nu,\sigma} + g^{\tau\sigma,\nu} - g^{\nu\sigma,\tau}),$$

and the covariant Laplacian is

$$x^\mu_{,a}{}^{;a} = \frac{1}{\sqrt{-\gamma}}\partial_a(\sqrt{-\gamma}\gamma^{ab}x^\mu_{,b}).$$

To consider the scattering of thermal particles off the string, the equation of motion has to modified including a force of friction $F^{\mu\nu}$ [45], depending on the temperature of the surrounding matter T , the velocity of the fluid transverse to the world sheet $u^{\lambda}_{\perp} \equiv u^{\nu} - x^{\nu}_{,a} x^{\sigma,\alpha} u_{\sigma}$, and the type of interaction between the particles and the string, which can be represented by σ:

$$\mu[x^{\mu}_{,a}{}^{;a} + \Gamma^{\mu}_{\nu\sigma} x^{\nu}_{,a} x^{\sigma}_{,b}] = F^{\mu}(u^{\lambda}_{\perp}, T, \sigma)$$

Cosmic strings of mass per unit length μ would have formed at cosmological time

$$t_0 \sim (G\mu)^{-1} t_{Pl}$$

where t_{Pl} is the Planck time. Immediately after the phase transition the string dynamics would be dominated by friction, until a time of order

$$t_* \sim (G\mu)^{-2} t_{Pl}.$$

For cosmic strings formed at the grand unification scale, $G\mu \sim 10^{-6}$, so that friction is important only for a very short period of time. However, if strings have formed at a later phase transition, for example closer to the electroweak scale for which $G\mu \sim 10^{-34}$, their dynamics would be dominated by friction through most of the thermal history of the Universe.

The string energy-momentum tensor can be obtained by varying the action, equation (5.2), with respect to the metric $g_{\mu\nu}$,

$$T^{\mu\nu}\sqrt{-g} = -2\frac{\delta S}{\delta g_{\mu\nu}} = \mu \int d^2\zeta \sqrt{-\gamma}\gamma^{ab} x^{\mu}_{,a} x^{\nu}_{,b} \delta^{(4)}(x^{\sigma} - x^{\sigma}(\zeta^a)).$$

For a straight cosmic string in a flat spacetime lying along the z-axis and choosing $\zeta_0 = t$ and $\zeta_1 = z$, the above expression reduces to the one for the effective energy-momentum tensor,

$$\tilde{T}^{\mu}_{\nu} = \mu\delta(x)\delta(y)diag(1, 0, 0, 1).$$

The equations of motion for strings are most conveniently written in comoving coordinates, where the FLRW metric takes the form (2.4). The comoving spatial coordinates of the string, $\mathbf{x}(\tau, \sigma)$ are written as a function of conformal time τ and the length parameter σ. For a cosmic string moving in a FLRW Universe, the equations of motion, Eq. (5.4), can be simplified by choosing both the gauge condition $\zeta_0 = \tau$, and the gauge in which the unphysical parallel components of the velocity vanish,

$$\dot{\mathbf{x}} \cdot \mathbf{x}' = 0,$$

where overdots denote derivatives with respect to τ and primes denote spatial derivatives with respect to σ.

In these coordinates, the Goto-Nambu action yields the following equations of motion for a string moving in a FLRW metric

$$\ddot{\mathbf{x}} + 2\left(\frac{\dot{a}}{a}\right)\dot{\mathbf{x}}(1-\dot{\mathbf{x}}^2) = \left(\frac{1}{\epsilon}\right)\left(\frac{\mathbf{x}'}{\epsilon}\right)'. \tag{5.5}$$

The string energy per unit σ, in comoving units, is $\epsilon \equiv \sqrt{\mathbf{x}'/(1-\dot{\mathbf{x}}^2)}$, implying that the string energy is $\mu a \int \epsilon d\sigma$. Equation (5.5) leads to [46]

$$\frac{\dot{\epsilon}}{\epsilon} = -2\frac{\dot{a}}{a}\dot{\mathbf{x}}^2.$$

One usually fixes entirely the gauge by choosing σ so that initially $\epsilon = 1$.

In flat spacetime spacetime, the string equations of motion take the form

$$\partial_a(\sqrt{-\gamma}\gamma^{ab}x^{\mu}_{,b}) = 0.$$

In the conformal gauge (overdots and primes denote derivatives with respect to ζ^0 and ζ^1, respectively),

$$\dot{x}\cdot x' = 0\ ,\ \dot{x}^2 + x'^2 = 0, \tag{5.6}$$

the string equations of motion is just a two-dimensional wave equation,

$$\ddot{\mathbf{x}} - \mathbf{x}'' = 0, \tag{5.7}$$

To fix entirely the gauge, one also imposes $t \equiv x^0 = \zeta^0$, which allows us to write the string trajectory as the three dimensional vector $\mathbf{x}(\sigma, t)$, where $\zeta^1 = \sigma$. This implies that the constraint equations (5.6) and the string equations of motion (5.7) become

$$\begin{aligned} \dot{\mathbf{x}}\cdot\mathbf{x}' &= 0 \\ \dot{\mathbf{x}}^2 + \mathbf{x}'^2 &= 1 \\ \ddot{\mathbf{x}} - \mathbf{x}'' &= 0. \end{aligned} \tag{5.8}$$

Equations (5.8) imply that:

- the string moves perpendicularly to itself with velocity $\dot{\mathbf{x}}$,
- σ is proportional to the string energy,
- the string acceleration in the string rest frame is inversely proportional to the local string curvature radius.

Thus, a curved string segment tends to straighten itself, resulting into string oscillations. The general solution to the string equation of motion in flat spacetime, Eq. (5.8c), is:

$$\mathbf{x} = \frac{1}{2}\left[\mathbf{a}(\sigma - t) + \mathbf{b}(\sigma + t)\right],$$

where $\mathbf{a}(\sigma - t)$ and $\mathbf{b}(\sigma + t)$ are two continuous arbitrary functions which satisfy

$$\mathbf{a}'^2 = \mathbf{b}'^2 = 1.$$

Thus, σ is the length parameter along the three-dimensional curves $\mathbf{a}(\sigma)$ and $\mathbf{b}(\sigma)$.

5.3 Cosmic strings evolution

As it was mentioned, the expansion of the universe stretches the strings, so that in the absence of energy loss mechanisms, their energy would grow with the scale factor and the string network would eventually become the dominant component of the universes energy density. Observational results are in conflict with this evolution, so such decay mechanisms do exist, being ultimately due to radiation losses and string self-interactions. In particular, closed loops may be formed, and these subsequently oscillate and eventually decay mainly into gravitational radiation.

Provided that the decay rate is high enough, the network will reach a linear scaling solution, where the string density is a constant fraction of the background density and on large scales the network looks the same (in a statistical sense) at all times. Physically, the reason for this is that the number of string interactions increases if the density of strings is high and therefore loop production becomes more efficient and the decay rate increases. Conversely, if the density is too low then there are few interactions and the decay rate is correspondingly lower. Numerical simulations confirm this broad picture, but also reveal that string evolution is a complex non-linear process, involving non-trivial interactions between various different scales.

The cosmic string network can be divided into long (infinite) strings and small loops. The energy density of long strings in the scaling regime is given by (in the radiation era)

$$\rho_L = k\mu t^{-2}$$

where $k = 20 \pm 10$ is a numerical coefficient.

Assuming that the long strings are characterised by a single length scale $\xi(t)$, one gets

$$\xi(t) = \left(\frac{\rho_L}{\mu}\right)^{-1/2} = k^{-1/2}t.$$

Thus, the typical distance between the nearest string segments and the typical curvature radius of the strings are both of the order of ξ. Early numerical simulations have shown that indeed the typical curvature radius of long strings and the characteristic distance between the strings are both comparable to the evolution time t. Clearly, these results agree with the picture of the scale-invariant evolution of the string network and with the one-scale hypothesis.

However, numerical simulations reveal that long strings in the scaling solution are not completely smooth, possessing significant substructure over a wide range of length-scales below ξ. In response to these findings, a three-scale model was developed, [47], which describes the network in terms of three scales, namely the usual energy density scale ξ, a correlation length along the string $\bar{\xi}$, and a scale ζ relating to local structure on the string. The small-scale structure (wiggliness), which offers an explanation for the formation of the small sized loops, is basically developed through intersections of long string segments. According to this model, the small length scale may reach scaling only if one considers the gravitational back reaction effect.

Chapter 6

Possible Signatures of Cosmic Strings

According to the theory, the presence of cosmic strings in the Universe might cause a series of detectable effects:

- gravitational lensing of objects behind a string;
- steplike anisotropies in the cosmic microwave background;
- gravitational waves due to loops oscillations;
- ultra-high energy cosmic rays generation
- black holes formation by massive loops;
- baryon-number violation processes.

In this section we focus our attention on the first two observables, lensing and CMB anisotropies, giving only a brief description of the others.

6.1 Gravitational lensing

The conical nature of space around a cosmic string results in the formation of double images of galaxies or quasars located behind the string. The typical angular separation between the components of a double images being comparable to the conical deficit angle, $\Delta\theta = 8\pi G\mu$.

Gravitational lensing by a string is illustrated in Fig. 6.1. A conical space is obtained after the shaded wedge is discarded and its two boundaries are matched. The observer is represented by two points, O_1 and O_2, on the opposite sides of the wedge. When the observer looks above the string S, the half-space above the line ASO_1 is seen, whereas looking below the string, the half-space below the line BSO_2 is seen. It is clear that all sources located in the wedge ASB have duplicated images. If we consider a point-like source and a string at rest with respect with the observer, the angular separation between the images can be written as

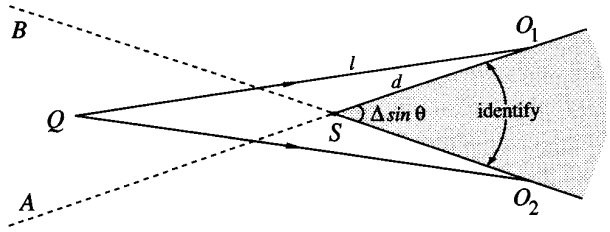

Figure 6.1: *Gravitational lensing by a cosmic string: the observer (O_1 and O_2 are identified), sees two images of the source Q.*

$$\delta\varphi_0 = 8\pi G\mu\ell(d+\ell)^{-1}sin\theta, \tag{6.1}$$

where ℓ and d are the distances from the string to the source and to the observer, respectively, and θ is the angle between the string and the line of sight.

Equation 6.1 can be easily generalized to a moving string, obtaining

$$\delta\varphi = \gamma^{-1}(1-\hat{\mathbf{n}}\cdot\mathbf{v})^{-1}\delta\varphi_0,$$

where $\gamma = (1-v^2)^{-1/2}$, $\hat{\mathbf{n}}$ is a unit vector in the direction from the observer to the source and $\mathbf{v}$ is the velocity of the string with respect with the observer. Depending upon the relative direction of $\mathbf{v}$ and $\hat{\mathbf{n}}$, the angular separation takes values in the range

$$\kappa^{1/2}\delta\varphi_0 < \delta\varphi < \kappa^{-1/2}\delta\varphi_0,$$

where $\kappa = (1-v)/(1+v)$.

It is important to note that if a segment of a rapidly moving string is not perpendicular to the line of sight, then the observer sees more distant parts of the string with a retardation, and the apparent direction of the string differs from its actual direction.

A second aspect of gravitational lensing by a cosmic string is that, at a difference with what happens for compact lenses, the images will be virtually undistorted due to the conical nature of the space time. The only distortions which can arise are sharp edges in the fainter isophotes. Deviations from this idealized pattern can be caused by string curvature, by masses distributed near the line of sight, or by unequal time delays for the two images. In Fig. 6.2 a simulation of a galaxy lensed by a cosmic string is depicted.

From the observational point of view, the most effective way to discover the existence of a non-closed cosmic string is the formation of what we can define as a sort of "milky way" of gravitationally lensed background sources (Fig. 6.3). The photons from a background source move around the string and, by circumnavigating it, they form two images on both sides of the strings itself. Since along the two trajectories the space

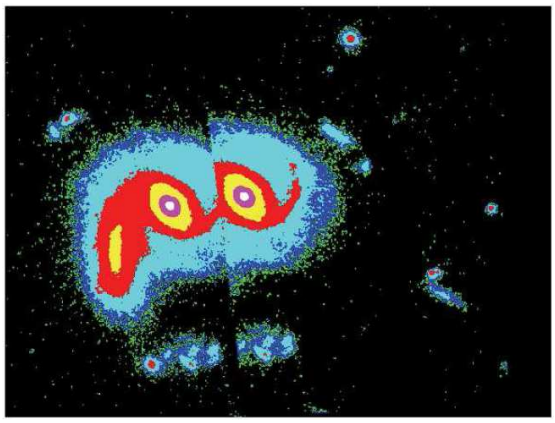

Figure 6.2: *Example of gravitational lensing of a galaxy by a cosmic string*

is flat, there is no gravitational attraction exerted by the string on the photons and no distortion is introduced. However, in spite of the fact that the metric is locally flat, the global properties of the space-time are not Minkowskian but conical.

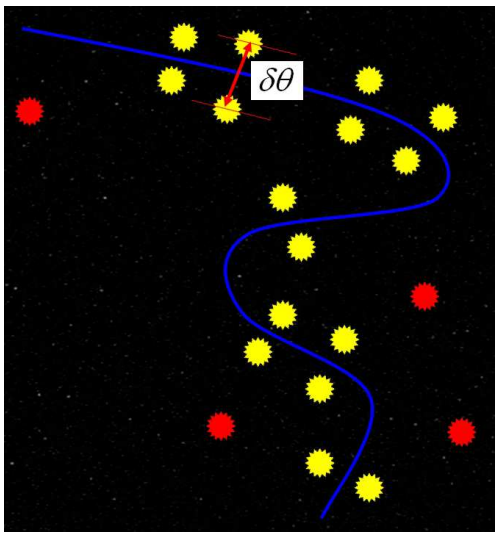

Figure 6.3: *Cosmic string "milky way": a chain of background objects lensed by a cosmic string*

The method of searching for gravitational lensing events makes use of optical observations. Modern optical surveys cover only $1/6$ part of the whole sky and their redshift depth is not more than $z = 2 - 3$, although some optical objects have redshift up to $z = 7$. Therefore, approximately only 3% of the existing strings can be detected with this method (if we suppose that they are distributed in an homogeneous way). Taking into account the predicted number of cosmic strings, it was estimated that gravitational

lensing events are very rare ones: the number of so-called "chains" of gravitational lensed pairs is from 0.3 up to 3 over the whole sky in the most optimistical models. This estimate can explain the unsuccessful previous attempts (see for example the case of the object CSL-1) and shows that additional methods are urgently required because even utilization of ultra deep galaxy surveys is not enough.

6.1.1 The CSL-1 case

The gravitational lensing by cosmic strings can be better understood by taking into account the case of a peculiar object named Capodimonte-Sternberg lens N.1 or CSL-1 located at $RA = 12^h23^m30^s$, $DEC = -12°38'57''$. CSL-1 was discovered in the OACDF [48] by an international collaboration, [12]. CSL-1, is a double extended source laying in a low density field and with the two components separated by ~ 1.9 arcsec. Both components are well resolved (i.e. extended) and have roundish and identical shapes. Low resolution spectroscopy showed that both components are at a redshift of 0.460 ± 0.008, while photometry (both global properties and luminosity profiles) matched those of giant elliptical galaxies at medium redshift. Visual inspection, comparison of main absorption lines, ratio of the spectra of the two components and their cross-correlation, showed that the spectra of the two components, altough in the limited spectral range covered by the original spectra, were identical at a $\sim 99\%$ confidence level. The separation, compatible with the predictable deficit angle for a cosmic string, and the overall appearance of both optical images and spectra arose the suspect that it could be the first case of gravitational lensing by a cosmic string. The other possible explanation, that of a rare chance alignment of two identical giant ellipticals at the same redshift seemed very unlikely due to a series of odd circumstances: the two ellipticals should have been relatively near ≈ 11 kpc to each other, and in spite of this undistorted, with identical (within the errors) spectra, and residing in a relatively low density environment (no other galaxies could be detected in the same region). Even though at the end it was proved that, in spite of all odds, this was the case [10], the detailed study of this anomalous object allowed to investigate in some detail another aspect of the expected observational effects induced by cosmic strings [8, 10, 12, 49].

In fact, as it has already been mentioned above, one of the main characteristics of lensing by a cosmic string is that it does not introduce distortions. In order to try to disentangle between these two possible explanations, extensive simulations were needed, and they proved that the only way to clarify the nature of the object was to obtain high angular resolution images of the object. These simulations showed that lensing of an extended background object by a cosmic strings would introduce sharp edges in the low light level isophotes. In average seeing conditions, these sharp edges are rounded off by the seeing and therefore high resolution data are needed. Fig. 6.4 shows the

simulated sharp edges of a background source. Depending on the impact parameter of source with respect to the string, the cuts are different, they tend to zero in symmetric case.

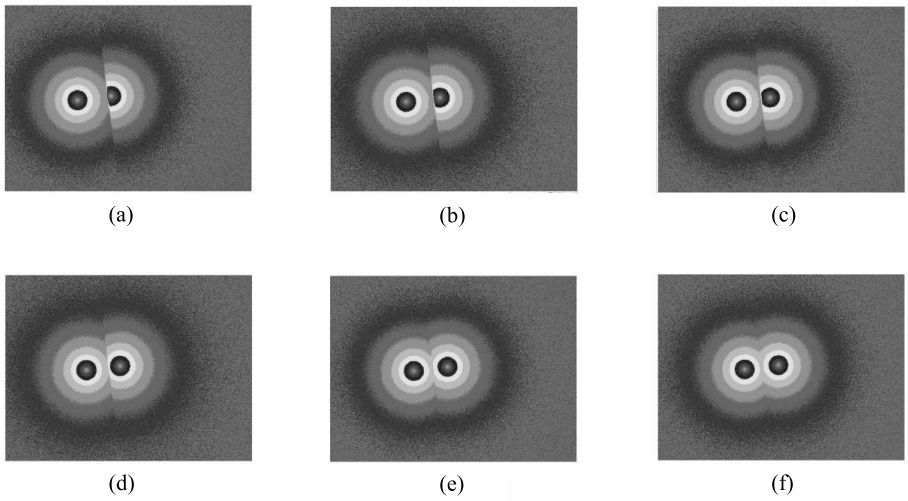

Figure 6.4: *The examples of sharp edges in different position of a background sources relative to the string strips. The CSL-1 case corresponds to the 'e' panel which is almost symmetric.*

In Fig. 6.5 we see the actual image of CSL-1 obtained with the ACS camera on HST. One can compare it with the simulated images of how CSL-1 should have appeared in the case it were a case of lensing by cosmic string. As it can be clearly seen, no sharp edges are present and, what is even more relevant, the shapes of the fainter isophotes are different and seem to indicate some degree of interaction. The most likely interpretation of CSL-1 is therefore that of two elliptical galaxies in an early state of interaction which may eventually lead to a dry merger.

Fig. 6.4 gives an example of what would happen to a circular source lensed by a string: notice that the sharp cut (edge) introduced by the string is clearly visible. The image of extended source produced by a cosmic string is characterized by special features which are unique to cosmic string(for a detailed discussion see [10]). First of all we wish to stress that any extragalactic object can be considered as extended in comparison with cosmic string. In fact, while the strip of cosmic string lensing is defined by its linear density μ, the width of the string itself (its cross section) is of the order of particle scales ($10^{-17} \div 10^{-27}$ cm). The gravitational lensing properties of a cosmic string can be easily understood as it follows: each pixel of the extended source which falls inside the string strip is displayed on the other side of the string. If it falls outside, it will be cut away producing sharp isophoteal edges on the image of the source.

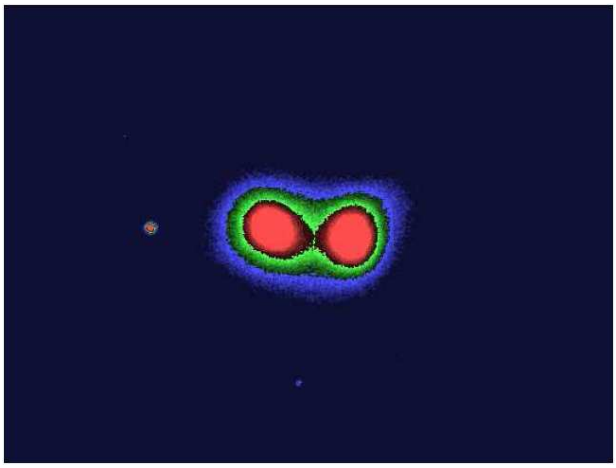

Figure 6.5: *The actual HST image of CSL-1.*

6.2 CMB anisotropies

The peculiar topology of the space-time in presence of a string can cause a detectable effect in the cosmic microwave background, by giving a contribution to its anisotropies. It is known as the Kaiser-Stebbins effect.

Consider two particles moving towards the string along parallel paths with the same velocity **v**. As they pass the string, the particles start moving towards one another and eventually collide. The relative velocity of the particles after they pass the string is

$$\delta u = v\gamma\Delta \tag{6.2}$$

where $\Delta = 8\pi G\mu$ is the deficit angle and v is the projection of string velocity on the line perpendicular to the one joining the source and the observer, in unit of c. The Lorentz factor, $\gamma = (1 - v^2)^{-1/2}$, appears after transforming to the reference frame of one of the particles, and assuming that the line connecting the particles is perpendicular to the string direction.

If one of the objects is a source of radiation and the other is an observer, then the observer will detect a discontinuous change in the frequency of radiation due to the Doppler shift (Fig. 6.6). In a cosmological setting, the string is backlighted by a uniform black-body radiation background, and the Doppler shift results in a discontinuous change of the background temperature across the string [15, 50]. The magnitude of this variation is:

$$\frac{\delta T}{T} = \delta u = 8\pi G\mu v\gamma. \tag{6.3}$$

The total effect is a step-like discontinuity in the CMB temperature distribution as

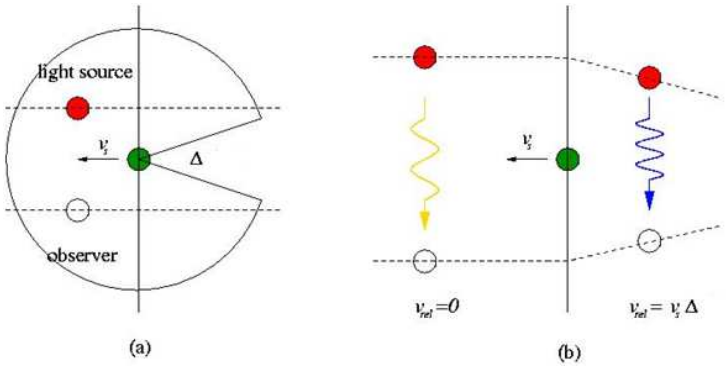

Figure 6.6: *The Kaiser-Stebbins effect is originated from conic space-time around the cosmic string. A moving cosmic string induces relative speed between the light source and observer and causes a Doppler shift of photons.*

depicted in Fig. 6.7: a cold spot right in front of the moving string, a step-like jump in corrispondence of the string and a hot spot immediately after the string.

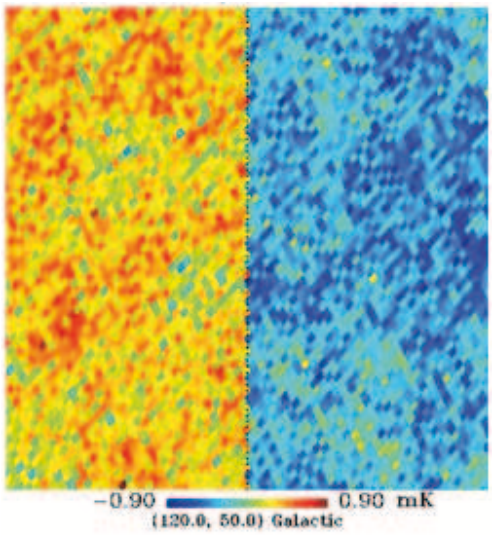

Figure 6.7: *The step-like anisotropy induced by a straight cosmic string.*

The length of the spot depends on how long is the part of the string which is inside the surface of last scattering. Therefore, the minimum length of the spot, which can be in principle observed in optical surveys, must be at least 100 degrees, taking into account the fact that the optical depth cannot be larger than $z = 7$. Taking into account these estimates, we can also understand why all attempts to find a cosmic strings through gravitational lensing effects have so far failed.

It is possible to generalize equation (6.3) for arbitrary angles between the string, its velocity, and the line of sight, [51, 52]. Let $\hat{\mathbf{s}}$ be a unit vector pointing along the string. Since only the transverse motion of any string is observable, one can assume $\mathbf{v} \cdot \hat{\mathbf{s}} = 0$. In the rest frame of the string the observer passes by the string with velocity $\mathbf{v}$. If the observer is at rest with respect to the sources of radiation on one side of the string, then the velocity of the sources on the other side is $\mathbf{v} + \delta u_0$, where $\delta u_0 = 8\pi G\mu \mathbf{v} \times \hat{\mathbf{s}}$. The corresponding velocity difference in the observer's frame is $\delta u = \gamma \delta u_0$. The temperature discontinuity can be found from the Doppler formula $dT/T = \delta u \cdot \hat{\mathbf{n}}$, where $\hat{\mathbf{n}}$ is a unit vector along the line of sight; thus,

$$\frac{\Delta T}{T} = 8\pi G\mu\gamma \hat{\mathbf{n}} \cdot (\mathbf{v} \times \hat{\mathbf{s}}). \tag{6.4}$$

Besides the discontinuous Doppler shift, there are several other effects contributing to the microwave temperature fluctuations. They include:

- temperature, velocity and potential perturbations at the surface of last scattering;
- the Sachs-Wolfe effect from potential perturbations between z_{ls} and us;
- anisotropies from gravitational waves emitted by strings.

Some of these effects may be of magnitude comparable to eq. (6.4), but they do not have a characteristic 'stringy' signature.

6.3 Other observables

6.3.1 Gravitational waves

Gravitational waves emitted by oscillating loops at different epochs produce a stochastic gravitational wave background. To estimate the power emitted in gravitational radiation by a string loop of length L, it is most convenient to use the quadrupole formula

$$\frac{dE}{dt} \sim GM^2L^4f^6$$

The only dimensional parameters available to us are G, μ and L. However, the power loss into gravitational waves is proportional to $G\mu^2$ since the power is the square of the quadrupole moment. Now since the power has dimensions of mass squared, we must have

$$P \sim G\mu^2$$

and the length of the loop drops outside of the estimates. In the cosmic scenario we are interested in the average gravitational energy emitted per unit time by all strings. So we write:

$$\bar{P} = \Gamma G\mu^2$$

where $\Gamma \sim 100$ is a numerical factor. To find the present gravitational wave background amplitude and spectrum one needs to sum over all strings in the network, include appropriate redshift factors etc.

The final result is:

$$\Omega_g(\omega) = \frac{18\pi^2(\beta-1)^2\nu G\mu}{(3-\beta)\sin[(2-\beta)\pi]}\left(\frac{4\pi}{\Gamma\mu\omega t_0}\right)^{(\beta-1)}$$

where ν is a parameter that sets the amplitude for the number density of loops and $4/3 \leq \beta << 2$ is a parameter that characterizes the typical spectrum of gravitational radiation emitted by loops, t_0 is the present epoch. The peak of the spectrum is at

$$\omega_{peak} \sim \frac{4\pi}{\Gamma G\mu t_0}$$

The strongest constraints on the amplitude of the gravitational wave background arise from the timing of the millisecond pulsar. In 1993, the constraint was [53]:

$$\Omega_g < 4 \times 10^{-7} h^{-2}$$

The constraint gets more stringent the longer the millisecond pulsar is observed without encountering noise in its timing. Today the constraint would be slightly stronger than in 1993. In terms of $G\mu$, this gives

$$G\mu < 4 \times 10^{-5} \tag{6.5}$$

The emission of gravitational radiation from strings also contributes to the energy density prior to nucleosynthesis. If the gravitational radiation contribution to the content of the universe exceeds about 5% , it will interfere unacceptably with BBN. This gives another constraint on the parameter $G\mu$ that is slightly better, though comparable to, the one in eq. (6.5).

6.3.2 Cosmic rays generation

An outstanding puzzle in astrophysics is to explain the origin of the so called Ultra High Energy Cosmic Rays or UHECR having energies $\geq 10^{20}\mathrm{eV}$. It has been proposed that evaporation from cosmic string cusps could provide the explanation. When cusps form, the local string velocity will be relativistic. It has been suggested, [54], that interactions

between the overlapping string segments moving at the speed of light will produces energetic particles. The string would emit quanta of the underlying string gauge or scalar fields. Such quanta would be unstable and would in turn decay into quarks and leptons.

The quarks in turn undergo the usual QCD fragmentation process, ending up as jets of hadrons, mostly pions with a few nucleons. Since the decaying particles have masses in excess of $\sim 10^{24}$ eV, and are moving with relativistic speeds, some of the decay products could easily have energies well in excess of 10^{20} eV, and hence be a significant contributor to the cosmic ray background at these energies.

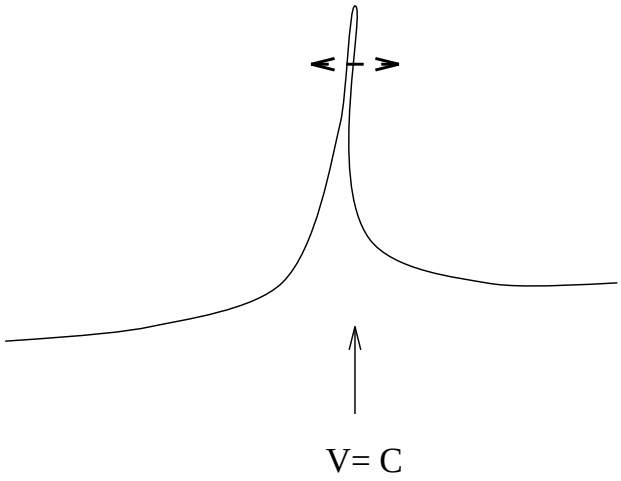

Figure 6.8: *Cosmic ray emission form cusps: Interactions between the overlapping string segments moving at the speed of light will produces energetic particles.*

To estimate how significant such a contribution could be, it is important to have some estimate of the fraction (f_{cr}) of the initial energy of the cosmic string which is evaporated away in this manner. Alternatively we could assume that all the cosmic ray background at this energy is due to cosmic string evaporation and see what value of f_{cr} this would correspond to, which yields an upper bound

$$G\mu f_{cr} \leq 10^{-8}$$

which for GUT strings would imply that $f_{cr} \approx 10^{-2}$ which seems implausible.

6.3.3 Black holes formation

Oscillating string loops are unlikely to collapse to form black holes. The Schwarzschild radius of a loop of invariant length $\ell = M/\mu$ is $r_g = 2G\mu\ell$ and thus, in order to form a black hole, the loop must shrink by a factor of order $(G\mu)^{-1}$ at some time during its

period of oscillation. However, even though the fraction of loops collapsing to black holes may be extremely small, they could be cosmologically significant.

The collapse of a cosmic string loop to within its Schwarzschild radius is a necessary, but not sufficient condition for the loop to form a black hole. There are several possible barriers to the formation of a black hole.

The first is on the total angular momentum allowed by the string. A rotating loops which collapses to form a black hole will produce a rotating black hole. In order that the curvature singularity within the newly formed rotating black hole of mass M lies within the event horizon, the black hole angular momentum $\mathbf{J}_{BH}$ must satisfy the inequality

$$|\mathbf{J}_{BH}| \leq GM^2.$$

Hence, the angular momentum of the loop which collapses must also satisfy this inequality.

The second constrain is related to the radiation emitted by an oscillating loop. As a loop collapses it may radiate a sufficient amount of energy such that its minimum configuration never falls within its Schwarzshild radius. Cosmic strings may emit both gravitational radiation, as seen in 6.3.1, and the quanta composing the string. Emission of non-gravitational radiation by a cosmic string is suppressed relative to the emission of gravitational radiation unless the curvature along the string become smaller than the loop thickness, λ, given by the Compton wavelength of the quanta composing the string. When that happens, the string is no longer topologically bound and the loop may rapidly "unwind" and vanish in a burst of radiated quanta. Thus, in order that a loop may collapse to form a black hole, it is required that its thickness is much smaller than the Schwarzschild radius

$$\lambda \ll R_S = 2GM.$$

6.3.4 Baryon asymmetry

For grand unified strings, the heavy gauge field trapped in the string core can have baryon-number-violating couplings. Light fermions scattering off the string S, therefore, can change their baryon number. For example,

$$Q + S \longrightarrow \ell + S, \tag{6.6}$$

where Q is a quark and ℓ is a lepton. Baryon-number-violating processes can also be mediated by a scalar field φ which has a Yukawa coupling to quarks and leptons, for example,

$$\varphi \bar{Q} \ell + \varphi^\dagger \bar{\ell} Q. \tag{6.7}$$

If such a field develops a condensate in the string core, it can cause baryon-number-violating scattering of the form (6.6). These processes can result in the generation of a net baryon number in a baryon-symmetric universe, or else they can erase baryon number generated at earlier times.

It can be shown [55, 56], that the baryon number B must vanish if B-violating interactions are in thermal equilibrium. Essentially, the reason is that, in the absence of a conservation law, B is determined by minimizing the thermodynamic potential. This leads to a vanishing chemical potential for baryons and thus to $B = 0$. B-violating scatterings of the form (6.7) provide a channel through which baryons and leptons can equilibrate and erase their primordial abundances.

Baryon asymmetry can also be generated at the final stages of loop decay. When a loop shrinks to a size comparable to its thickness, it disintegrates into heavy particles which can then undergo B- and CP-violating decays. The calculated baryon asymmetry may be comparable to that observed. The largest contribution to the baryon number of the universe again results from the earliest times, when the strings are overdamped.

Chapter 7

Photometric Redshift

As previously mentioned, the presence of cosmic strings induces some detectable effects and the availabily of huge amounts of data produced by both optical and radio surveys, gives us the possibility to explore two different aspects of such problem. The method of searching for gravitational lensing events is based on optical observations. Modern optical surveys cover only $1/6$ part of the whole sky and their redshift depth is not more than $z = 2 - 3$, although some optical objects have redshift up to $z = 7$. It is possible to estimate the number of strings sufficiently near to be detected. Consider the standard cosmological ΛCDM model with the FRW metric and an emitting object. The scale factor $a(t)$ of the metric is determined by the Friedmann equation (2.9). We also choose the WMAP recommended global cosmological parameters: $H_0 = 72$ km/s/Mpc is the present value of the Hubble parameter, $a(t_0) = a_0 = 1$ is the present value of the scale factor, Ω_Λ refers to the cosmological constant. The values used in the following are $\Omega_m = 0.27$, $\Omega_\Lambda = 0.73$.

Taking into account the usual determination of the distance of an object in the expanding Universe:

$$l = c \int_{t_e}^{t_0} \frac{dt}{a(t)},$$

where t_e is epoch when the photons were emitted, t_o is the present epoch, and by substituting $t_e = 0$, one obtains the distance to the particle horizon as

$$l_{ph} = 3.4 \frac{c}{H_0}$$

in standard ΛCDM model.

One can also redefine l in terms of the red shift instead than in terms of time. In this redifinition the equation for the distance becomes

$$l(z) = \frac{c}{H_0} \int_0^z \frac{dz}{1+z} \frac{1}{\sqrt{\Omega_m (1+z)^3 + \Omega_\Lambda}}.$$

This form of a cosmological distance is more convenient to perform a probabilistic analysis.

The distance betwen an observer and a cosmic object is a function of the redshift of the object and of the cosmological parameters. In order to estimate the probability to observe a string we suppose that the most distant object we are able to observe is at $z = 7$. In this case we can calculate the radius of the sphere in which all avaible optical objects are

$$l_7 = 0.64 l_{ph}$$

Let us now assume that there is a straight string inside the particle horizon sphere, then the probability that the string is inside the optical radius is proportional to the optical sphere volume

$$p = l_7^3 = 0.25$$

where l_7 is the radius of this sphere in units of the distance to the particle horizon. Therefore only one string out of four is inside the sphere of optical sources. A detailed calculation of the probability to find a string and of the number of expected lenses can be found in [8, 11, 57]. In this case the string just "touches" the sphere of optical sources and the angular size of the string turns out to be $\sim 100^\circ$. If the redshift of optical source sphere is closer, then the size of a straight string has to be much larger.

In the case $z = 2$ the sphere radius is

$$l_2 = 0.38 l_{ph},$$

and the probability is $p = 0.05$. In this case, only one string out of twenty is inside the sphere and the angular size of the string is around $\sim 134^\circ$. The angular size of straight string is very important since it defines the scale of the signatures left in the radiomaps. As a rough estimate, in order to observe the gravitational lensing effects by a cosmic string, the number of strings must be larger than 4 in the observable Universe. In order to derive the detection probability one must derive first the number of string inside the particle horizon which is model dependent. If we restrict ourselves to long strings alone we can use the value derived in [58] ($10^3 \div 10^4$). By using such figures we derive that at least 50 strings should be closer than $z < 2$ and astronomers should be able to detect at least a dozen of "new milky ways".

The stumbling block of this kind of research is due to the presence of spurious effects, mainly when the flux is low. In fact, the "milky ways" of lensed objects need to be searched in the catalogues extracted from extensive multi-band surveys. In this catalogues, the selection of the candidate pairs of lensed images is performed by searching for all pairs of objects having identical (within an arbitrarily chosen confidence interval) flux ratios in all observed bands. At low flux levels (and this is the case for distant background galaxies) photometric errors become larger and deeply affect the resulting

lists of candidates. If the confidence interval is kept too large, it will result in a huge and unmanageable increase in the number of candidates while, if the interval is kept too small most objects will be rejected making it almost impossible to detect the pairs of lensed images. This can be easily proved by applying cuts in the color space to the objects contained in the SDSS catalogues.

To improve the contrast in order to reduce the number of spurious detections, a possible approach is to improve the contrast by taking into account not only the photometric parameters alone but also the spatial distribution of the background galaxies.

To this purpose, we made use of an innovative method for the determination of photometric redshifts of galaxies and QSOs. The method is based on multiwavelength photometry and on a combination of data mining techniques and makes use of specific tools developed under the EuroVO and NVO frameworks for data gathering, preprocessing and mining, while relying on the scaling capabilities of the computing grid. This method, described in the following, allowed us to obtain photometric redshifts with an increased accuracy (up to 30%) with respect to the literature. It needs to be stressed that the application of these redshifts to the production of a list of candidate pairs in the SDSS is still in progress.

7.1 The reshifts and the Hubble law

In 1929 the american astronomer Edwin P. Hubble, using data collected over the previous decade by M. Humason, S. Slipher and himself, reached the definitive proof of a disconcerting result found a few years before by the swedish astronomer Knut Lundmark: galaxies receed from the observer at a velocity (easily measured through the Doppler effect on spectral emission lines) which, at least in the near universe, is linearly proportional to their distance. The phenomenon, which came to be known as the Hubble law[1], can be written (in the classical approximation) as

$$v = H_0 d$$

When a source of radiation moves toward or away from an observer, the observed frequencies of photons are different from their emission values. Quantitatively, if v_r is the radial velocity of a source that emits photons that have frequency ν_0 in the rest frame of the source, then these photons will be detected at frequency:

$$\nu = (1 - \beta)\gamma\nu_0$$

where

$$\beta^2 = \frac{v^2}{c^2}$$

[1]The fact that it was actually discovered by Lundmark has been sistematically neglected.

and

$$\gamma = \frac{1}{\sqrt{1-\beta^2}}$$

and c the speed of light. To the lowest order in $\frac{v}{c}$, $\gamma = 1$ and the frequency shift is:

$$\Delta\nu \equiv \nu - \nu_0 = -\beta\nu_0$$

In terms of wavelengths $\lambda = \frac{c}{\nu}$, it is necessary to this order in $\frac{v}{c}$ that $\frac{\Delta\lambda}{\lambda_0} = -\frac{\Delta\nu}{\nu_0}$ as

$$\Delta\lambda = \frac{v_r}{c}\lambda_0$$

Thus $\Delta\lambda$ for a receding source is positive, and the observed spectrum is redshifted relative to its rest wavelength; on the other hand, for an approaching source, $\Delta\lambda$ is negative and the observed spectrum is blue-shifted. In general, the redshift of an object is defined to be

$$z \equiv \frac{\Delta\lambda}{\lambda_0}$$

Theorists almost immediately realized that the Hubble law could be easily explained in the framework of general relativity and, in particular, in the Lemaitre model of an expanding universe. In this model photons propagating through the expanding space are stretched and give rise to the cosmological redshift. This cosmological effect differs from the simple Doppler effect because the velocity boost (i.e. the Lorentz transformation) between the source and the observer is not due to classical momentum and energy transfer, but the photons emitted by the receding source increase their wavelength as the space-time expands. This effect is prescribed by the current cosmological model as an observable manifestation of the time-dependent cosmic scale factor a in the following way:

$$1 + z = \frac{a_0}{a_t}$$

where a_t is the scale factor measured at time t before present time, while a_0 is the current value of the same scale factor. This type of redshift is called cosmological redshift or Hubble redshift. It needs to be stressed that, according to the cosmological interpretation of redshift, the galaxy located at redshift z is not receding simply by means of a physical velocity in the direction away from the observer; instead, the intervening space between the observer and the emitting galaxy is stretching, so accounting for the large-scale isotropy of the effect demanded by the cosmological principle.

For redshifts $z < 0.1$, the effects of space-time expansion are minimal and the observed redshifts are dominated by the peculiar motions of the galaxies relative to one another that cause additional Doppler redshifts and even blue shifts, while at higher redshifts the cosmological component is almost always dominant with respect to the proper motion component. From a mathematical viewpoint, the statements "distant

galaxies are receding" and "the space between galaxies is expanding" are related by a change of coordinate systems. Expressing this change in a correct mathematical framework requires working with the formalism of the Friedmann-Robertson-Walker metric in the theory of the general relativity.

For a long time, one of the key problem of observational cosmology was the derivation of an accurate and reliable estimate of the parameter H_0, also known as the Hubble constant. Conceptually speaking this should be an easy task since all would be needed are the accurate distances for a small number of galaxies and their recession velocity. The ratio of these two quantities would then allow an accurate estimate of H_0. In practice, however, due to the systematics, to measurement errors and to the presence of concurring and often strongly entangled effects, the task proved to be a true nightmare which has been clarified only recently, when measurements made with the Hubble Space Telescope have allowed to obtain an accurate estimate: $H_0 = 70 \pm 8 kms^{-1} Mpc^{-1}$. Once H_0 is known, at least in principle, the measure of the distance for large samples of galaxies becomes trivial though time consuming task. As already mentioned, from the operational point of view the *redshift* of a source is measured through the shift of its emission/absorption spectral lines with respect to their laboratory frequency.

At faint light levels spectral lines are usually poorly defined and measurements are affected by poor S/N ratios, or by instrument systematics. Taking spectra of such faint objects is a demanding task in terms of observing time: for a given object the dilution of the signal in the wavelength domain implies about two orders of magnitude increase in observing time with respect to normal photometry in order to achieve the same S/N. Furthermore, taking into account all effects, it is safe to state that, for a specific observing apparatus, the faintest galaxies for which accurate spectroscopic redshifts may be estimated, are at least two-three magnitudes brighter than the faintest objects detectable photometrically.

Now, given that the number counts (number of galaxies per bin of magnitude and per square degree) increase more or less exponentially for decreasing luminosities, it is clear that the spectroscopically accessible universe is much brighter (and hence smaller) than the photometric one.
Even the modern MOS (Multiple Objects Spectrographs) which can take up to several hundreds spectra in a single exposure, cannot satisfy the crave for data of modern cosmology and alternative methods need to be found. These methods arise from an obvious but often overlooked consequence of the Hubble law: the appearance and the properties of galaxies at different redhifts, when observed in a given photometric band, correspond to different rest-frame wavelengths. In other words, if we want to compare the properties of a nearby galaxy observed in the visible band with the properties of a galaxy located at high redshift, we need to observe it at longer wavelengths (i.e. near IR, far IR, etc.): the higher the redshift, the larger the wavelength shift. This simple

consideration is the starting point of the so called *Photometric Redshifts* technique which shall be discussed in the following.

The main idea behind it can be simply explained as it follows. Let us suppose to have the same galaxy moving far away from an observer who is performing multiband photometry. While it moves, the continuum and line features in the galaxy spectrum shift in wavelength and move from one photometric band to the other, thus affecting the integrated colours of the galaxy. In principle, the procedure can be inverted and colours can be used to derive an accurate estimate of the redshift of the galaxy. Obviously, the information richness of spectra cannot be supplied by a coarse integration of the spectra themselves over a few broad band filters, so it is quite clear that photometric redshifts cannot reach the spectroscopic redshifts accuracy.

As always, things are much more complex than what one would expect and the all photometric redshifts methods need to cope with a wide variety of effects: from the fact that different galaxy types have different spectra, to the presence of evolutionary effects, to degeneracies existing among the observed properties of galaxies of different morphological types.

7.2 The Data

7.2.1 The Sloan Digital Sky Survey

The SDSS is a digital imaging and spectroscopic survey of the high Galactic latitude sky in the Northen Hemisphere, covering $\sim 10,000$ sq. deg. mainly in the Northern hemisphere in five specifically designed bands (u, g, r, i, z) [59] and is complemented by an extensive redshift survey for about 10^6 objects (mainly galaxies and QSO's). The SDSS data are made available to the community through a public archive which at the moment is distributing its Seventh Data Release [60].

However, most of this work was performed on the Sixth Data Release (hereafter DR6, [61]). This is due to different reasons: first of all, DR6 was the most recent data release available when our work began. Also, since we are interested in a multiwavelength approach to the photometric redshift estimation task, we took advantage of the existing crossmatched tables for the GALEX Ultra-Violet survey and the DR6 objects (see [62])

7.2.2 The Galaxy Evolution Explorer

GALEX is a NASA mission led by the California Institute of Technology. Its aim is to investigate evolution in the star formation from the early universe up to the present.

GALEX is an orbiting telescope which observes the universe in two bands: Far Ultraviolet (FUV, ~ 154 nm) and Near Ultraviolet (NUV, $\sim 232nm$).

For this work we used the GALEX release 3 (hereafter GR3) and in particular we queried for objects crossmatched with the SDSS DR6. The crossmatching procedure is discussed in some detail in [62].

7.2.3 The base of knowledge

The first base of knowledge (hereafter BoK) consists of a set of spectroscopically confirmed QSOs from the SDSS survey, with i-band magnitudes ranging from 14.5 and (de-reddened) 21.3. Although we are going to use the most robust photometric measurements available in the SDSS, namely the point spread function magnitudes (*psfMag*), we extracted from the database all the photometric measurements available, i.e. *fiberMag*, *modelMag*, *petroMag*, as well as the corrections for galactic extinction.

The lower limit is not corrected for reddening since its sole scope is to avoid saturated objects, while the 21.3 limit is the limiting apparent magnitude.

More specifically, we queried the `photoObjAll` table of the SDSS CAS interface for the magnitudes (and their errors) of the quasars (`specClass` either 3 or 4) for which a spectroscopic observation is available, i.e. the correspondent object in the `specObj` table.

We restricted our query to the primary observations (`mode`=1) and ask for the spectroscopic redshift z_{spec} with a consistent value (`zClass` > 2), high confidence (`zConf` > 0.85) and without warning flags (`zWarning`=0).

The SDSS photometric system does not allow the detection of quasars with $z > 6$ and, with the additional constraint of having the objects detected in at least two bands, this limit reduces to $z \sim 5.8$ [63, 64]. At the low-redshift end, the design of the u filter and the location of the gap between the u and g filters were chosen to emphasize the difference between objects with power-law spectral energy distributions (SEDs), such as quasars at $z < 2.2$, and objects that are strongly affected by the Balmer decrement, particularly A stars, which are historically the prime contaminants in multicolour optical surveys for low-redshift quasars.

To test our method on a galaxy sample we used the same BoK as in [65], i.e. galaxies with $z < 0.5$, dereddened r magnitude $r < 21$, and $mode = 1$ (deblended sources).

7.2.4 Feature selection

Feature selection plays a key role in data mining. We shall not go deep in detail on thip topic. For what concerns our specific problem we can refer to the feature selection

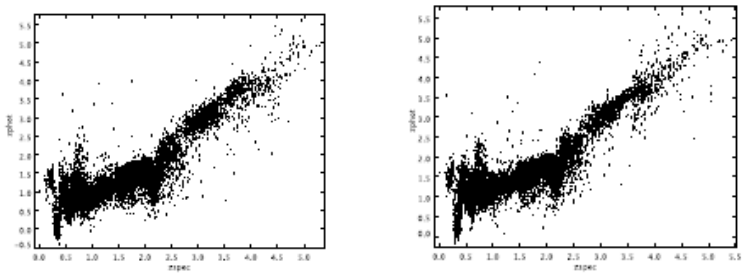

Figure 7.1: z_{phot} *vs* z_{spec} *for two single MLP networks with 15 hidden neurons, taken from the five networks in Tab. 7.1 (Net 1 and 2). This plot contains 13078 points from the test sets, i.e. the dataset used for testing the generalisation capability of the networks. It is clearly shown that due to the not deterministic nature of MLP training process the results may differ from one training to another. The network architectures are described in Tab. 7.1*

performed by [65] to the SDSS galaxies sample, since the very same arguments stand for quasars.

Throughout this chapter we will assume that the input features are the four *natural* optical colours of the SDSS photometric system, namely *u-g*, *g-r*, *r-i*, *i-z*. The target is, obviously, the spectroscopic redshift.

Then, in order to produce a robust data mining method for photometric redshift estimation that is capable of using as much information as possible for the photometric estimation, we will expand the parameter space including ultraviolet observations from GALEX, and thus two other features will be presented to the networks: *z-nuv* and *nuv-fuv*.

For the final experiments reported in section 7.7 we will introduce other four input features, i.e. the four optical colours errors.

7.3 The simplest solution: a single Neural Network

Artificial neural networks are effective tools for addressing regression problems. We can thus use a single Multi Layer Perceptron (MLP) to try and tackle our problem in the simplest way.

In Fig. 7.1 it is shown the test scatter plot for two MLPs with the topology shown in Tab. 7.1. The networks are trained on a different training set, validated by means of a different validation set, but the test set is the same. Also, the initial weights are randomly chosen for both the networks, so the initial weights can be assumed to be different as well.

The scatter plots in Fig. 7.1 show some catastrofic regions where the networks badly

fail to estimate the redshift. These regions and the possible origins of the bad performance shown by the networks in there will be subject to deep analysis in section 7.6.1.

It is clearly visible that the two training processes lead to different results. This is due to some noise sources described in appendix A.1.5 and to some degeneracies related to the optical SDSS input space.

	Net 1	**Net 2**	**Net 3**	**Net 4**	**Net 5**
Input nodes			4		
Hidden nodes			15		
Output nodes			1		
Learning Rate			0.1		
Hidden Act. Function			Elliot (sigmoid)		
Output Act. Function			Linear		
Test Error	0.057	0.055	0.057	0.055	0.058
$\overline{\mathbf{\Delta z}} = \overline{\mathbf{z_{spec} - z_{phot}}}$	0.028	−0.041	0.059	0.004	−0.079
MSE	0.397	0.391	0.394	0.0391	0.0394

Table 7.1: *Network architecture for five single ANNs (see Fig. 7.1). For each network the average and standard deviation of the distribution of the residuals $\Delta z = z_{spec} - z_{phot}$ are shown. Training and test errors are in normalized units. Notice that Δz may follow a Gaussian distribution globally but not locally, so the standard deviation is not related to any confidence interval useful for a robust estimation of the error.*

In order to avoid overfitting, and to seek the trade-off between variance (from the training) and bias (from the training) for the individual networks we make use of an early-stopping validation procedure. However, new variance/bias is introduced in the splitting procedure.

To take into account this fact we could perform a k-fold cross validation. However, cross validation is a somehow empiric procedure, very effective when dealing with data that show a good regularity, but it lacks a consistent statistical framework and is inadequate when dealing with *pathologic* data like the QSO optical sample from the SDSS.

So far, we have spotted different problems that arise when dealing with neural networks regression predictions and the physical nature of the QSO SDSS sample:

- Bias/Variance from both data and training for the neural networks,
- Input noise,
- Target noise,
- Cross validation inadequacy for our data,
- Degeneracies.

7.4 Ensemble of Networks

In the last decade a lot of interest there has developed in a new class of predictors, namely *ensemble* networks. Each ensemble is composed of several networks individually trained and whose outputs are combined by means of a *gating* network in order to produce the ensemble output.

The combination is performed by simple averaging, or by a linear combination of the single outputs.

To understand how ensembles work, we may recall the neural network learing procedure formalism described in appendix A.1.4. We have a training set made of patterns sampled from an unknown functional relationship:

$$y_p = g(\mathbf{x_p}) + \epsilon \qquad ,$$

where g is the regression function and ϵ is a zero mean additive noise with finite variance σ^2. The learning process seek out the minimum of the MSE cost function

$$E_f = \sum_{p=1}^{N} (y_p - f(\mathbf{x_p}))^2 \qquad ,$$

where f is the network output given the pth pattern.

Now, this cost function can be restated in terms of bias and variance:

$$E_f = E\{\text{Var}_f + \text{Bias}_f^2\} + \sigma^2 \qquad ,$$

where E is the expectation operator, $\text{Var}_f = E\{(f(\mathbf{x}) - E\{f(\mathbf{x})\})^2\}$ is the variance and $\text{Bias}_f = E\{f(\mathbf{x})\} - g(\mathbf{x})$ is the bias.

A *simple* ensemble is a set of M networks whose outputs are combined by a simple average:

$$f_{ens}(\mathbf{x}) = \frac{1}{M} \sum_{i=1}^{M} f_i(\mathbf{x}) \qquad ,$$

We will define a *general* ensemble one for which the output is defined by

$$f_{ens}(\mathbf{x}) = \sum_{i=1}^{M} \alpha_i f_i(\mathbf{x}) \qquad ,$$

For a general ensemble, once all the experts have been trained the problem is to find the values of the α_i parameters. Much work has been made to understand why an ensemble perform better than a singe network and how to take the best advantage of

it. In [66] it is shown that the MSE is guaranteed to be less than the average MSE of the individual predictors:

$$(f_{ens} - d)^2 = \sum_i \alpha_i (f_i - d)^2 - \sum_i \alpha_i (f_i - f_{ens})^2$$

The second term is called *ambiguity* and is always positive, thus the MSE of the ensemble is always better than the weighted average of the individual error.

This approach is useful to increase the accuracy of the prediction, but doesn't increase the generalization error. In [67] a different decomposition for a simple ensemble is derived:

$$E_{ens} = E\left\{\frac{1}{M}\text{Var} + \left(1 - \frac{1}{M}\right)\text{Cov} + \text{Bias}^2\right\} + \sigma^2 \qquad .$$

It is possible to defines *decorrelation* networks by using this formula [68]: by introducing decorrelation in the different networks training processes, via the addition of a time dependent penalty term in the cost function[2], the overall prediction accuracy and generalization error may be significantly improved.

However, we have to deal with another factor. Notice that the problem we have faced so far assumes that there is a single mapping function from the parameter space to the target space of spectroscopic redshifts[3] and, above all, that there is one noise regime throughout the parameter space. This is not true, actually, for our data.

Degeneracies are an example of how the noise regime changes in different colours intervals. Also, we know that the input and target noise depend on the magnitude of the objects, and so depend on their distance from the observer, which is the information encoded in the redshift itself. Since the sources' colours distribution depend on the distance, we know for sure that the noise depends on the input as well. Finally, the sparseness of the QSO BoK itself changes with the colour.

Now, trying to learn the mapping function on different input space regions with different noise levels and different densities by a single network is a mismatch since the network could extract features that do not generalize well in some regions (local overfitting), whilst it doesn't learn all it potentially could in another region (local underfitting). In other terms, since the cost function is unique for a single network, a local overfitting in some region may be compensated by a local underfitting in other regions.

[2]This procedure is similar to the weights regularization procedure shown in [69]: in order to achieve good generalization performance, one can introduce a regularization term into the cost function in order to prevent weights to become overly large. This procedure is usually performed by cross-validation.

[3]Although a single global model can in principle approximate any function, even if it is piecewise defined, in real world problems it is actually very hard to extract such a global model from the data. In these cases the error function is very complex and it is likely for the backpropagation process to end in a local minimum.

The key process in the general ensemble networks is *promoting diversity*. Since the ensemble efficiency is related to the covariance term among the different networks, one can manage this covariance by promoting diversity in the different training sets. The first method to be used for promoting diversity were bagging and boosting. However, these methods are more suited for classification tasks and, on the other hand, rely on the probabilistic sampling of the data sets.

For all these reasons we turned our attention to a special class of ensembles, i.e. the so called *gated experts*.

7.5 Gated Experts

The basic idea of *experts* is to try and learn several local models from the data, in different regions of the parameter space. These experts are specialized over their subdomain and their outputs are linearly combined to form the output. The first proposed models that implement this idea are referred to as *Mixtures of experts*.

Gated experts are somehow different, in that they *nonlinearly* combine *nonlinear* experts. The input space is also nonlinearly split into subspaces. The gating network is trained to learn both the segmantation of the input space and the input dependent coefficients $g_i(\mathbf{x})$ that combine the system outputs $y_i(\mathbf{x})$,

$$y = \sum_{i=1}^{K} g_i(\mathbf{x}) y_i(\mathbf{x}) \qquad .$$

Each expert i is a standard neural network that learns a function $y_i(\mathbf{x})$ by means of a sigmoidal activation function hidden layer and a linear activation function output layer, as depicted in appendix A.1.4.

The gating network, instead, has a classification flavour, with the K output layer's nodes having a *softmax* activation function

$$g_j = \frac{e^{s_i}}{\sum_{i=1}^{K} e^{s_i}} \qquad ,$$

$s_i(\mathbf{x})$ being the output of the hidden layer's nodes. The outputs of the gating networks are normalized to 1 and their value express the *competition* among different experts, which is soft, in the sense that each input pattern has a non zero probability of being in the domain of each expert.

This problem cannot be addressed by means of supervised learning only since, in general, we don't have any *a priori* knowledge on how to carve the input space. Thus, a complex cost function has to be derived to take into account all the variables. In [70] it is

shown how this cost function may be derived. However, in the same paper it is clearly shown that:

- The cost function cannot be minimized with gradient descent, but the problem can be reformulated and addressed by means of an *Expectation Maximization* algorithm.
- In order to find a consistent solution we need to assume that *one and only one expert is responsible for each pattern*. In other terms, we need to be sure that there is a way of isolating different *sub-processec* throughout the parameter space. For the QSO sample we are dealing with, this assumption is false.

7.6 Weak Gated Experts

We have explored some of the solution that seemed to fit our problem, but since our problem is, from a physical point of view, ill-defined due to heavy degeneracies, there are some implications which need to be taken into account.

The best approach, however, seems to involve the gated experts. We have elaborated a new method that can be viewed as a "weak" version of the gated experts we have introduced before and that, while trying to take advantage of the gated experts strengths, will also take into account our knowledge of the problem from a physical point of view.

7.6.1 Clustering

The gated experts demand an unsupervised approach to the carving of the input space. We know that the colours distribution changes noticeably with the redshift, so that we can spot regions of the parameter space in which the colour redshift relationship changes its regime.

The figure 7.2 shows the projection of the SDSS QSO sample on the $u-g, g-r$ plane. The grey scale stands for the source's spectroscopic redshift. We can clearly spot two main regions: a compact *window* where most of the objects lie, with the redshift ranging from $z_{spec} = [0, \sim 2.5]$, and a vast region where the data is more sparse and the redshift is high.

Zooming inside the windows we can see how the degeneracies arise. Although this plot refers to a bi-dimensional projection of a 4-dimentional space (where it is possible that some of the degeneracies are resolved), this region is characterized by sources with similar colours and very different redshifts.

This fact suggests that we can carve the input space into different regions, two or more inside the *window* and one or more outside. We don't know if the mapping function changes between these sub-domains, but we know for sure that error and noise

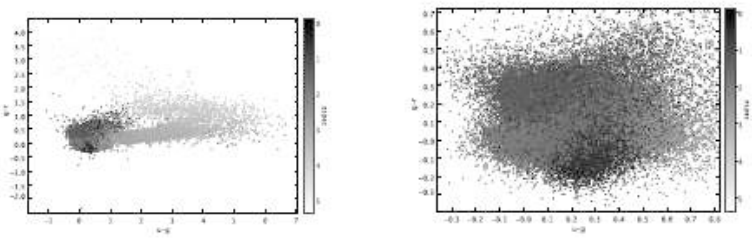

Figure 7.2: *Colour distribution projection on the $u-g, g-r$ plane of the SDSS QSO sample. The grey scale indicates the redshift. In the right panel a zoom on the region of larger density is shown.*

regimes are different in these regions and, in particular, that some of them (the densest ones) are heavily affected by degeneracies while the others are affected by sparseness.

To partition the input space we decided to make use of a *fuzzy* version of a simple clustering algorithm, namely the fuzzy k-means, or c-means.

The classical *crispy* k-means algorithm finds, given the number of clusters k and a metric, the centroids that minimize the distance with the objects belonging to their clusters and maximize the distance among them, by an iterative method. When convergence is reached, each point in the input space will belong to one and only one cluster. c-means works exactly like its crispy counterpart for finding cluster centroids, except that in this case each source has a non null *membership degree* to each cluster. This property allows us to build clusters with *soft* boundaries, introducing some redundancy in the datasets, because we allow the patterns to belong to different clusters.

Generally speaking, when using machine learning techniques, the BoK must be used carefully: when we train a neural network we have to make sure that the input features will all be available for the redshift prediction. For example, we can't train a neural network with the spectroscopic redshift as a feature, since, quite obviously, we won't have this information at our disposal during the photometric redshift calculation. This concept is quite trivial. However, when performing a clustering we could, in principle, make use of additional information from the BoK, even if this information won't be available at "runtime": we will show in this section that, for our weak gated experts, this is actually a useful approach. In other terms, we can use the spectroscopic redshift to cluster our BoK patterns and then remove this information from the input features we use to train the neural networks. We will shortly show how this is possible.

Figures 7.3 and 7.4 show the clusters found by a standard crispy k-means. The number of clusters may be two or three. For the clustering in figure 7.3 only colours are taken into account, while in the clustering represented by figure 7.4 z_{spec} is used as well.

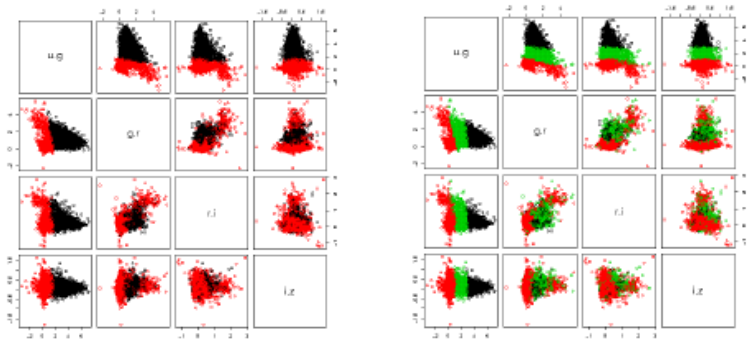

Figure 7.3: *Clusters found by a k-means algorithm: (a) 2 clusters; (b) 3 clusters. The pictures show all the projections on the colour/colour planes. The clustering is based on the colour information only. In figure 7.4 the same algorithm is used to take into account* a priori *knowledge, i.e. the spectroscopic redshift.*

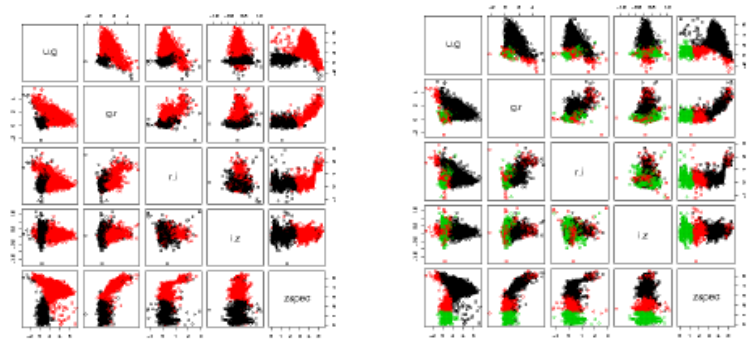

Figure 7.4: *Clusters found by a k-means algorithm: (a) 2 clusters; (b) 3 clusters. The pictures show all the projections on the colour/colour planes and on the colour/z_{spec} plane. Unlike figure 7.3, the clustering is not based on the colour information only, but we take into account* a priori *knowledge, i.e. the spectroscopic redshift.*

7.6.2 Using z_{spec} for clustering

The main source of degeneracies affects those quasars that have similar colours but very different redshifts: thus, by clustering BoK quasars on the base of their colours *and* redshifts, we can help different experts to train themselves on a more homogeneous sample. In other words, although there is no way we can remove degeneracies, we can always try to increase the expertise of the networks in the ill-behaving regions of the parameter space, entrustring the gating newtork with the recognition of specific patterns in the experts predictions.

Dataset	Objects	Subset	σ_r	Δ_{T_1}	Δ_{T_2}	Δ_{T_3}
S	QSO	O	0.154	48.7%	70.3%	78.9%
SG	QSO	ONF	0.089	67.9%	85.4%	91.0%
SG	QSO	ON	0.104	62.9%	83.6%	90.0%
S	GAL	O	0.019	40.6%	68.6%	83.9%

Table 7.2: *This table summarizes our results with some figures we find meaningful. Dataset: "S" stands for SDSS (optical) colours, "G" stands for GALEX (UV) colours. Subset: "O" stands for optical colours, "N" for near UV and "F" for far UV. σ_r is the median absolute deviation (mad), a robust estimate of the residuals variability. We do not find the standard deviation as meaningful as mad, since it is very sensitive to outliers, and therefore unfit to represent QSO residuals. For each dataset three Δ_T are measured: they denote the number of objects whose absolute deviation $|z_{spec} - z_{phot}| < T$. QSO's: $T_1 = 0.1$, $T_2 = 0.2$, $T_3 = 0.3$. For galaxies: $T_1 = 0.01$, $T_2 = 0.02$, $T_3 = 0.03$.*

7.6.3 Gating Network

The gated experts must be combined by means of a non-linear superposition: this task should be performed by a Maximization Expectation procedure together with the carving of the input space. Our "weak" gating network emulates the standard gating network by means of an MLP network in a regression configuration: this time, the features will be the colours *and* the experts' outputs. This means that according to the photometric colours of the source, the gating network will try and learn how to recognize the patterns in the redhift estimations of the indivual experts and assign to each source the best estimate of the photometric redshift.

We cannot forget that the gating network is a neural network itself, and it suffers by all the noise sources we have introduced so far. We use validation for finding a good bias/variance trade-off and a simple ensemble to increase accuracy.

7.7 Results

7.7.1 SDSS optical colours

We can measure our method effectiveness, namely accuracy and generalization, by means of the test set: figure 7.5 shows the z_{phot} vs z_{spec} scatter plot for the output of a single MLP network (left panel) and of the weak gated experts method. Both plots refer to the QSO sample from SDSS, i.e. optical colours (and errors) only. It is evident, even at first sight, that the photometric redshift reconstruction of our method significantly outperforms the single MLP network.

Notice that in these experiments we did not use just colours as input features, but

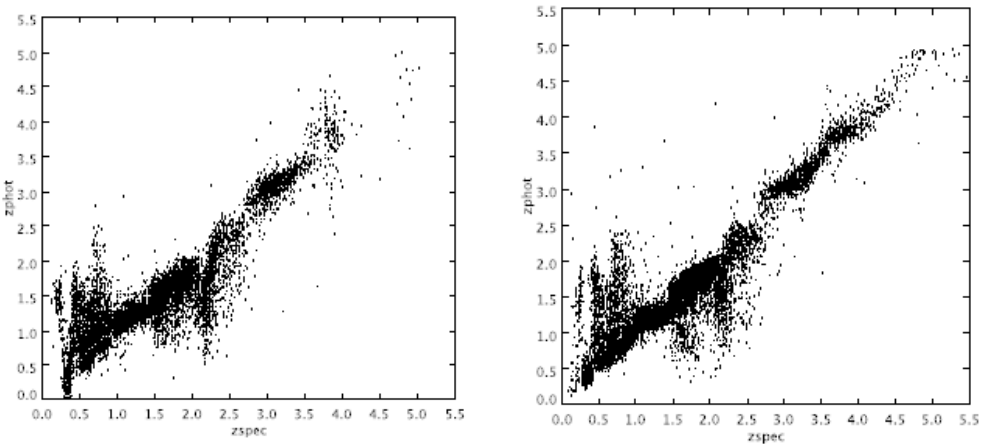

Figure 7.5: *Graphical comparison between a single network output (a) and the weak gated experts one (b). Both plots refer to QSO optical data (SDSS only).*

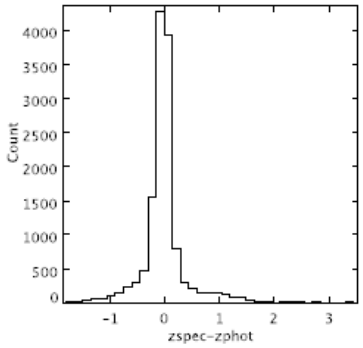

Figure 7.6: *Distribution of residuals for QSO optical photometric redshifts.*

also the errors on the colours. Introducing errors allows the network to somehow weight how training patterns contribute to the overall training process. The improvement is about 2-3%.

7.7.2 Extending the parameter space: UV observations

As already mentioned, the main aim of the present work is the production of a robust data mining method for photometric redshift estimation that is capable of use as much information as possible for the photometric estimation.

This would allow to dinamically adjust the parameter space to fit each datum, to provide our best estimation of its redshift.

Currently the Virtual Observatory lacks many features required for a data mining

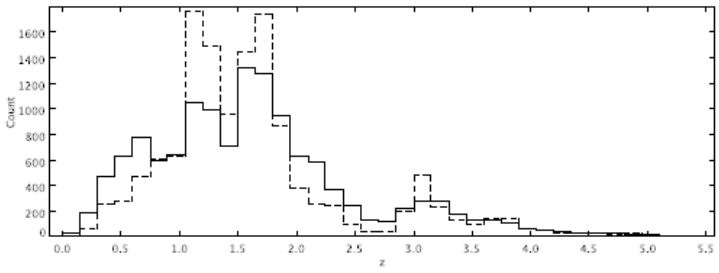

Figure 7.7: *Distribution of redshifts. Solid line: spectroscopic redshift. Dashed line: photometric redshift.*

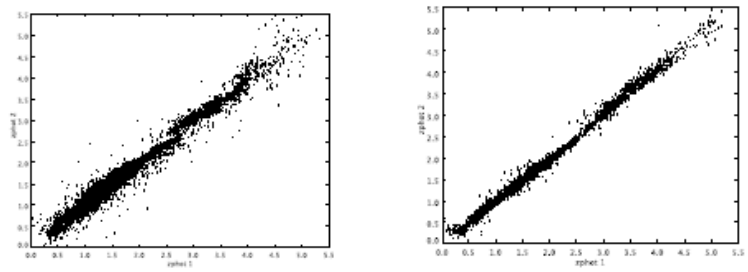

Figure 7.8: *In this figure we show how the gating network variance/bias is significantly reduced with respect to a single MLP network. Both plots show z^1_{phot} vs z^2_{phot} where the indices stand for different networks, trained on different data and with a different weights initialization. In the left panel, the photometric redshifts are from single networks, while in the right panel the photometric redshift estimation comes out from two different gating networks of the weak gated experts. Notice that the both variance and bias of the gating networks are significantly reduced.*

approach. This means that our ambitious goal has to wait until the Virtual Observatory will fit the data mining demands. The work done and described in this thesis represents a benchmark to understand what this demands are and what is the most effective way to match them.

We have already showed how the spectroscopic features may shift off the broad band filters of a photometric system. Of course these features may be found in other catalogs produced by different instruments in different ranges of the electromagnetic spectrum.

This multi-wavelength approach may resolve some of the degeneracies suffered by a single instrument's observations and increase accuracy. On the other hand, it is clear that this gain of information is counterveiled by the finite footprint of the surveys. In other words, to build a useful Base of Knowledge we need a significant overlap among different surveys in different wavelength. The cross-match among surveys is limited by physical argument, too.

For example, let's consider the UV GALEX survey (see section 7.2.2). In this survey,

only few quasars are found beyond $z \sim 2$, because the Lyman limit at 912Å shifts off the GALEX photometric bands at about that redshift. Following [71] we built a new BoK of quasars crossmatching the SDSS optical catalog and the GALEX UV one. Detailed information about this BoK is provided in section 7.2.2.

7.7.3 Applying WGE to SDSS Galaxies

While QSO photometric redshifts are a relatively new field of interest, many methods have been proposed in the last ten years for galaxies photometric redshifts estimation (see [65] and references therein).

The WGE method is fairly general, so it appears quite natural to apply it to the same BoK explored in [65]. Actually, WGE represents a possible natural evolution of the method presented in [65], also being a methodological improvement of that algorithm.

This is mainly due to the fact that SDSS galaxies are actually divided into two great classes: main sample galaxies (MSG) and luminous red galaxies (LRG). The latter are intrinsically brighter and redder than the main sample, and it can be assumed to be volume limited in the SDSS survey out to $z = 0.38$; MSG, on the other hand, are flux limited and can be detected out to $z \sim 2.5$. This physical distinction justifies the assumption that at least two different mapping functions and noise regimes could be modeled out of the data.

While the method developed in [65] relies on an early classification into LRG and MSG, our WGE doesn't need this prior classification, and can distinguish galaxies during the clustering phase.

WGE achieves good results with this dataset, slightly outperforming [65] (about 2%), but in a more robust fashion. This will allow us to explore new regions of the SDSS parameter space with a robust statistical tool: for instance, we can now try and explore the faint end of the galaxies Luminosity Function.

For the galaxies sample, we don't make any experiments using GALEX UV data, since we know that the main source of spectroscopic information for galaxies, i.e. the Balmer 4000 Å break, is always off the GALEX photometric system [72]. The only spectroscopic feature in the NUV is the shape of the continuum. However, the crossmatched BoK between GALEX and SDSS data is way more sparse than the SDSS alone: it is likely that this sparseness would countervail any information gain may come from the NUV magnitude colour.

7.8 Comparison with other methods

We will now compare our results with those from other methods. We have to stress that unlike the photometric redshift estimation for galaxies, only few attempts have been made to estimate the photometric redshift of quasars.

The two algorithms in literature we shall refer to are the Empirical Colour-Redshift Relation (CZR, [73–75]) and the k-Nearest Neighbor (kNN, [71,76]).

Other methods have been proposed, but they require a complete spectral library with templates covering all of the spectral types of sources within the sample under study. It is worth stressing, however, that these methods are more physical in nature, and provide more information on the sources under study than empirical algorithms.

7.8.1 QSO: Colour-Redshift Relation

The CZR is the method in the lot that uses the most information from the base of knowledge.

First of all, they bin the spectroscopic redshift axis. For each bin they reject the most reddened QSOs: if a quasar's $u-g$ colour is redder than the 97.5% of the other quasars in the same bin, and the $g-r$ colour is redder than the median $g-r$ colour for its bin, then they reject that object from their BoK.

Then, they construct the CZR relation by making use of the photometric errors that affect the colours and, for each object, they calculate the "mean" covariance matrix $\mathbf{V}_i$ and the "mean" colour vector $\mathbf{M}_i$. In these procedure they reject the reddest quasars again, with an iterative procedure, until $\mathbf{V}_i$ and $\mathbf{M}_i$ are unaltered.

Since they reject the reddened quasars, one can foresee that the CZR generalization capability will be much lower for these objects, which in turn will represent a good fraction of the ouliers.

To make a prediction they build a PDF by comparing each object's $\mathbf{M}$ and $\mathbf{V}$ with the binned BoK. The PDF is weighted with the *a priori* probability W_i that a quasar has a redshift in the ith bin. This is a strong assumption which may not be acceptable, since we cannot be sure that the candidate quasars follow the same redshift distribution of our spectroscopic sample.

In fact, when rejecting this assumption, the CZR performance is 5-7% worse.

The strength of the CZR approach is that all the available information in the BoK is used. Its weaknesses are the strong assumption on the redshift distribution of quasars and the fact that it requires the binning of the redshift axis: this way each bin is characterized by a unique photometric redshift value.

These argument should be enough to analize the algorithm performance. First of all, as already stated, the algorithm needs the rejection of the reddened quasars. For this

Method	Dataset	Variance	$\frac{\sigma^2}{1+z}$	$\mu\left(\frac{\Delta z}{1+z}\right)$	$\%\Delta_{0.1}$	$\%\Delta_{0.2}$	$\%\Delta_{0.3}$
kNN	S	**0.123**	**0.034**	0.095	54.9	73.3	80.7
kNNPDF	S	–	–	–	53.8	72.4	79.8
CZR	S	0.265	0.079	0.115	**63.9**	**80.2**	**85.7**
WGE	S	0.142	0.059	0.032	48.8	70.3	78.9
WGE+err	S	0.133	0.056	**0.025**	48.7	71.4	80.4
kNN	SG	**0.054**	**0.014**	0.060	70.8	85.8	90.8
kNNPDF	SG	–	–	–	71.8	86.4	90.8
CZR	SG	0.136	0.031	0.071	**74.9**	**86.9**	91.0
WGE	SG	0.058	0.030	0.022	67.9	85.2	91.1
WGE+err	SG	0.057	0.029	**0.012**	69.3	86.2	**91.3**

Table 7.3: *Comparison among different methods on the QSO datasets: k-Nearest Neighbors (with or without PDF estimation; empirical Colour-Redshift Relation and our Weak Gated Experts (WGE). "S" stands for optical SDSS colours, while "G" stands for GALEX ultraviolet colours. The best results for each column are highlighted.*

reason it's not a surprise that a large number of outliers is made of these objects. Also, the binning procedure enlarges the overall error on the predictions (e.g. the variance of the residuals). However, this method is the one that allows the most redshifts to be correctly predicted.

In [73] photometric redshifts for the SDSS Early Data Release (EDR) are provided, while in [75] only the Δz distribution is provided for the DR3 SDSS data. In order to make a comparison on homogeneous datasets, in [76] both the CZR and the kNN algorithms are implemented: for this reasons in table 7.3 we will refer to the figures in [76] for the CZR method.

7.8.2 QSO: k-Nearest Neighbors

Unlike the the other methods this one is *instance based*. This means that the BoK is not used to derive a model (WGE) or a parametrization (CZR). Instead, at prediction time, all the BoK must reside into "memory". For each object for which we want to make a prediction, the k nearest objects are taken into account, and the photometric redshift of the source is the average of the photometric redshifts of its neighbors, weighted over the reciprocal of the distance.

This approach has the significant advantage of taking into account all the BoK for each prediction, at the price of being more computing intensive, since for each predictions a large number of distances has to be calculated. In this simple case the errors on the photometric colours are not taken into account.

The main strength of this algorithm is that it uses all the BoK for each prediction.

Bin	$\sigma(\Delta z)$	$\sigma_r(\Delta z)$	$\%\sigma_r$	$\%2\sigma_r$	$\%\Delta_T$
1.06-1.44	0.355	0.170	64	78	56
1.44-1.82	0.372	0.148	62	79	63
1.82-2.20	0.476	0.172	56	80	56
2.20-2.60	0.470	0.171	62	86	77
2.60-3.00	0.302	0.153	69	94	69
3.00-3.50	0.205	0.115	69	94	78
3.50-4.00	0.268	0.140	70	94	82
4.00-4.50	0.333	0.167	52	87	71

Table 7.4: *For each z_{phot} bin, this table lists several figures in order to find a suitable characterization of the error. See text for details.*

Also, it does not need to reject objects. However, since the parameter k is unique, the same number of nearest objects must used in all the parameter space regions. The overall error is better than the CZR one, but larger than the WGE one.

7.8.3 QSO: k-Nearest Neighbor with PDF estimation

This approach is identical to the previous one. However, the errors on the colours are taken into account to find a redshift PDF for each object. Due to the deficiency in the data, PDF can show two or more peaks. For single peaked distributions the redshift that corresponds to the peak is picked. When the PDF has more than one peak, the photometric redshift is assigned to the value of the highest peak.

The PDF is derived by sampling a multivariate Gaussian where the mean value is the colour value, and the variances are assumed to be equal to the photometric error of SDSS table. For each point in this sample the kNN method is run and the photometric redshift is measured, so to determine the PDF distribution.

Surprisingly, for the Optical sample this method is outperformed by the simple kNN algorithm. For the Optical+UV sample, instead, the kNN-PDF algorithm outperforms its simpler version, as one would expect.

7.9 Error bars

Estimating errors for neural networks predictions is a tricky task, which has been addressed in many papers ([69] and references therein, [77]).

The main noise and error sources are described in appendix A.1.5: the knowledge of these contributions can lead to the estimation of error bars for neural network predictions.

However, for many real world problems, the noise processes are difficult to model, and we have to take into account the physical properties of the data, in order to estimate these effects.

In this section we shall present the problem of estimating error bars for photometric redshifts of quasars (and to some extent of galaxies).

It's worth stressing that we shall always refer to the noise in the BoK, i.e. in the photometric information from a sample of spectroscopically confirmed quasars. When dealing with candidate QSO's other effects have to be taken into account, since selection algorithms have their own efficiency and contamination issues [75,78].

Then, we shall try to tackle the problem from a statistical point of view, with two approaches: an empirical *a posteriori* approach, and a more formal one.

Degeneracies

Most of the outliers ($|\Delta z| > 0.3$) are neither extended nor reddened quasars: these objects show a colour-redshift degeneracy. Both [73] and [71] show that the colours of these quasars are consistent with at least two different redshifts.

The only way of removing such degeneracies is to add photometric information in other e.m. bands.

In figure 7.20 the redshifts at which emission lines shift from one band to the other, or completely off the SDSS photometric system, are shown. It is clear that at these redshifts most of the degeneracies are "created".

7.9.1 Error bars from z_{phot} binning

If we bin the photometric redshift axis, we can analyze the distribution of spectroscopic redshifts in each bin as well as the distribution of residuals $\Delta z = z_{spec} - z_{phot}$.

For each bin we want to find a good estimate of the residuals distribution variability: since these distributions are not gaussian, the standard deviation is not related to any confidence interval. Also, standard deviation is sensitive to outliers, leading to an overestimate of the distribution spreading.

Thus, we decided to measure both the standard deviation and the so called *median absolute deviation* (mad) which, for a vector X is defined as

$$\sigma_r = \text{median}(|X - \text{median}(X)|).$$

Then, we measured the number of objects whose $|\Delta z|$ value is lower than σ_r and $2\sigma_r$. We also measured the number of sources whose spectroscopic redshift is actually in the considered bin, $\%\Delta_T$.

In table 7.4 all these estimates are given, while in figures from 7.14 to 7.22 different plots for each bin are shown: distribution of z_{spec}, superimposed to the distribution of z_{phot}; distribution of the residuals.

From table 7.4 one can see that the probability of a source to be within one σ_r is, with only two exceptions, between 62% and 70%. So in first approximation σ_r can be interpreted as an interval confidence analoguous to one standard deviation.

This estimation of the error bar should take into account all the error sources, averaging over each bin. In the next section we shall discuss a possible alternative method for error estimation.

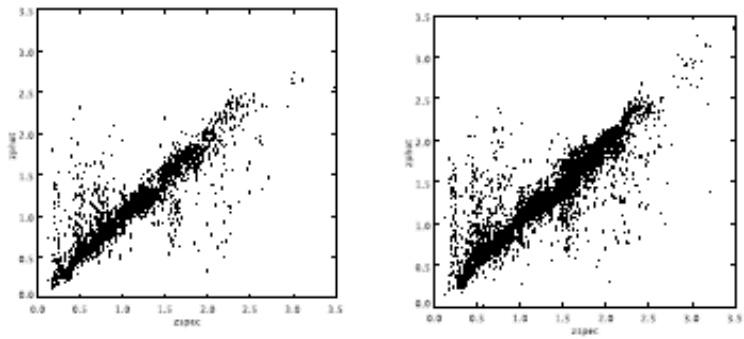

Figure 7.9: *Test set scatter plots for: (a) SDSS optical colours, plus GALEX near and far UV (3305 points); (b) SDSS otical colours, plus GALEX near UV (5833 points). Although several points still suffer by catastrophic failures, the photometric redshift estimation is significantly improved. See table 7.2 for details.*

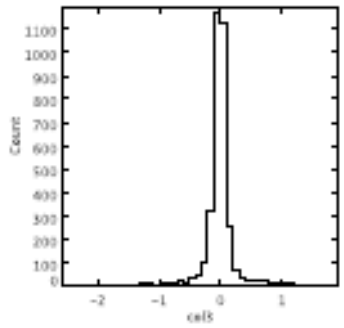

Figure 7.10: *This histogram shows the distribution of dispersion* $\Delta z = |z_{spec} - z_{phot}|$ *for the SDSS+GALEX (NUV and FUV) sample.*

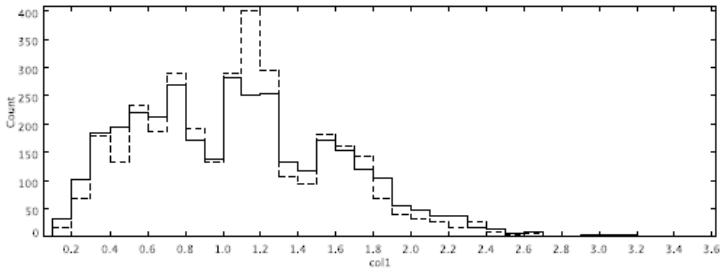

Figure 7.11: *Distribution of redshifts for the optical+FUV+NUV QSO sample. Solid line: spectroscopic redshift. Dashed line: photometric redshift.*

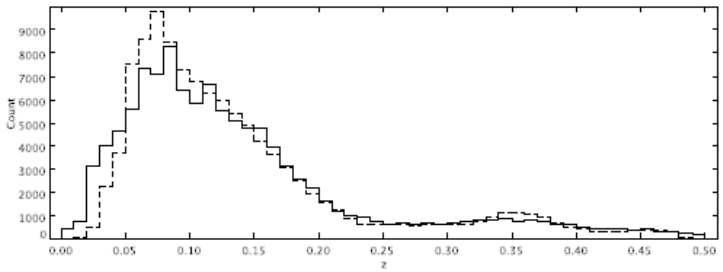

Figure 7.12: *Distribution of redshifts for the galaxy sample. Solid line: spectroscopic redshift. Dashed line: photometric redshift.*

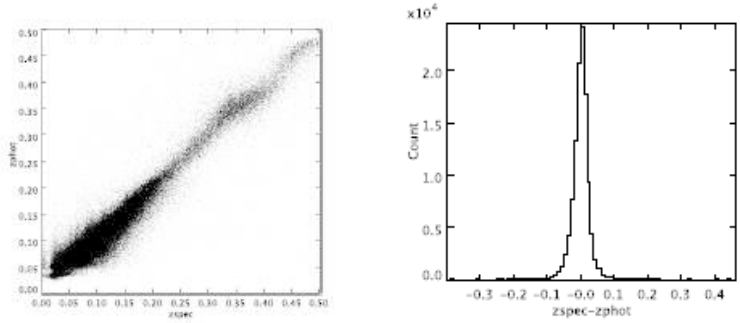

Figure 7.13: *(a) Test set scatter plot for SDSS galaxies; (b) distribution of the residuals* Δz.

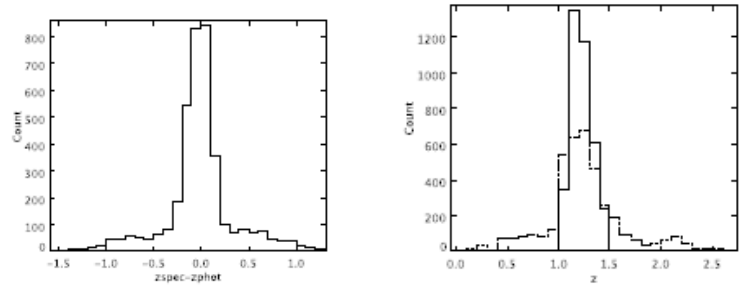

Figure 7.14: *(a) Distribution of the residuals in the 1.06-1.44 bin; (b) distribution of both* z_{spec} *(dashed line) and* z_{phot} *(solid line).*

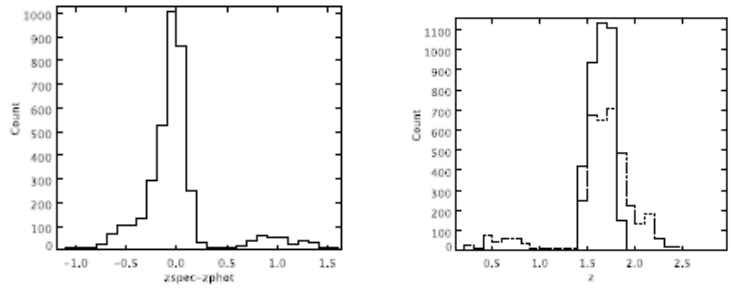

Figure 7.15: *(a) Distribution of the residuals in the 1.44-1.82 bin; (b) distribution of both z_{spec} (dashed line) and z_{phot} (solid line).*

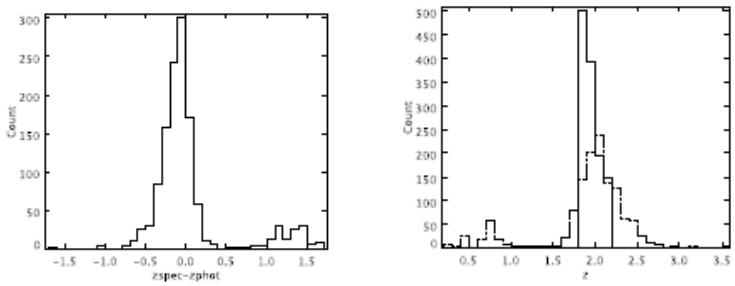

Figure 7.16: *(a) Distribution of the residuals in the 1.82-2.20 bin; (b) distribution of both z_{spec} (dashed line) and z_{phot} (solid line).*

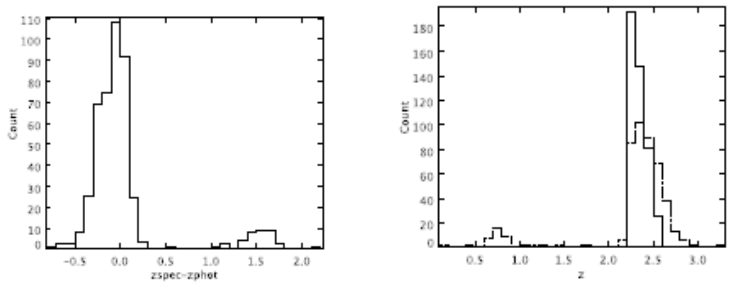

Figure 7.17: *(a) Distribution of the residuals in the 2.20-2.60 bin; (b) distribution of both z_{spec} (dashed line) and z_{phot} (solid line).*

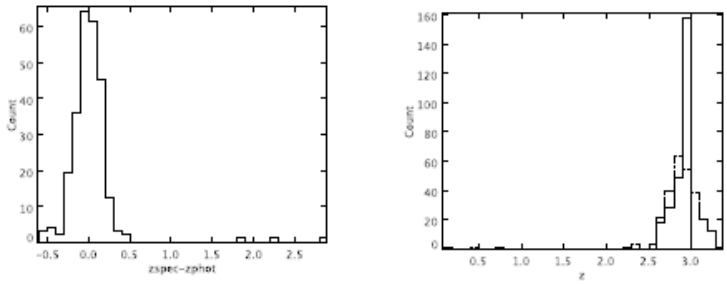

Figure 7.18: *(a) Distribution of the residuals in the 2.60-3.00 bin; (b) distribution of both z_{spec} (dashed line) and z_{phot} (solid line).*

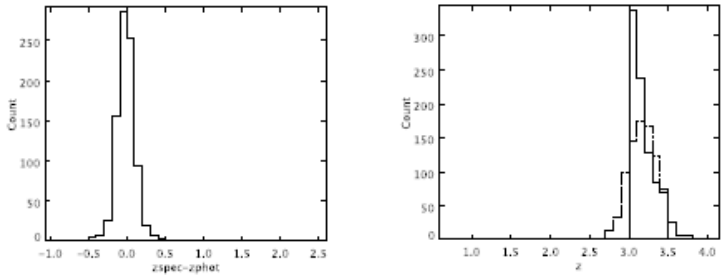

Figure 7.19: *(a) Distribution of the residuals in the 3.0-3.5 bin; (b) distribution of both z_{spec} (dashed line) and z_{phot} (solid line).*

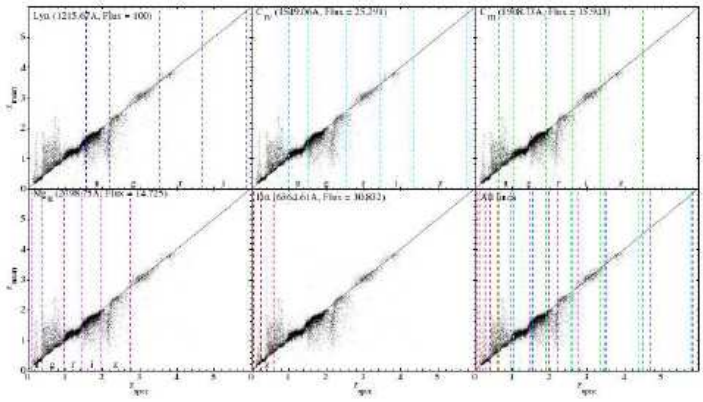

Figure 7.20: *This figure shows the redshift at which some emission lines shift from one band to the other, or completely off the SDSS photometric system. At these redshifts degeneracies are likely to arise.* **From [71]**.

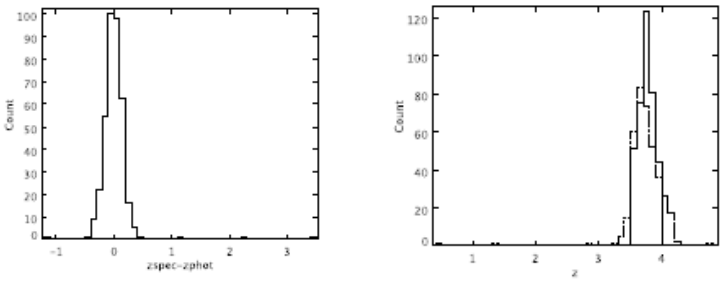

Figure 7.21: *(a) Distribution of the residuals in the 3.5-4.0 bin; (b) distribution of both z_{spec} (dashed line) and z_{phot} (solid line).*

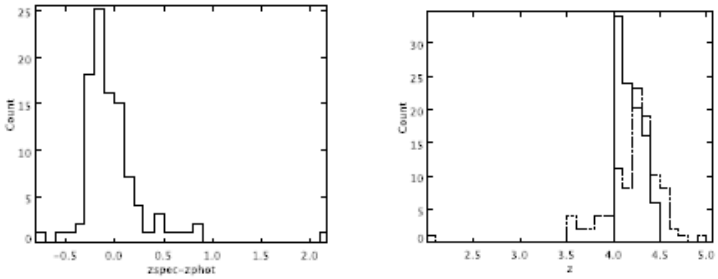

Figure 7.22: *(a) Distribution of the residuals in the 4.0-4.5 bin; (b) distribution of both z_{spec} (dashed line) and z_{phot} (solid line).*

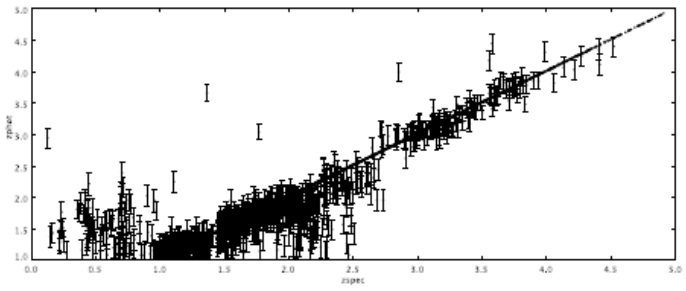

Figure 7.23: *A subsample of about one tenth of the total number of objects in the QSO test set, with error bars, as calculated by the method described in 7.9.1*

Chapter 8

Serching for Cosmic Strings: CMB Analysis

As the Universe expands, the temperature of the plasma falls down to the recombination temperature, the formation of matters becomes energetically favorable, and the photons begin to propagate freely in space, producing the surface of the last scattering (LSS). There is a small anisotropy in the temperature of the LSS, of the order of 10^{-5}. The amplitude vibration of the surface of last scattering is a function of the multipole number. In the low-multipole part of the angular spectrum, the Standard Cosmological Model is not in very good agreement with observational data and such disagreement can be traced to several causes among which a non-trivial topology of the Universe, or the presence of one or at most a few cosmic strings.

In order to test the latter hypothesis, we investigated the signature left on the CMB by a single straight infinite cosmic string moving with constant velocity in a homogeneous and isotropic background. As mentioned in section 6.2, a moving string might generate a large scale CMB anisotropy according to a simple Doppler mechanism. The total effect is a sequence of zones of decreased and increased temperature in a pattern which, moving toward the string can be schematized as a cold spot right in front of the moving string followed by a step-like jump across the string and then by a hot spot immediately after the string and, finally, another cold spot. The amplitudes of these discontinuities and their extensions depend on the position of the string with respect to the observer, on the string velocity and its direction, and on the string linear density, but the structure is always the same. At present there is no evidence of their presence, and the data gathered by modern space missions (such as WMAP) show that, if the strings do exist, their contribution to the total anisotropy is very low. This implies that the S/N ratio between the string signal and the CMB anisotropy is very low. Therefore, in order to recognize the possible signal introduced by a cosmic string, we need to create a filter finely tuned to work with very low S/N ratios.

In this chapter, I shall briefly extimate the geometrical structure of the anisotropy front; then I shall describe the $C++$ code (section 8.2) implemented in order to simulate the effects on CMB temperature distribution by the presence of a vertical straight cosmic string. This code is based on standard tools like HEALPix [79] and CMBFast [80] and, due to its computational complexity, it has been written for parallel computing. In particular, in order to create a huge number of simulations covering the whole param-

eter space, it was run on the GRID infrastructure of PON S.Co.P.E.. Then two different filters (section 8.4) were created, in order to detect such effects. Their efficiency was evaluated by a statistical analysis on a solid set of simulated maps of CMB, both with and without string, created by varying some characteristic parameters (section 8.3). In 8.5 the results of statistical analysis on simulated data are shown. Finally, in 8.6, I shall present the results of one of the two filters on real data of WMAP 5 year release.

8.1 A cosmic string inside the LSS

Let us consider the position of a cosmic string with respect to the surface of the last scattering in some fixed epoch.

As string model we will consider a straight string without ends. It means that the string has points of intersection with the LSS at each epoch. Obviously this model string extends well beyond the LSS, but the Thomson depth prevents observation of remote part of the string which situated behind the LSS.

One can choose a coordinate frame (centered on the string and comoving with it) in which the linearized metric of cosmic string can be reduced to a Minkowskian metric [3]:

$$\hat{g}_{\mu\nu} = \eta_{\mu\nu} = diag(1, -1, -1, -1)$$

In this coordinate frame, the space becomes conical and the cylindrical coordinates $\hat{\zeta}$ (vertical coordinate) and $\hat{\rho}$ (radial coordinate) have standard arbitrary values, while the angular coordinate changes in the range $0 \leq \hat{\Phi} \leq 2\pi - \alpha$, where α is the deficite angle. Such space time is locally euclidean, while globally it is non-euclidean but conical. The LSS has a spherical symmetry, and we choose the center of the coordinate system O in the center of the LSS of an observer. The cartesian lagrangian coordinate system $O\xi\eta\zeta$ is choosen in such a way that the string is perpendicular to the plane $\xi O\eta$ which we shall call *main plane*.

Let us consider the point S of intersection of the string and the $\xi O\eta$ plane at present epoch τ_O. Let us also designate the points A and B as the points of intersection of the string with the LSS (see Fig. 8.1). The distance from S to the observer is the shortest distance from the observer to the string. Moreover, the point S is the central point of the string segment inside the LSS. We shall designate this point as the string center. With these assumptions, the position of the string is defined completely by its central point (if the main plane is defined) and the projection of each string point onto the main plane is S.

Now, let us choose the axis $O\xi$ of our coordinate in such a way that this axis passes through S, and let designate the distance from the observer to S is ξ_s.

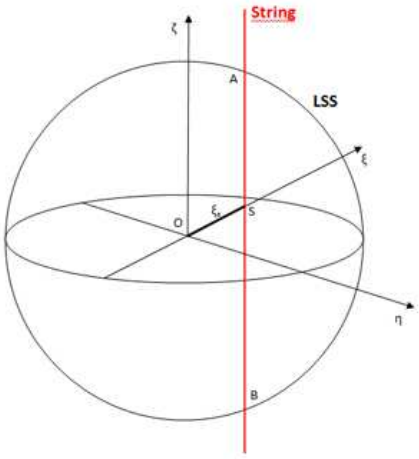

Figure 8.1: *Schematization of a cosmic string intersecting the LSS. The observer is in O, the string is perpendicular to the main plane $\xi O\eta$. The distance between string and observer is ξ_s.*

The positions of transfix points A and B are:

$$\zeta_s = \pm\sqrt{\rho_{ls}^2 - \xi_s^2}.$$

This value provides us the angular length of the string $\Delta\phi$.

$$\tan\Delta\phi = \frac{2\zeta_s}{\xi_s}. \tag{8.1}$$

We would like to mention also that the axis $O\xi$ passes through both the observer and the center of the string and one can write $\xi_s = \rho_s$.

8.1.1 The geometry of the anisotropy front.

A cosmic string is a very elongated object and the distance between the two points of intersection with the LSS is comparable with the particle horizon of the Universe. A cosmic string is a dark object, but suppose for a moment that two lights are attached to the string: one at the center and the other near point of intersection A. The distances from these two lights are different. Therefore two light signals arriving to the observer in the same moment left the point of emission at different epochs and the time difference is very long and comparable with the age of the Universe. Therefore, if the string is moving, an observer will see at any time two lights at different positions and the string front will appear to be curved [52].

Consider now the coordinate system $O\xi\eta\zeta$ of Fig. 8.1, comoving with the observer, and a second system comoving with the cosmic string $\hat{O}\hat{\xi}\hat{\eta}\hat{\zeta}$. Both are cartesian systems of lagrangian coordinates. At $t = 0$ the two coordinate systems coincide. The string is a

straight line parallel to the axis $O\zeta$ and therefore perpendicular to the main plane $O\xi\eta$. Let now the string move perpendicular to the main plane with constant velocity $\mathbf{v}$ and along a straight trajectory (for instance in the positive direction $O\eta$). Let us also choose the axis $O\xi$ in such a way that it passes through the string at the initial moment.

Photons emitted by the surface of the last scattering at the moment $t = t_0$ propagate towards the observer O. The observer registers a CMBR anisotropy generated by a point A on the string at $t = 0$ (for simplicity we consider $t_0 < 0$). The more distant from the main plane the point A is, the longer takes to the signal to reach the observer [52].

The coordinates of the point A in the coordinate system of the cosmic string are:

$$\begin{aligned}\hat{t} &= -\frac{1}{c}\sqrt{a_\eta^2 + a_\xi^2 + a_\zeta^2},\\ \hat{\eta} &= a_\eta,\\ \hat{\xi} &= a_\xi,\\ \hat{\zeta} &= a_\zeta,\end{aligned}$$

because the total time for the signal to go from the point A towards the observer O is $\sqrt{a_\eta^2 + a_\xi^2 + a_\zeta^2}/c$.

The coordinate system of the string is moving with respect to the coordinate system of the observer with velocity $\mathbf{v}$. Therefore, the observer coordinate system is moving with respect to the string coordinate system with velocity $-\mathbf{v}$, and the coordinates of the point A in the observer coordinate system are:

$$\left\{\begin{array}{rcl} t &=& \dfrac{1}{\sqrt{1-\beta^2}}\left(-\dfrac{1}{c}\sqrt{a_z^2 + a_y^2 + a_x^2} - \dfrac{v}{c^2}a_z\right),\\ \eta &=& \dfrac{1}{\sqrt{1-\beta^2}}\left(a_\eta - v\cdot\left(-\dfrac{1}{c}\sqrt{a_\eta^2 + a_\xi^2 + a_\zeta^2}\right)\right),\\ \xi &=& a_\xi,\\ \zeta &=& a_\zeta. \end{array}\right. \tag{8.2}$$

We then apply Lorentzian coordinate transformations.

Let us define the distance between the observer O and the string at the initial moment as R, which is measured in units of the radius of the last scattering surface, $a_\xi = R$. If $\beta = v/c$ and the Lorentz-factor is $1/\sqrt{1-\beta^2} = \gamma$ then the η-coordinate of the point A in the observer c.s. is:

$$\eta = \gamma(a_\eta + \beta\sqrt{a_\eta^2 + R^2 + \zeta^2}). \tag{8.3}$$

Equation (8.3) defines the string front. In other words it is a border of the CMBR anysotropy discontinuity [81]. Therefore, if we take into account the above discussed

time retardation, then the equation of the string front in the observer coordinate system becomes a hyperbola. Its vertex is in the intersection of string with the main plane and the hyperbola is symmetric with respect to the axis $O\eta$. The parameter a_η characterizes the location of the intersection point of the string and the main plane in the string coordinate system, and ζ is the altitude of a string point over the main plane. So, if, for example, the observer O registers the front vertex at the point $\{\eta = 0, \xi = R, \zeta = 0\}$ at $t = 0$, then $a_\eta = -\beta R\gamma$.

At $\zeta = 0$ (the intersection point of the string and the main plane) the radius of curvature of the front is

$$r = \frac{\left[1 + \left(\frac{d\eta}{d\zeta}\right)^2\right]^{3/2}}{\left|\frac{d^2\eta}{d\zeta^2}\right|} = \left(\frac{\gamma\beta}{\sqrt{a_\eta^2 + R^2}}\right)^{-1}.$$

Let the observer see the string front, where the distance from the front vertex to the origin of the coordinate system $O\eta$ is $\Delta\eta$. In this case the η-coordinate of the front vertex in the string coordinate system can be easyly found by posing in (8.3) $\eta = \Delta\eta$:

$$a_\eta = \gamma(\Delta\eta - \beta\sqrt{(\Delta\eta)^2 + R^2}). \tag{8.4}$$

The equations (8.3)-(8.4) define the profile of string front for any observed position of the string with respect to the chosen coordinate system of the observer.

8.2 Simulation code

In order to study the effects of a cosmic string on the CMB, I created a software capable to simulate the step-like discontinuity induced by the cosmic string. This software has been written in C++, making use of the HEALPix package, the standard data structure used for WMAP and Planck. Due to its close relation with HEALPix, this code can be easily interfaced with CMBFAST (a code for calculating the linear CMB anisotropy, see section 8.2.2) and other tools for CMB analysis. It is worth to stress that, at the moment, this code is able to mimic only straight strings and does not consider the effect of retardation of photons.

According to the simple model discussed above [81], the CMB anisotropy generated by moving cosmic string can be written as:

$$\frac{\delta T}{T} = 4\pi G\mu\beta\left(\pm 1 - \frac{\Phi_r}{\pi}\right)\frac{\cos\phi\sin\theta}{1 - \beta\sin\phi\sin\theta}, \tag{8.5}$$

where $\theta \in [0, \pi]$ and $\phi \in [-\pi, \pi]$ are latitude and longitude on the sphere, $\beta = \frac{v}{c}$ is the projection of string velocity on the line perpendicular to the one joining the source and the observer and

$$\tan \Phi_r = \frac{\sin\phi \sin\theta}{\cos\phi \sin\theta - R},$$

being R the ratio between the distances observer-string and observer-LSS. Naming κ the direction of propagation of the string, defined as the angle between the velocity vector and the line of sight, then we can rewrite equation 8.5 as

$$\frac{\delta T}{T} = 4\pi G\mu\beta \left(\pm 1 - \frac{\Phi_r}{\pi}\right) \frac{\sin(\kappa - \phi)\sin\theta}{1 - \beta\cos(\kappa - \phi)\sin\theta}. \tag{8.6}$$

Equation 8.6 is the one used to generate the simulated temperature anisotropy due to the cosmic string.

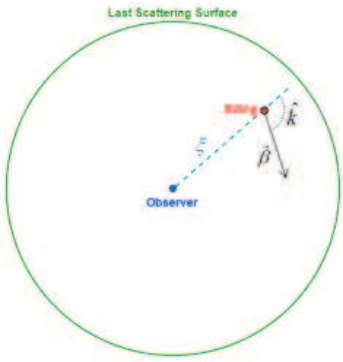

Figure 8.2: *String parameters used for the simulations.*

In order to implement equation 8.6 into the code, it's necessary to define 3 parameters of the string (Fig. 8.2):

1. the magnitude β of velocity of the string (set c=1);

2. string direction κ;

3. distance ξ between the observer and the string, setting the distance observer-last scattering surface equal to 1.

In Fig. 8.3 the flow-chart of our code is shown: the user sets string parameters and then the code generates the temperature distribution map, in according to eq. 8.6.

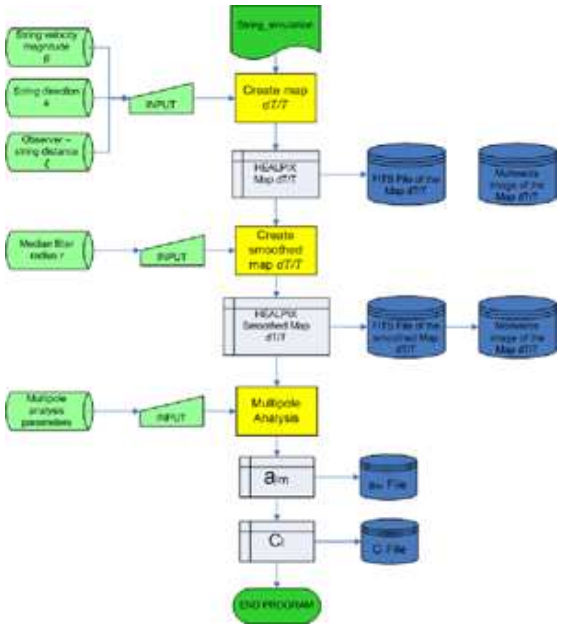

Figure 8.3: *Flow-chart of the string signature simulation procedure. Starting from the string parameters, a $\Delta T/T$ map is generated and the harmonical analysis is performed. For each simulation, a map file, an image file, and a_{lm}s and C_ls are created*

Then the map is stored in a FITS[1] file, and a TGA[2] image is created from it. Successively, in order to simulate realistic resolution of available data, a median filter of arbitrarily selected radius is performed in order to smooth the temperature distribution and a new TGA image of the smoothed map is created. The subsequent step is a multipole analysis, to compute the a_{lm}s and C_ls coefficients.

Examples of maps generated with different parameters are depicted in Fig. 8.4.

By varying the string parameters according to what reported in Tab. 8.2, more than 3000 maps of temperature distribution were generated thus covering the whole string parameter space.

In order to reduce the computational time and to produce a large number of simulations, we were obliged to recur to 64 processors of the GRID infrastructure S.Co.P.E.. In about 6 hours of CPU time 3040 simulations of maps were generated and 18240 files

[1]FITS or Flexible Image Transport System is a digital file format used to store, transmit, and manipulate scientific and other images. FITS is the most commonly used digital file format in astronomy. Unlike many image formats, FITS is designed specifically for scientific data and hence includes many provisions for describing photometric and spatial calibration information, together with image origin metadata.

[2]Truevision's (now AVID) TGA File Format, often referred to as TARGA File Format, is a raster graphics file format. It was the native format of Truevision Inc.'s TARGA and VISTA boards, which were the first graphic cards for IBM-compatible PCs to support Highcolor/truecolor display. The format can store image data with 8, 16, 24, or 32 bits of precision per pixel the maximum 24 bits of RGB and an extra 8-bit alpha channel. Color data can be color-mapped, or in direct color or truecolor format.

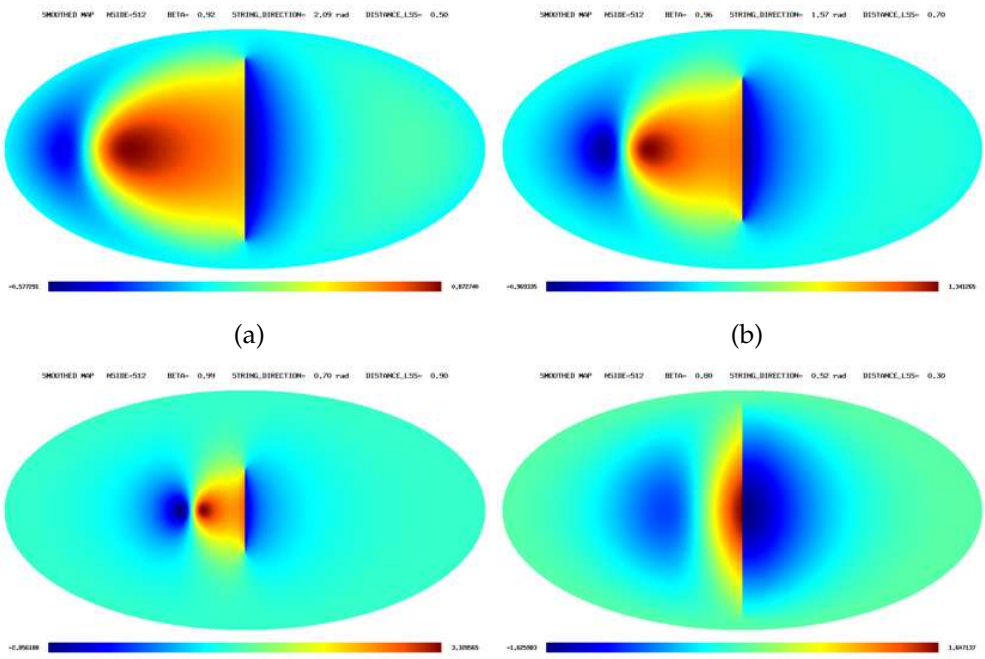

(a) (b)

(c) (d)

Figure 8.4: *Examples of simulations of straight cosmic string signature in the CMB for different values of parameters: a)* $\beta = 0.92$, $\kappa = 120°$, $\xi = 0.50$*; b)* $\beta = 0.96$, $\kappa = 90°$, $\xi = 0.70$*; c)* $\beta = 0.99$, $\kappa = 40°$, $\xi = 0.9$*; d)* $\beta = 0.80$, $\kappa = 30°$, $\xi = 0.30$.

β	κ	ξ
$0.0 \div 0.9$		
0.920		
0.940		
0.960	$0 \div 180$	$0.0 \div 0.9$
0.980		
0.985		
0.990		
0.992		

Table 8.1: *Parameters used for string simulations*

were saved on a storage element of the GRID:

- 6080 FITS files (divided into smoothed and unsmoothed maps),
- 6080 TGA images,

- 3040 a_{lm}s files,
- 3040 C_ls files,

for a total of about 100 GB of compressed data.

8.2.1 HEALPix

The numerical analysis of functions on the sphere involves a class of mathematical operations (like convolutions with local and global kernels, Fourier analysis with spherical harmonics and power spectrum estimation, wavelet decomposition, nearest-neighbour searches etc.), whose objects are discretised maps, i.e. quantizations of arbitrary functions according to a chosen tessellation (exhaustive partition of the sphere into finite area elements). Some of these operations become prohibitively slow if the sampling of functions on the sphere, and the related structure of the discrete data set, are not designed carefully. Moreover, the need of discretization of the map comes from the nature of data: typically, a whole sky map rendered by a CMB experiment contains: (i) signals coming from the sky, which are by design strongly band-width limited (in the sense of spatial Fourier decomposition) by the instrument's angular response function, and (ii) a projection into the elements of a discrete map, or pixels, of the observing instrument's noise; this pixel noise should be random, and white, with a band-width significantly exceeding that of all the signals.

To this aim, a number of tessellations have been used for discretisation and analysis of functions on the sphere, but only HEALPix (*Hierarchical Equal Area and iso-Latitude Pixelization*) satisfies simultaneously three stated requirements of the mathematical structure of discretised full sky maps:

1. **hierarchical structure of the data base.** This is recognized as essential for very large data bases, and was postulated in construction of the Quadrilateralized Spherical Cube (or quad-sphere), [82], which was used for the COBE data. The data elements which are nearby in a multi-dimensional configuration space (here, on the surface of a sphere), are also nearby in the tree structure of the data base, hence the near-neighbour searches are conducted optimally in the data storage medium or computer RAM. This property, especially when implemented with a small number of base resolution elements, facilitates various topological methods of analysis, and allows easy construction of wavelet transforms on quadrilateral (and also triangular) grids. Fig. 8.5 shows how a hierarchical partition with quadrilateral structure naturally allows for a binary vector indexing of the data base;

2. **equal areas of discrete elements of partition.** This is advantageous because *(i)* white noise generated by the signal receiver gets integrated exactly into white

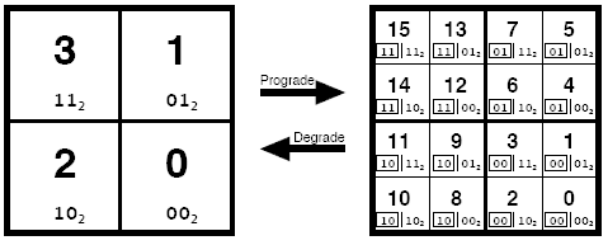

Figure 8.5: *Quadrilateral tree pixel numbering. The coarsely pixelised coordinate patch on the left consists of four pixels. Two bits suffice to label the pixels. To increase the resolution, every pixel splits into 4 daughter pixels shown on the right. These daughters inherit the pixel index of their parent (boxed) and acquire two new bits to give the new pixel index. Several such curvilinearly mapped coordinate patches (12 in the case of HEALPix, and 6 in the case of the COBE quadsphere) are joined at the boundaries to cover the sphere. All pixels indices carry a prefix (here omitted for clarity) which identifies which base-resolution pixel they belong to.*

noise in the pixel space, and *(ii)* sky signals are sampled without regional dependence, except for the dependence on pixel shapes, which is unavoidable with tessellations of the sphere. Hence, as much as possible given the experimental details, the pixel size should be made sufficiently small compared to the instrument's resolution to avoid any excessive, and pixel shape dependent, signal smoothing;

3. **iso-Latitude distribution of discrete area elements on a sphere.** This property is critical for computational speed of all operations involving evaluation of spherical harmonics, since the associated Legendre polynomial components of spherical harmonics are evaluated via slow recursions, and can not be simply handled in an analogous way to the trigonometric Fast Fourier Transform. It is precisely this property that the COBE quad-sphere is lacking, and this renders it impractical for applications to high resolution data.

HEALPix is a genuinely curvilinear partition of the sphere into exactly equal area quadrilaterals of varying shape (Fig. 8.6). The base-resolution comprises twelve pixels in three rings around the poles and equator. The base parameter to express the resolution of the grid is N_{side}, which defines the number of divisions along the side of a base-resolution pixel that is needed to reach a desired high-resolution partition.

All pixel centers are placed on $4 \times N_{side} - 1$ rings of constant latitude, and are equidistant in azimuth (on each ring). All iso-latitude rings located between the upper and lower corners of the equatorial base-resolution pixels, the equatorial zone, are divided into the same number of pixels: $N_{eq} = 4 \times N_{side}$. The remaining rings are located within the polar cap regions and contain a varying number of pixels, increasing from ring to ring with increasing distance from the poles by one pixel within each quadrant.

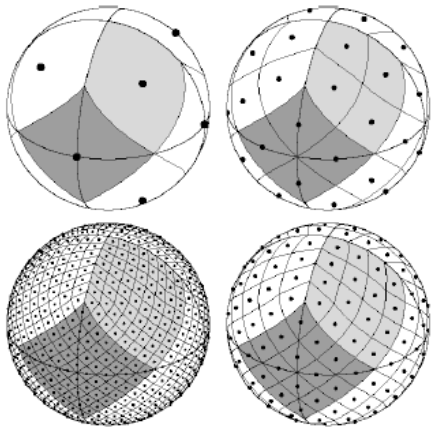

Figure 8.6: *Orthographic view of HEALPix partition of the sphere. Overplot of equator and meridians illustrates the octahedral symmetry of HEALPix. Light-gray shading shows one of the eight (four north, and four south) identical polar base-resolution pixels. Dark-gray shading shows one of the four identical equatorial base-resolution pixels. Moving clockwise from the upper left panel the grid is hierarchically subdivided with the grid resolution parameter equal to* $N_{side} = 1, 2, 4, 8$*, and the total number of pixels equal to* $N_{pix} = 12N_{side}^2 = 12, 48, 192, 768$.

Specific geometrical properties allow HEALPix to support two different numbering schemes for the pixels, as illustrated in Fig. 8.7:

- in the *RING scheme*, one can simply count the pixels moving down from the north to the south pole along each iso-latitude ring. It is in the RING scheme that Fourier transforms with spherical harmonics are easy to implement;

- in the *NESTED scheme*, one can arrange the pixel indices in twelve tree structures, corresponding to base-resolution pixels. Each of those is organised as shown in Fig. 8.5. This tree structure allows one to implement efficiently all applications involving nearest-neighbour searches, and also allows for an immediate construction of the fast Haar wavelet transform on HEALPix.

8.2.2 CMBFAST and CMBEASY

CMBFAST is a code, implemented by by Uros Seljak and Mattias Zaldarriaga [83], for calculating the linear cosmic microwave background anisotropy spectra based on integration over the sources along the photon past light cone. In this approach the temperature anisotropy is written as a time integral over the product of a geometrical term and a source term. The geometrical term is given by radial eigenfunctions which do not depend on the particular cosmological model. The source term can be expressed in

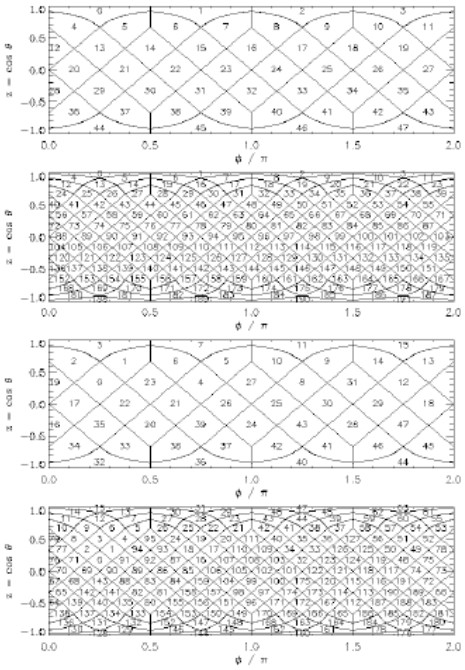

Figure 8.7: *Cylindrical projection of the HEALPix division of a sphere and two natural pixel numbering schemes (RING and NESTED) allowed by HEALPix. Both numbering schemes map the two dimensional distribution of discrete area elements on a sphere into the one dimensional, integer pixel number array. From top to bottom: Panel one (resolution parameter Nside = 2) and panel two (Nside = 4) show the RING scheme for pixel numbering. Panel three (resolution parameter Nside = 2) and panel four (Nside = 4) show the NESTED scheme for pixel numbering within which the pixel number grows with consecutive hierarchical subdivisions on a tree structure seeded by the twelve base-resolution pixels.*

terms of photon, baryon and metric perturbations, all of which can be calculated using a small number of differential equations.

This split clearly separates between the dynamical and geometrical effects on the CMB anisotropies. More importantly, it allows to significantly reduce the computational time compared to standard methods. This is achieved because the source term, which depends on the model and is generally the most time consuming part of calculation, is a slowly varying function of wavelength and needs to be evaluated only in a small number of points. The geometrical term, which oscillates much more rapidly than the source term, does not depend on the particular model and can be computed separately. Standard methods that do not separate the two terms and require a much higher number of evaluations.

CMBEASY [84] is a software package for calculating the evolution of density fluctuations in the universe, based on the CMBFAST package. Even though its ancestor is a

Fortran program, CMBEASY is fully object oriented C++. This considerably simplifies manipulations and extensions of the code. In addition, a powerful Spline class can be used to easily store and visualize data.

8.2.3 GRID computing

"Distributed" or "grid" computing in general is a special type of parallel computing that relies on complete computers (with onboard CPU, storage, power supply, network interface, etc.) connected to a network (private, public or the Internet) by a conventional network interface, such as Ethernet.

The term "grid computing" originated in the early 1990s. Its ideas (including those from distributed computing, object-oriented programming, and Web services) were brought together by Ian Foster, Carl Kesselman, and Steve Tuecke, widely regarded as the "fathers of the grid" [85]. They led the effort to create the Globus Toolkit incorporating not just computation management but also storage management, security provisioning, data movement, monitoring, and a toolkit for developing additional services based on the same infrastructure, including agreement negotiation, notification mechanisms, trigger services, and information aggregation. While the Globus Toolkit remains the de facto standard for building grid solutions, a number of other tools have been built that answer some subset of services needed to create an enterprise or global grid. In 2007 the term cloud computing came into popularity, which is conceptually similar to the canonical Foster definition of grid computing.

The basic concept of the GRID is the coordinated sharing of resources within the framework of a dynamical and multi-institutional Virtual Organization (VO). Resource sharing is not limited at file exchange, but it includes the whole hardware necessary to the resolution of a scientific, engineering or industrial problem.

The common feature of GRID projects is the necessity to have a data-intensive calculus environment, in which software need to access, quickly and reliably, to huge amount of data through the whole world. Task of the GRID is optimize these applications like all works as an unique supercomputer.

S.Co.P.E. Grid

The S.Co.P.E. (Italian acronymic for high Performance, Cooperative and distributed System for scientific Elaboration) is a research project, started in 2004, that aims at developing several applications in the field of fundamental research, which is one of its strategic objectives. The main spin off is the implementation of an open and multidisciplinar Grid infrastructure between the departments of University "Federico II", distributed in Metropolitan scale in the city of Naples. The S.Co.P.E. Architecture provides the uni-

fication of all the main computational and storage resources already available in the sites that participate at the project, using the Grid Paradigm supported by INFN-GRID distribution.

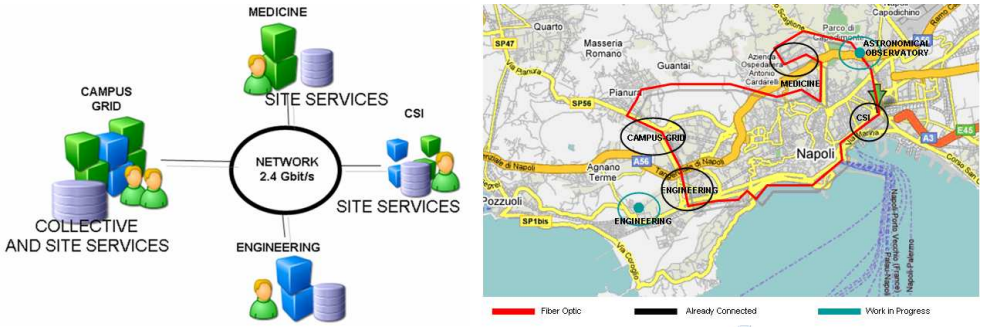

Figure 8.8: *The S.Co.P.E. Grid infrastructure: at left the current fiber optic MAN ring of the University "Federico II". In the right picture a map of the city of Naples with the main SCoPE sites. In green the departments not still connected at the "Federico II" network infrastructre.*

The computing infrastructure connectivity is supported by the metropolitan fiber optic ring that connects at 2.4Gb/s the 4 main sites of the University: Medicine, Engineering, C.S.I. (Center of Information Services) and the Campus of Monte Sant'Angelo, that accommodates the science faculty departments and are already organized in a Grid infrastructure over a fiber optic LAN at campus level (THE CAMPUS GRID). The MAN will be extended by the end with a wireless bridge towards the Astronomical Observatory of Capodimonte and a wired link to the detached engineering site.

All the peripheral sites share their resources by offering the basic Grid site services of the INFN-GRID middleware: Computing Element, Worker Node and Storage Element based on DPM. The collective services, are centralized in a new computing center open in the Campus Grid that offer Services Discovery, Resource Brokering, File Catalog, Grid Monitoring and graphical user interface.

8.3 The Dataset

In order to evaluate the capabilities of the filters that will be described in the following, a robust simulated dataset has been created. It is divided into two subsets:

- 300 "Only CMB" maps;
- 1800 "String + CMB" maps.

The "Only CMB" set is composed by maps not containing the signature of the string. These maps were produced starting from a simulated power spectrum, generated by CMBEASY.

The parameters used for the generation of the simulated power spectrum are those measured by WMAP (see Tab. 3.3.2). It is important to stress that, for our purposes, CMB maps not containing the string represent the noise that contaminates the signal (i.e. the temperature anisotropy by string).

The "String + CMB" set is instead obtained by combining the "Only CMB" maps with maps generated by the simulation code previously discussed. In particular, we used an unique representative of string maps with the following parameters:

- $\beta = 0.70$;
- $\kappa = 90°$;
- $\xi = 0.60$.

The choice of this triple is not casual: in fact, it is possible to demonstrate that by using this combination of the string parameters, the length of the resultant spot is of about $100°$, which is, as mentioned in 6.2, the minimum angular length for which it is possible to detect the string also by lensing method in the optical surveys. The simulated string, generated by this triple, is depicted in Fig. 8.9.

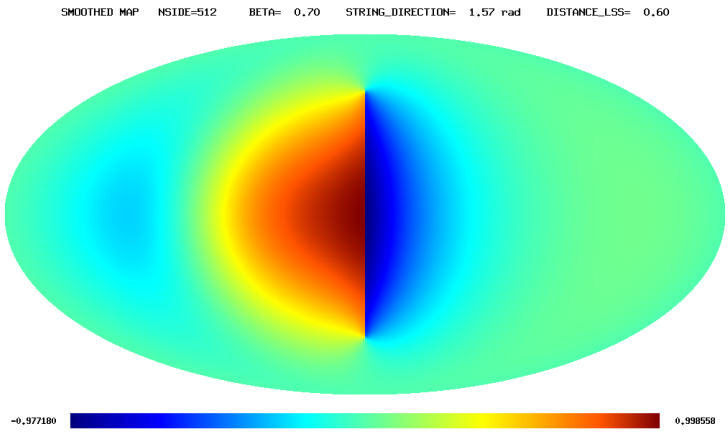

Figure 8.9: *Simulated string used for statistical analysis. Parameters of string are:* $\beta = 0.70$, $\kappa = 90°$, $\xi = 0.60$.

The two type of maps are summed together by a separate routine of the code, by using the following relation:

$$\delta T_{CMB+String}(i) = \delta T_{CMB}(i) + \alpha \delta T_{String}(i)$$

where i represents the pixel index and α is a multiplicative coefficient strictly related to the S/N ratio. Varying α, in fact, we obtain different values of S/N ratio (fluctuations due to cosmic string over CMB), in according to what is listed in Tab. 8.2.

α	**S/N Ratio**
1	0.002
5	0.01
10	0.02
15	0.03
20	0.04
30	0.06

Table 8.2: *Table of conversion α - S/N ratio*

In this way, 1800 realistic simulated images sampling the whole parameter space defined by S/N were produced. In Fig. 8.10 an example of "String + CMB" map is shown, in which, in order to stress the effects of cosmic string, we used a high S/N ratio ($\alpha = 100$).

The partition of the dataset is needed because the statistical analysis followed two different directions: the main target was the evaluation of the capability of the filters to detect the presence of a cosmic string, that is their *efficiency*; the secondary target was to evaluate the *cleanliness* of the filters, i.e. their tendency to detect false positive or spurious events. "Only CMB" maps were used to evaluate the cleanliness of the filter. In fact, each triggered event of "Only CMB" maps represents a failure of the filter. Other important information about the "cleanliness" can be derived from the analysis of "String + CMB" maps. In fact, even if the primary result of "String + CMB" analysis is the capability to detect the cosmic string signatures, it is possible to estimate how many spurious events are encountered when there is also a string, well knowing that the event caused by the string must be unique (in analysing a map, the filter must detect only one event and all the other must be regarded as spurious).

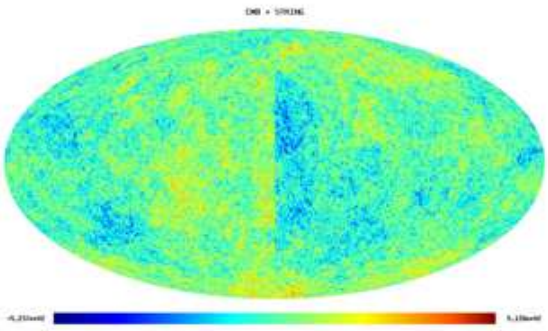

Figure 8.10: *Example of "String + CMB" map with $\alpha = 100$ (S/N ratio 0.2). CMB is been generated by CMBEASY. Parameters of string are: $\beta = 0.70$, $\kappa = 90°$, $\xi = 0.60$.*

8.4 The filters

In this section, I'm describing 2 different filters, implemented in order to detect the cosmic string signature in the CMB. Both filters are split into two steps. The first, defined *squeezing procedure*, is a way to arrange data in order to smooth the noise produced by the CMB temperature distribution and, at the same time, to amplify the step due to the presence of the string. The first part of both filters was written in C++, making use of the HEALPix libraries to manage the maps. The second step is the real filter: the first filter, called *threshold filter*, tries to detect the hot spot of the string temperature distribution; the second, named *jump filter*, searches for the step-like discontinuity in the string maps. The second part of the filters was written in MATlab, being this software very powerful in arrays and vectors management.

8.4.1 The "Squeezing" procedure

The "squeezing" procedure allows to damp the noise due to the CMB anisotropy and to amplify the string signal, so that the step like hot-cold spot, which is characteristic of a string, becomes more easily detectable.

This procedure works on data on the sphere giving, as final result, a monodimensional vector of resolution depending on the resolution of the starting HEALPix map. In this work, as previously mentioned, in order to generate maps compatible with WMAP data, we used $N_{side} = 512$, corresponding to a "squeezed" vector of 4096 pixels. In this procedure, the RING scheme of HEALPix is use, because the nature of the operations made.

The first step of the squeezing procedure is the partition of the sphere (then of the HEALPix map) in strips of $\Delta\theta = 10^{\circ}$, centered on the equator. In each strip, for fixed longitude ϕ, the average $\delta\overline{T}$ of the anisotropy values over the latitude θ is calculated, so that the map is reduced to a monodimensional vector of 4096 pairs $(\phi, \delta\overline{T}(\phi))$. Finally, all strips are summed together. In this way, we expect the signal to be amplified, due to the summation over θ (the difference between hot and cold spots improves, while the noise, being almost gaussian, is smoothed out). In Fig. 8.11, it is possible to see the effects of the squeezing on different kinds of maps: on the left side of each row, HEALPix "Only String", "Only CMB" and "String + CMB" maps ($S/N = 0.04$) respectively are shown; on the right side, the respective "squeezed" maps are depicted. The step-like discontinuity caused by the string is clearly visible in the bottom map.

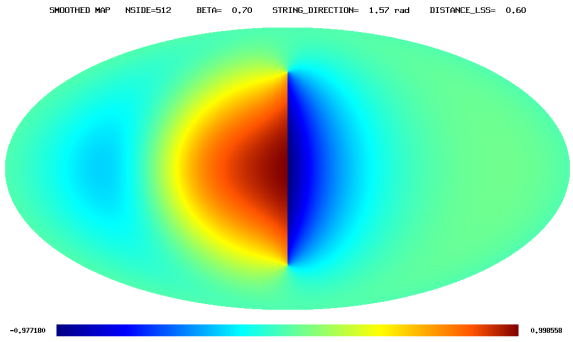

"Only String" map

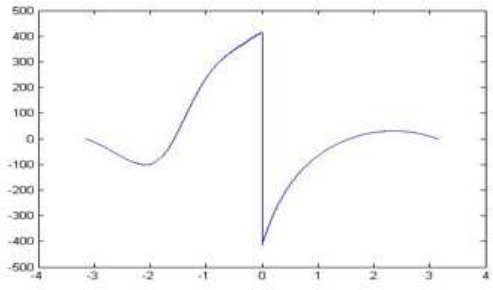

Squeezed "Only String" map

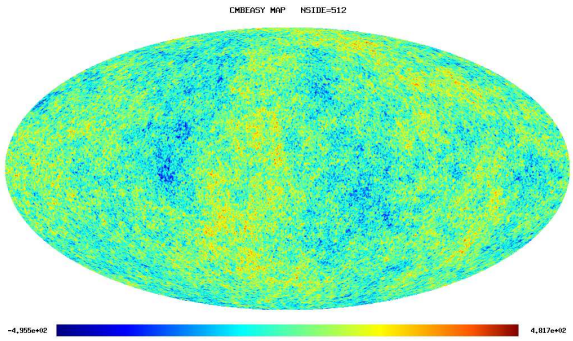

"Only CMB" map

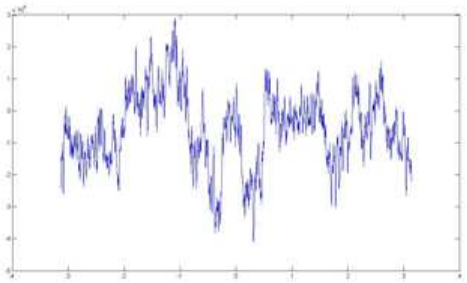

Squeezed "Only CMB" map

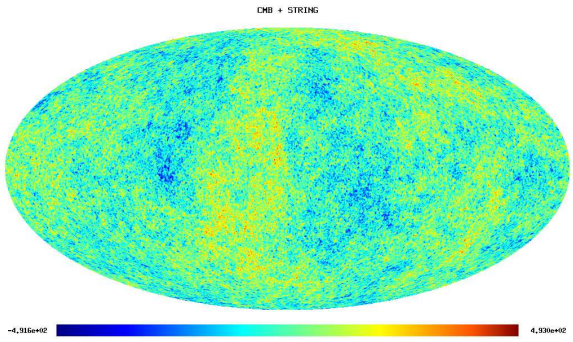

"String + CMB" map

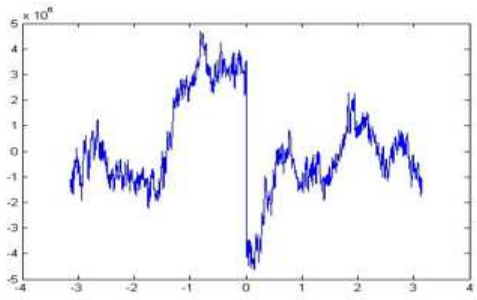

Squeezed "String + CMB" map

Figure 8.11: *Effects of the squeezing procedure on different maps:* ***top)*** *"Only String" map;* ***center)*** *"Only CMB" map;* ***bottom)*** *"String + CMB" map with* $\alpha = 20$.

8.4.2 The Threshold Filter

The first filter here proposed, called "Threshold Filter", is a simple trigger with a defined threshold. It is a dynamical threshold, in the sense that it depends on the specific map under analysis. In fact, its value is determined by the mean temperature value $\overline{T}_m$ and its standard deviation σ_m:

$$\Sigma_{threshold} = \overline{T}_m + 2\sigma_m \tag{8.7}$$

Exploring a whole squeezed map, the code searches for a certain number of consecutive pixels over the threshold (8.7). The number of consecutive pixels is a parameter of the filter, then its value is an input of the user. If the condition is fulfilled, then the detection of an event is flagged. It is clear that the choice of the parameter n, that is the number of consecutive pixels over threshold, is fundamental for the filter. The determination of optimal value of this parameter is the first step of statistical analysis performed on the threshold filter.

8.4.3 The Jump Filter

The Threshold Filter searches for "over threshold" values of the mean temperature in squeezed maps. In this way, it tries to recognize the "hot spot" at one side of the string, neglecting the step-like effect characterizing temperature fluctuations due to a cosmic string. With this view, a second filter, name "Jump Filter", has been implemented, in order to search for the step-like discontinuity caused by a straight string.

Consider a squeezed map and define a window of width l moving along the latitude φ with a step of s pixels (Fig. 8.12). It is important to stress that, in the following analysis, we arbitrarily set $l = s$.

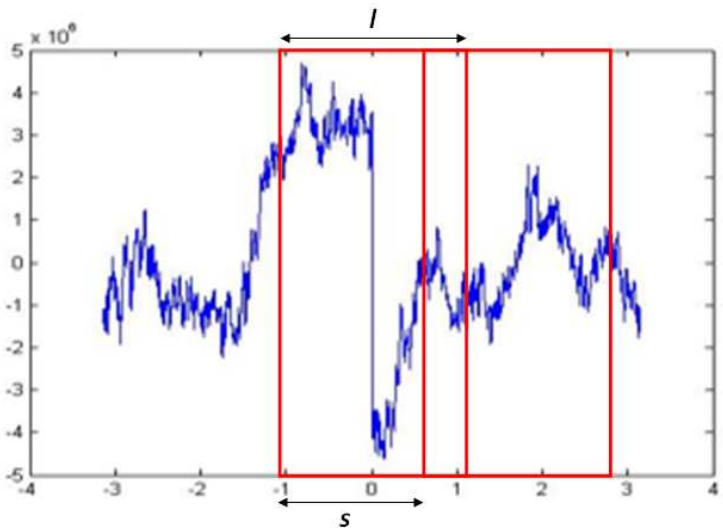

Figure 8.12: *Schematization of the functioning of the Jump Filter: the squeezed map is sampled by a window of width l and step s*

In each defined window, the difference between the maximum and minimum value of the mean temperature $\overline{T}_m$ is calculated. In this way, a vector, of length depending

on l (and s), containing the maximum differences is built. The maximum value of the vector **V** of differences is flagged as event of the map.

For this filter, two different threshold are used:

$$\begin{aligned} \Sigma_1 &= \overline{T}_m + \gamma\sigma_m; \\ \Sigma_2 &= \overline{T}_{max} + 2\gamma\sigma_{max}, \end{aligned} \tag{8.8}$$

where $\overline{T}_m$ and σ_m are, respectively, the mean value and standard deviation over all data , while $\overline{T}_{max}$ and σ_{max} are referred to the vector of maximum differences. Both thresholds depend on the parameter γ which is one of parameter evaluated in statistical analysis.

In order to be flagged as possible string candidate, one element of vector **V** has to be at least over one of two thresholds.

The second crucial parameter of the Jump Filter is the width l of the window used to sample the map: smaller is l, closer are the minimum and the maximum value of temperature, therefore higher is the probability that the difference was due to the temperature step by the string.

8.5 Statistical analysis

In this section, results of a statistical analysis on the two filters previously discussed is shown. Aim of such analysis is the evaluation of two quantity defining the capabilities of filters:

1. **efficiency**, defined as the capability of the filter to recognize temperature fluctuations due to the cosmic string. It is evaluated on 1800 "String + CMB" maps (see section 8.3). On a single map, filters give one of these possible values: 0, if the effect of cosmic string (in the following it will be called *event*) is not detected; 1 if an event is detected. The Efficiency is defined as the number of detected events over the total number of explored maps:
$$E_{filter} = \frac{N_{detected}}{N_{maps}};$$
2. **cleanliness**, is instead defined as the tendency of the filters to detect spurious events due to noise fluctuation. It is crucial because, by evaluating it on "Only CMB" maps, it is possible to determine the best values of filters parameters. On a single "Only CMB" map, the filters give one of two possible values: 0 if an event is detected (it shall be a spurious event); 1 if no event is detected. The cleanliness is defined as the number of maps in which no event is detected over the total number of maps:
$$C_{filter} = \frac{N_{no\,detected}}{N_{maps}}.$$

8.5.1 Threshold Filter analysis

Aim of statistical analysis on the threshold filter is the determination of the optimal value of the parameter n (number of consecutive over threshold), by which the best efficiency and cleanliness of filter is reached.

In Fig. 8.13 we present the results of statistical analysis on "Only CMB" data. In this case, as mentioned, the filter works well if no event is detected. By increasing the number of required consecutive pixels, the filter cleanliness grows up, reaching a maximum ($C_{threshold} = 0.79$) for $n = 50$. In this case, however, the filter detects false positives in 21% of cases.

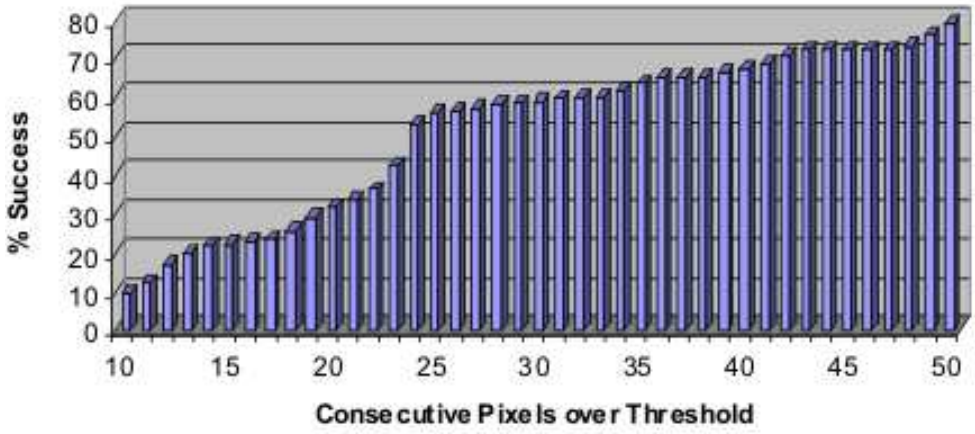

Figure 8.13: *Results of the statistical analysis performed on "Only CMB" maps as a function of the number of required consecutive pixels above threshold. The filter must be regarded as successful if no event is detected. The best filter cleanliness of 0.79 (i.e. 0.21 of spurious events detected) is reached for 50 consecutive pixels.*

In Fig. 8.14 the results of statistical analysis on the "String + CMB" data for different S/N ratios are shown.

They are summarized in Tab. 8.3, in which it is also possible to see the filter efficiency for the best value of the cleanliness n.

It is apparent that the filter works well for S/N ratios between 0.01 and 0.04. At lower S/N it fails because the signal due to the string is too low, while at higher S/N, it fails since the threshold becomes too high.

In addition, we have to consider the fact that the filter can not recognize spurious events in presence of a string. In Tab. 8.4, the fraction of spurious events detected in "String + CMB" maps, as function of the S/N ratio and, in the last column, the same fraction for the best value of n. Even if the total cleanliness as function of the S/N ratio is quite low, it results maximum for $n = 50$.

In conclusion, this filter has very high efficiency in a limited range of S/N ratios

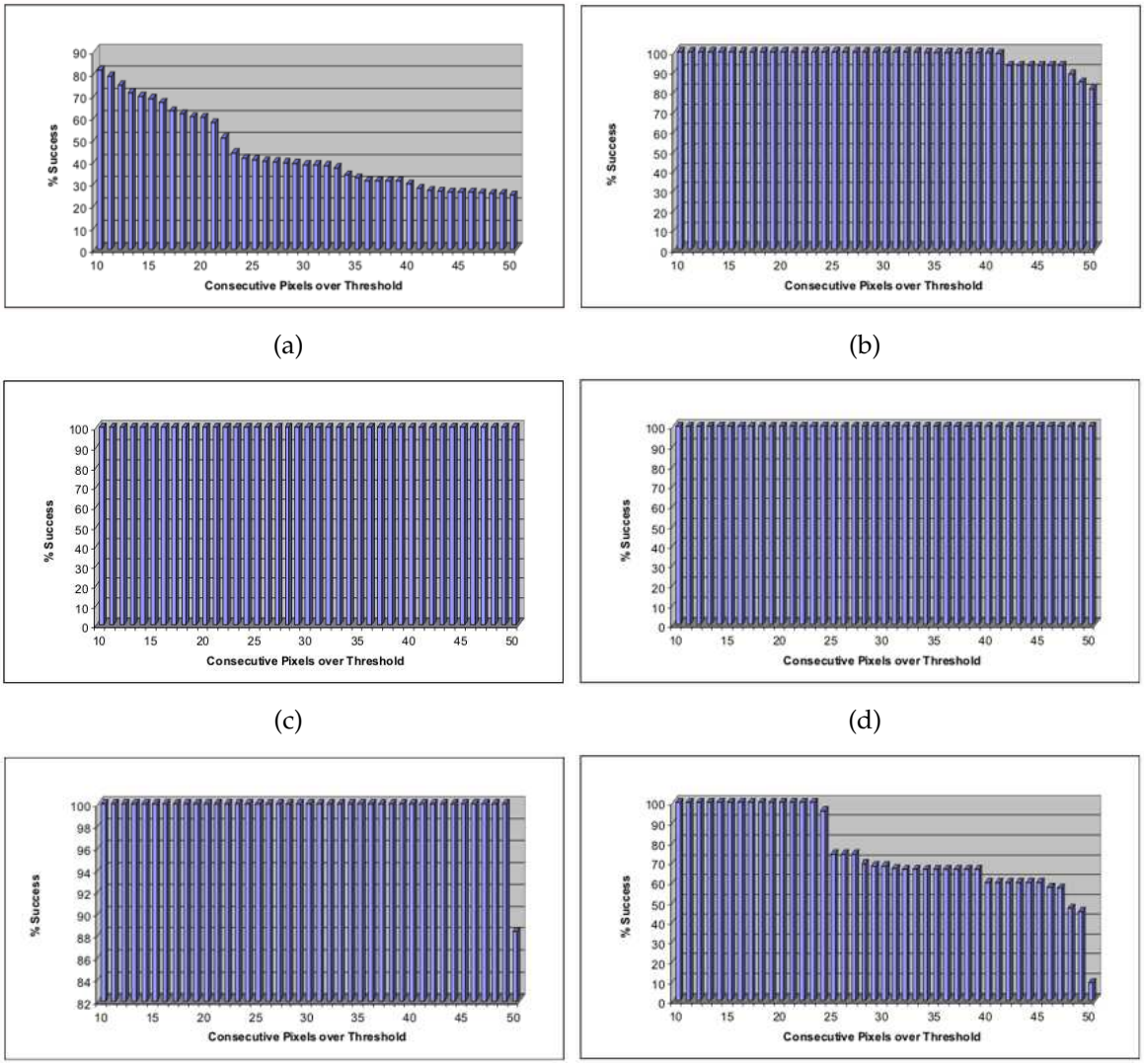

Figure 8.14: *Results of statistical analysis on "String + CMB" data for different values of S/N ratio: a) S/N=0.002; b) S/N=0.01; c) S/N=0.02; d) S/N=0.03; e) S/N=0.04; f) S/N=0.06*

($[0.01, 0.04]$), reaching the maximum in $[0.02, 0.03]$. About its cleanliness, we see that there is a $\sim 21\%$ to have false positives if the string is not present, but in case of presence of string, there are no spurious events setting $n = 50$.

8.5.2 Jump Filter analysis

Also in this case, the main purpose of statistical analysis on the Jump Filter is the determination of its efficiency and cleanliness with the two different thresholds (in the following, the filter will be called $F1$ or $F2$ according with the threshold used (Σ_1 or Σ_2

S/N	Best consec. pixels	Best Efficiency	Efficiency at 50 pixels
0.002	10	0.813	0.247
0.01	10 ÷ 33	1.000	0.810
0.02	10 ÷ 50	1.000	1.000
0.03	10 ÷ 50	1.000	1.000
0.04	10 ÷ 49	1.000	0.883
0.06	10 ÷ 23	1.000	0.009

Table 8.3: *Results of statistical analysis on "String + CMB" data for different S/N ratios*

S/N	Total Cleanliness	Cleanliness at 50 pixels
0.002	0.195	1.000
0.01	0.376	1.000
0.02	0.504	1.000
0.03	0.472	1.000
0.04	0.334	1.000
0.06	0.241	1.000

Table 8.4: *Ratio of spurious events detected in "String + CMB" maps for different S/N ratios*

respectively) by setting the optimal values of its parameters γ and l. In order to evaluate the best filter configuration, the analysis was performed by varying, on both types of maps, the value of parameter γ and l, in according to the values of Tab. 8.5.

γ
1.5
2.0
2.5
3.0

l
5
10
15
20
25
30

Table 8.5: *Jump Trigger parameters γ (left side) and l (right side) used in statistical analysis*

In Tab. 8.6 and Fig. 8.15, the efficiency E_{jump} of $F1$ and $F2$ on "String + CMB" maps as function of the parameter α (and then of S/N ratio, according to Tab. 8.2) is shown.

It is clear that the filter works very well for $\alpha \geq 10$. Fixing α at its minimum value $\alpha = 10$, the best results of E_{jump} are obtained for all values of γ except $\gamma = 3.0$, as shown

α	$F1$ **efficiency**	$F2$ **efficiency**
1	0.000	0.007
5	0.489	0.620
10	0.980	0.999
15	1.000	1.000
20	1.000	1.000
30	1.000	1.000

Table 8.6: *Jump Filter efficiency as function of parameter α (then of S/N ratio) on "String + CMB" maps. Both filters $F1$ and $F2$ work very well for $\alpha \geq 10$*

.

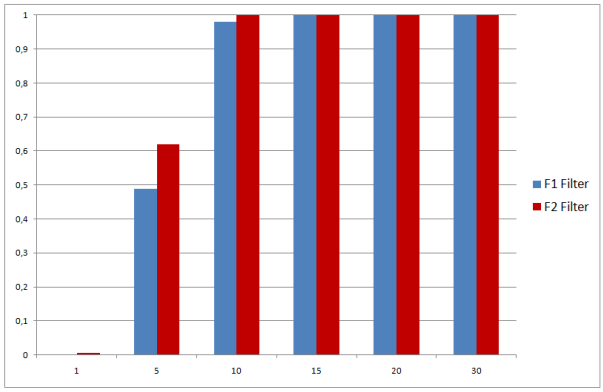

Figure 8.15: *Jump Filter efficiency as function of parameter α on "String + CMB" maps.*

in Tab. 8.7.

If we evaluate the efficiency of $F1$ and $F2$ as function of γ, regardless of the value given to α, the slow-descreasing tendency is confirmed, allowing to exclude $\gamma = 3.0$. Then, excluded this value of γ, the "only CMB" maps have been explored, in order to evaluate the cleanliness of the two filters, selecting only data with at least one value of cleanliness equal to 1 (i.e. with no spurious data detected). Results are shown in Tab. 8.8.

γ	$F1$ **efficiency**	$F2$ **efficiency**
1.5	1.000	1.000
2.0	1.000	1.000
2.5	1.000	1.000
3.0	0.921	0.996

Table 8.7: *Jump Filter efficiency as function of parameter γ on "String + CMB" maps, setting $\alpha = 10$. Both filters $F1$ and $F2$ work perfectly for $\gamma < 30$.*

The best combinations of parameters γ and width l are the pairs $(2.5, 15)$ and $(2.5, 20)$

γ	l	$F1$ **efficiency**	$F2$ **efficiency**
1.5	5	1.000	0.000
2.0	5	1.000	0.0053
2.0	30	0.157	1.000
2.5	5	1.000	0.813
2.5	10	1.000	0.867
2.5	15	1.000	1.000
2.5	20	1.000	1.000
2.5	25	0.963	1.000
2.5	30	0.880	1.000

Table 8.8: *Cleanliness of Jump Filter on "only CMB" maps for selected pairs of parameters* (γ, l). *Data are selected if at least one of the filters has efficiency equal to 1. The best combinations are* $(2.5, 15)$ *and* $(2.5, 20)$

for which both filters has cleanliness $C_{jump} = 1.000$. In particular, the pair $(2.5, 20)$ has a better efficiency ($E_1 = 0.563$, $E_2 = 0.593$) than $(2.5, 15)$ for $\alpha = 5$.

8.6 The Jump Filter on the real WMAP data

The excellent results of the Jump Trigger on a large number of simulations prompted to its application on real data from WMAP mission. At this purpose, the filter was been applied to a ILC map of the WMAP 5-years data release. The Internal Linear Combination (ILC) map is formed from a weighted linear combination of 5 Smoothed I Maps in which the weights are chosen in order to maintain the CMB anisotropy signal while minimizing the Galactic foreground contribution.

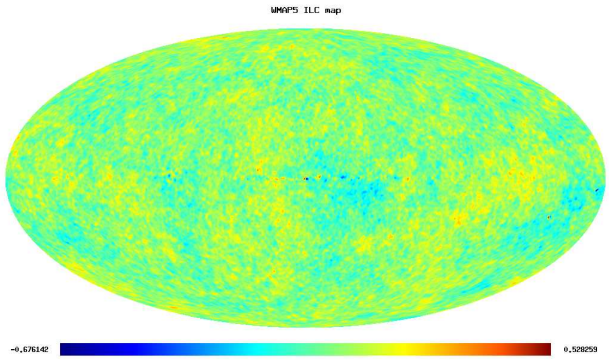

Figure 8.16: *The ILC map of WMAP 5-years data release. The map has a resolution parameter* $N_{side} = 512$, *for a total of 3145728 pixels and a resulting resolution of* 1°.

The weights were determined by minimizing the variance of the measured tempera-

tures with the additional constraint that sum of the weights is equal to 1. To account for the spatial variation of the spectral indices of the various foreground components across the sky and in particular in the Galactic plane, the sky is divided into 12 regions: 11 regions within the Galactic plane and 1 covering the outer Galactic plane and high Galactic latitudes. The weights are calculated for each of the 12 regions and a full-sky ILC map is generated using the obtained coefficients after smoothing the region boundardies with a 1.5 degree kernel. As a final step, a 'bias' correction' based on Monte Carlo simulations is applied to to the ILC map. The map, initially ordered according to a NESTED scheme, has a resolution parameter $N_{side} = 512$, for a total of $N_{pix} = 3145728$ pixels and a resulting resolution of 1° (Fig. 8.16). Temperature assumes values in [-0.729654 mK, 0.530705 mK].

The map produced by the squeezing procedure on the ILC map is depicted in Fig. 8.17.

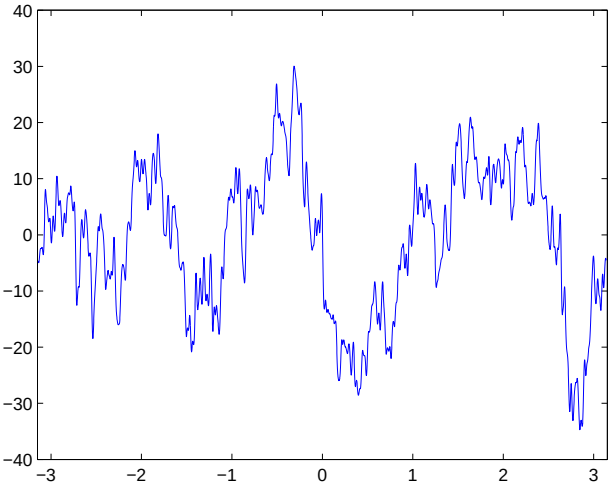

Figure 8.17: *The squeezed map produced by the squeezing procedure on the WMAP5 ILC map.*

The Jump Filter was applied on the squeezed ILC map using the same pairs of parameters γ and l used in the statistical analysis for the cleanliness determination (Tab. 8.8), thus including the case with the optimal parameters, $(2.5, 15)$ and $(2.5, 20)$. The results are shown in Tab. 8.9 in which, in F1 and F2 columns, corresponding to the two different thresholds defined in 8.4.3, are flagged with 1 and 0 the cases of detected or not detected event respectively.

Comparing these results with those in Tab. 8.8, relative to the cleanliness, it appears clear that the first two, corresponding to the pairs $(1.5, 5)$ and $(2.0, 5)$, are spurious events, because the efficiency of F1 with those parameters is extremely low. Conversely, the detected event for the pair $(2.5, 5)$ needs more attention: probably it is a spurious

γ	l	$F1$ **detection**	$F2$ **detection**
1.5	5	0	1
2.0	5	0	1
2.0	30	0	0
2.5	5	0	1
2.5	10	0	0
2.5	15	0	0
2.5	20	0	0
2.5	25	0	0
2.5	30	0	0

Table 8.9: *Results of application of Jump Filter on WMAP ILC map for different choice of the parameters γ and l. In F1 and F2 columns, corresponding to the 2 different thresholds, are flagged with 1 and 0 the cases of detected or not detected event respectively.*

event too, because the same filter with the optimal parameters has given no detection, but the fact that the cleanliness for this pair is high (0.813), suggests that this event has to be more investigated.

Even if it will be confirmed that the event under investigation is spurious, the performed analysis could give anyway an important result about cosmic strings. In fact, if such result will be also confirmed for different inclinations of the cosmic string respect with the observer (remember that this analysis has been performed on a vertical straight string only), it is possible to set an upper limit to the deficit angle (and then on the parameter $G\mu$), according to the following formula that relates the deficit angle to the amplitude of the temperature anisotropy induced by a string:

$$\delta T = 27 \mu K \frac{\Delta}{2"} \frac{\beta}{0.9} F, \tag{8.9}$$

where β is velocity of the string in units of speed of light and F is a function which define angular structure of the anisotropy and is equal to unity at the string front. The Jump Filter has the best efficiency up to $\alpha = 15$ (see Tab. 8.6), corresponding to a S/N ratio of 0.03 (referring to Tab. 8.2); then, taking into account the maximum value of temperature of the map and using eq. 8.9, one obtains

$$\Delta \lesssim 1'',$$

which corresponds to linear density of GUT energy scale [86].

Chapter 9

Summary and conclusions

Cosmic strings are expected to produce well defined and unambiguous observational features. In optical surveys these features are of two types: chains of lensed galaxies and sharp edges in well resolved galactic images. In the CMBR, cosmic strings introduce well defined step-like discontinuities. This thesis can be considered as an exploratory work aimed at defining the best strategy to detect cosmic string signatures in both types of data. As it has been outlined and justified in the previous chapters, the most effective approach to the search for cosmic string is first to search for CMBR signatures and then to perform optical follow-up's and validation. In order to have a cross-match between radio and optical data, among all detected string candidates one has to choose strings with angular size more than 100° to be sure that they are inside the sphere of optical sources $z < 7$.

From the optical point of view, the search of sources lensed by a cosmic string is made very difficult by the presence of a lot of spurious effects, mainly when the flux is low. If one performs a research in the SDSS catalogues for possible candidate lensed objects, their number is so large to hinder any possible signal. In order to reduce the spurious candidate components, it is necessary to work on very accurate photometric data and, if possible in the 3-D space, rather than in the 2-D (projected) space. To this purpose, I started to work on the determination of photometric redshifts of galaxies and QSOs, by using an innovative method based on multiwavelength photometry and on a combination of data mining techniques. This procedure makes use of specific tools developed under the EuroVO and NVO frameworks for data gathering, preprocessing and mining, while relying on the scaling capabilities of the computing grid. This method allowed us to obtain photometric redshifts with an increased accuracy (up to 30%) with respect to the literature. The application of these new redshift to the search for candidate lensed pairs will be addressed in a future work.

The main part of my work regarded the study of the possibility to detect the Cosmic String signatures expected in the CMBR. The anisotropy induced by a cosmic string would appear in the CMB as a well defined and peculiar sequence of zones of decreased and increased temperature: first a cold spot in front of the moving string, then a step-like jump followed by an hot spot and, finally, a second cold spot. The structure of such temperature fluctuations is virtually independent on the cosmic string parameters, since

only the spot width and the temperatures at the local maximum and local minima are affected by the position of the string with respect to the observer, by the string velocity and direction, and by the string linear density. But the structure always remains the same.

In the simplifying assumption that the string is a straight discontinuity in space time, I used the S.Co.P.E. computational grid to produce a large number of simulations covering a wide range of values for the velocity of the string, its direction and its distance from the observer. Simulations were produced using a C++ code with the Healpix pixelization. This code generated realistic maps of the CMB temperature distribution in presence of a straight cosmic string. By varying its characteristic parameters, it is possible to explore the signatures left by various types of moving strings. These simulations can be divided in two types: without string, simulating the signal and noise structure of WMAP data and without noise–with string; the two types of data were then combined to produce realistic simulated images sampling the whole parameter space defined by S/N and string parameters. Maps were subject to a "squeezing" procedure in order to amplify the step-like discontinuity and smooth the noise. The first step of the squeezing procedure is the partition of the sphere (then of the HEALPix map) in strips of $\Delta\theta = 10^\circ$, centered on the equator. In each strip, for fixed longitude ϕ, the average $\delta\overline{T}$ of the anisotropy values over the latitude θ is calculated, so that the map is reduced to a monodimensional vector of 4096 pairs $(\phi, \delta\overline{T}(\phi))$. Finally all strips are summed together.

Successively, on the "squeezed" maps, I tested some filters: the first, the Threshold Filter, searches for all pixels which are over a pre-defined threshold. Statistical analysis over 2100 simulations demonstrates that, even if its capability of recognizing the string is good, the spurious component is too high to assure good overall results. The second kind of filter, the Jump Filter, recognizes high value differences between close pixels. In this case, the statistical analysis shows a great efficiency of the filter for values of S/N ratio greater or equal than 2%, with an extremely low spurious component.

The excellent results of the Jump Filter on simulations allowed its application on the WMAP data. With the best choice of parameters (defined by the statistical analysis), there are no detected event, but the filter has detected 3 events with other parameters: two of them are surely spurious, while the third, corresponding to a non optimal but equally good pair of parameter, deserves further nvestigations.

This work foresees many possible developments: first of all, the detected event has to be investigated, both by other CMB data analysis tecniques and by cross-matching with optical data. About CMB data analysis, we are exploring the possibility of using adpative filtering or *ad hoc* data structures (like, for example, b-trees) in order to seek and follow the path of the step-like signature, regarless of the shape and the direction of the string. About optical data analysis, the work has to follow two directions: the re-

search of the ”milky ways” of lensed object and the cross-matching between optical and CMB candidates. Recently, for example, Morgason et al. [57] has found four possible lensed candidates: our aim is to search for these candidates in CMB data the possible correspondence to such candidates. In fact, finding signature both in CMB data and a correspondence in optical data would be the definitive proof for the existence of cosmic string.

Appendix A

Appendix

A.1 Multi-Layer Perceptron (MLP)

A.1.1 General remarks

Neural networks may have different architectures and topologies, but in the following we shall always refer to feed-forward networks only.

Feed-forward neural networks provide a general framework for representing non linear functional mappings between a set of input variables and a set of output variables. We can achieve this goal by representing the non linear function of many variables by a composition of non-linear *activation* functions of one variable.

A multi-layer perceptron may be represented by a graph, as shown in figure A.1: the input layer is made of a number of perceptrons equal to the number of input variables; the output layer, on the other hand, will have as many neurons as the output variables.

The network may have an arbitrary number of hidden layers which in turn may have an arbitrary number of perceptrons.

In a fully connected feed-forward network each node of a layer is connected to all

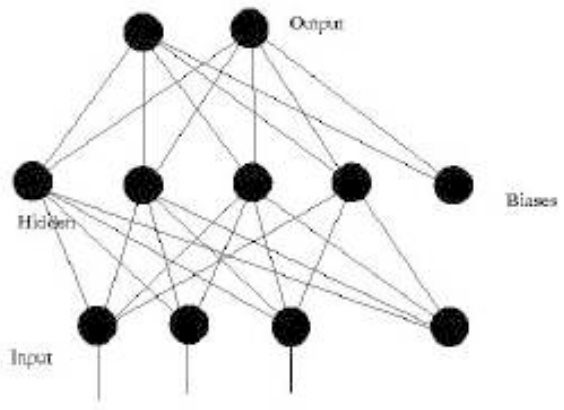

Figure A.1: *The Multi-Layer Perceptron*

the nodes in the adjacent layers[1]. Input layer's nodes are, obviously, connected to the first layer's node only, and output nodes are likewise connected only to the last hidden layer's neurons only.

Each connection is represented by an adaptive *weight* which represents the *stength* of the synaptic connection between neurons.

Generally speaking, along with the regular units, a feed-forward network presents a *bias* parameter for each layer. The bias parameter of the kth layer is added to the activation function input of all the nodes in the $k+1$th layer.

In figure A.1 a network with a single hidden layer is shown in its schematic representation.

We will now consider a generic feed-forward network with d input units, c output units and M hidden units in a single hidden layer. We shall refer to this kind of network as a two-layer network, counting the number of connection layers instead of the number of perceptron layers.

The input units are special, in the sense that their value is equal to the input value passed to the network. No other manipulation is required to these units.

The output of the jth hidden unit of the kth hidden layer is formed by firstly computing the weighted sum of the inputs:

$$a_j^{(k)} = \sum_{i=0}^{d} w_{ji}^{(k)} z_i^{(k-1)},$$

where $w_{ji}^{(k)}$ denotes the weight related to the connection from the $k-1$th layer to the jth node of the kth layer, and z_i is the activation state of the unit. Notice that the sum runs from 0 to d, and that we have included the bias parameter in the $k-1$th units as $w_{j0}^{(k-1)} = b_{k-1}$, with a constant activation state $z_0^{(k-1)} = 1$.

Then, the output of the jth unit of the kth layer is

$$z_j^{(k)} = g\left(a_j^{(k)}\right),$$

where $g()$ is the activation function. It's worth stressing that, in general, different nodes may have different activation functions, even in the same layer. Actually, most of the times we set one activation function for the hidden layers and one for the output one.

Once combining all these functions through the network, we obtain the outputs. For the kth output unit we have:

$$y_k = \tilde{g}\left(\sum_{j=0}^{M} w_{kj}^{(2)} g\left(\sum_{i=0}^{d} w_{ji}^{(1)} x_i\right)\right).$$

[1]This kind of networks are referred to as fully connected networks. However, generally speaking, we could also have missing connections. These networks are called *sparse* networks and are characterized by another parameter, the connection rate.

If the output activation function is linear ($\tilde{g}(a) = a$) the network output simply reduces to:

$$y_k = \sum_{j=0}^{M} w_{kj}^{(2)} g\left(\sum_{i=0}^{d} w_{ji}^{(1)} x_i\right).$$

It's worth stressing that in a feed-forward network the outputs can be expressed as deterministic functions of the inputs.

A.1.2 Activation functions

One of the most used differentiable activation functions, that can be used to represent smooth mappings between continuous variables, is the logistic sigmoid function:

$$g(a) \equiv \frac{1}{1 + e^{-a}}.$$

The function is defined in the interval $(-1, 1)$ and present a linear central region. For regression problems, it is often use for hidden units, and this is actually what we do in our method[2]. However, the use of the logistic function requires the features to be normalized between $(-1, 1)$.

The linear activation function $g(a) = a$ is used when dealing with regression problems for the output units. In this way, the target vectors don't need to be normalized. We actually use the linear activation function for our networks' output nodes.

A.1.3 Back Propagation (BP)

In the previous sections we have introduced feed-forward neural networks and their function approximation capabilities. But in order to take advantage of them we need to solve the following approximation problem: given a network topology we need to find the values of the weights that best fit the data.

This task is referred to as *training*, since the network actually *learns* how to adapt its structure to the data.

We can distinguish among three learning classes:

Supervised learning. We provide the network with a set of examples for the network itself to learn from. This *a priori* information is made of a set of patterns that we call base of knowledge (BoK).

[2]We actually use a *faster* sigmoidal function instead of the "pure" logistic one, so to speed up the training procedure.

Unsupervised learning. The network trains itself to adapt its synaptic weights on the base of data intrinsic statistic properties only. No *a priori* information is provided to the network.

Reinforcement learning. In these learning paradigm no BoK is seeded to the network. Instead, the system learns by interacting with the *environment* which actually produces *observations*.

Throughout this work we will make use of supervised learning. The description of the BoKs used in this work is provided in section 7.2.

The BoK is constituted by a set of pairs $(\mathbf{x_i}, \mathbf{d_i})$, where $\mathbf{x_i} \in X$ are the so called *input* vectors, or input *patterns*, while $\mathbf{d_i} \in Y$ are called *target* vectors (patterns). Input vectors' components are called *features*.

Learning is an optimization task in which we seek out the model (i.e. the synaptic weigths) that best fit our data, while keeping a good generalization capability. This task involves some sort of error function minimization. This function is often referred to as *cost* function, and we will always assume a sum of squares error function, even if any arbitrary cost function can be, in principle, considered.

The BP is a common algorithm for cost function minimization implemented, in its simplest form, as an iterative gradient descent of the cost function: at each learning iteration n the network response to an input pattern $\mathbf{x}(n)$ is $\mathbf{y}(n)$, while the desired output is $\mathbf{d}(n)$.

We can back propagate the error between the actual output and the desired one by calculating the derivative of the cost function with respect to the weigths[3] throughout the network: this way we can find the weights that minimize the cost function and update them.

A.1.4 Regression with MLP

Regression is the task of predicting the dependent variable $din\mathbb{R}^M$ from the input vector $\mathbf{x} \in \mathbb{R}^M$ consisting of M random variables.

The input data $\{(x_p|p = 1, 2, ..., P\}$ may be assumed to be selected independently with a probability density $P(x)$. Outputs $\{(d_p|p = 1, 2, ..., P\}$ are generated following the standard signal-plus-noise model

$$d_p = f(x_p) + \epsilon^p$$

where $\{\epsilon^p|p = 1, 2, ..., P\}$ are zero-mean random variables with probability density $P_\epsilon(\epsilon)$.

[3]This requires the error function to be differantiable.

A neural network's learning procedure aims to minimize a cost function. We will assume this function is the MSE

$$E_f = \sum_{p=1}^{P} (y_p - f(\mathbf{x_p}))^2$$

This way the "best" regressor is represented by $E(y|x) = \int yP(y|x)dy = f(x)$, where E denotes the expectation. Unbiased neural networks asymptotically ($P \to \infty$) converge to the regressor.

We can account for uncertainty in the independent variable assuming that we cannot sample any x directly: instead, what we sample is another random vector $\mathbf{z} \in \mathbb{R}^M$ defined by

$$z_p = x_p + \delta_p,$$

where δ_p are the independent random vectors sampled from the probability distribution $P_\delta(\delta)$.

A neural network trained with data $\{(z_p, y_p)|p = 1, 2, ..., P\}$ approximates

$$E(y|z) = \frac{1}{P(z)} \int yP(y|x)P(z|x)P(x)dydx = \frac{1}{P(z)} \int f(x)P_\delta(z - x)P(x)dx$$

This means that, in general, that $E(y|z) \neq f(z)$. The equality stands only when there is no noise.

If noise is assumed to be gaussian, it can be shown that, in some cases, $E(y|z)$ is the convolution of f with the noise process $P_\delta(z - x)$.

A.1.5 Errors in MLP predictions

Generally speaking, we can distinguish among four different noise sources:

- model variance (from both training and data);
- model bias (from both training and data);
- target noise;
- input noise.

We briefly explain the meaning of each:

Model Variance. Different sets of training data and different sets of initial weights will lead to different trainings and so to different predictions. According to the coverage of the parameter space, a network may show more or less variance in different

regions of the parameter space itself. Generally speaking, in a given region of the parameter space the training of a network may be more or less dependent on the data: if the training depends much on the data, because, for example, the data in a specific input space region are very sparse, then the network is said to have high variance from data, and vice versa. The same arguments stand for the dependance upon the initial choise of the weights: a network which depends much on the initial choice of the weigths is said to have high variance from training. In the latter case, the dependance is influenced not only by the coverage of the parameter space, but also by the complex nature of the cost function, that could lead the gradient descent to local minima. This variance could be filtered out by means of other optimization algorithms than back propagation, like genetic algorithms.

Model Bias. In some regions of the parameter space the network may fail to learn the conditional mean of the data, due to either the data or the training process. If the network topology is not complex enough, for example, then the network will fail to learn a mapping relation between inputs and targets; or, even if the network is complex enough, the training process may have been stopped too early.

Target Noise. In some cases and, again, in some regions of the parameter space, the input patterns may not be predictive of the target values, thus introducing the so called target noise. The uncertainty induced on the network prediction, unlike the previous ones, is irreducible. The target noise is, in fact, the conditional variance of the data, and is intrinsic to the data themselves.

Input Noise. Input patterns will suffer, in general, from some degree of intrinsic uncertainty: this uncertainty will propagate through the network as uncertainty on the prediction.

These uncertainty sources implicitly assume that we provide the network with all the information it needs in order to learn how to approximate the mapping function from the parameter space to the target space. In other words, we assume that there actually is a function, at least injective, from the parameter space to the target space, and that all the information we have is enough for the network to approximate this function, but with some uncertainty to be determined.

However, this is not the case for photometric redshift estimation, since, as we will show in the following sections, we have to deal with some degeneracy in the data. We will assume that this degeneracy is due to some missing data, i.e. to some features we can't measure. This fact can be justified with physical arguments.

From a physical point of view, the degeneracy is, as a matter of fact, due to the spectroscopic features shifting off the photometric system, leading to photometric points

that appear to be near in the parameter space but would be far away from each other in a parameter space with more dimensions, and at different redshifts.

In fact, if we could access observations of the same sources from other photometric systems, i.e. from other surveys, we could remove at least part of the degeneracy, since the spectroscopic signature of the redshift would become accessible. This is the reason why a multiwavelength approach to the photometric redshift problem is so appealing.

In the following discussion we will assume that the model bias is negligible, since we can assume that our network is complex enough to learn the conditional mean of the data, wherever it's possible, i.e. within those regions of the parameter space that don't show any degeneracy; we also assume that the training process is not stopped too early, by means of a validation procedure.

Despite the intrinsic deficiency of our data, in the following sections we shall try to estimate the error contributions from target noise, input noise and model variance and, when possible, to filter them out.

A.2 k-means clustering

In distance-based clustering the criterion is just the "distance" and its definition: two or more objects belong to the same cluster if they are "close" according to a given distance. The goal of clustering is to determine the intrinsic grouping in a set of unlabeled data. But how to decide what constitutes a good clustering? It can be shown that there is no absolute *best* criterion which would be independent of the final aim of the clustering. Although different figures are commonly used, it is the user which must supply this criterion, in such a way that the result of the clustering will suit his needs.

For instance, we could be interested in finding representatives for homogeneous groups (data reduction) or in finding unusual data objects (outlier detection).

k-means is one of the simplest, yet robust, clustering algorithms: given the number of clusters (k), k-means finds the k cluster centroids. If the distance is chosen to be the euclidean distance between points, a point belongs to the cluster with the nearest centroid.

The best centroids are found by an iterative procedure.

At first, k centroids are placed randomly in the parameter space, even if one should be careful in placing them as far as possible from each other.

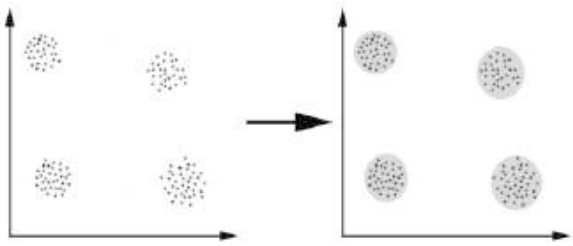

Figure A.2: *A simple clustering example in two dimensions.*

Clustering is an unsupervised learning task: its goal is to find a structure in a collection of unlabeled data. In other words clustering is the process of organizing objects into groups whose members are similar in some way; moreover, a good clustering requires that objects in different clusters are dissimilar assording to the same similarity definition.

Then:

1. each point in the dataset is associated with the nearest centroid;
2. the k centroids positions are recalculated so to be the barycenters of the clustering resulting from the previous step.

The loop between points 1. and 2. is repeated until convergence is found, i.e. when the centroids don't "move" anymore, or when the maximum number of iterations has been reached.

From this step on, the algorithm tries to minimize the *objective* function:

$$J = \sum_{j=1}^{k} \sum_{i=1}^{n} d(x_i^{(j)} - c_j) \ ,$$

where d is the chosen distance. Euclidean distance is often used, and that was our choice, too.

Bibliography

[1] T.W.B. Kibble. Topology of cosmic domains and strings. *J.Phys. A: Math. Gen. V.9*, 1976.

[2] Ya.B. Zeldovich. Cosmological fluctuations produced near a singularity. *Mon. Not. Royal Astr. Soc.*, 192:663, 1980.

[3] A. Vilenkin. Gravitational field of vacuum domain walls and strings. *Phys. Rev. D*, 23(4):852, 1981.

[4] A. Vilenkin and E.P. Shellard. *Cosmic strings and other topological defects*. Cambridge Univ. Press., 1994.

[5] A.C. Davis and T.W.B. Kibble. Fundamental cosmic strings. *Contemporary Physics*, 46:313, 2005.

[6] J. Polchinski and J.V. Rocha. Cosmic string structure at the gravitational radiation scale. *Phys. Rev. D*, 75(123503), 2007.

[7] `http://map.gsfc.nasa.gov/`.

[8] M.V. Sazhin, O. Khovanskaya, M. Capaccioli, G. Longo, J.M. Alcalá, R. Silvotti, and M. Pavlov. Search for gravitational lenses near the extragalactic double object csl-1. *Astronomy Letters*, 31(2):73–79, 2005. astro-ph/0406516.

[9] J.L. Christiansen, E. Albin, K.A. James, J. Goldman, D. Maruyama, and G.F. Smoot. Search for cosmic strings in the great observatories origins deep survey. *Phys. Rev. D*, 77(123509), 2008.

[10] M.V. Sazhin, O. Khovanskaya, M. Capaccioli, G. Longo, M. Paolillo, G. Covone, N.A. Grogin, and E.J. Schreier. Gravitational lensing by cosmic string: what we learn from the csl-1 case. *Mon. Not. Royal Astr. Soc.*, 376:1731–1739, 2007. astro-ph/0611744.

[11] M.A. Gasparini, P. Marshall, T. Treu, E. Morgason, and F. Dubath. Direct observation of cosmic strings via their strong gravitational lensing effect: I. predictions for high resolution imaging surveys. *MNRAS*, 385:1959–1964, 2007.

[12] M.V. Sazhin, G. Longo, M. Capaccioli, J.M. Alcalá, R. Silvotti, G. Covone, O. Khovanskaya, M. Pavlov, M. Pannella, M. Radovich, and V. Testa. Csl-1: chance projection effect or serendipitous discovery of a gravitational lens induced by a cosmic string? *Mon. Not. Royal Astr. Soc.*, 343:353–359, 2003. astro-ph/0302547.

[13] M.V. Sazhin, M. Capaccioli, G. Longo, M. Paolillo, O. Khovanskaya, N.A. Grogin, E.J. Schreier, and G. Covone. The true nature of csl-1. astro-ph/0601494, 2006.

[14] E. Agol, C.J. Hogan, and R.M. Plotkin. Hubble imaging excludes cosmic string lens. *Phys. Rev. D*, 73(087302), 2006.

[15] N. Kaiser and A. Stebbins. Microwave anisotropy due to cosmic strings. *Nature*, 310:391, 1984.

[16] M.B. Hindmarsh. *The Formation and evolution of cosmic strings*, chapter Seaching for Cosmic Strings, page 527. Cambridge Univ. Press, 1990.

[17] E. Jeong and G.F. Smoot. The validity of the cosmic string pattern search with the cosmic microwave background. *ApJL*, 661, 2007.

[18] O. Laurino. Deprojecting the agn universe within the virtual observatory. Master's thesis, University of Naples "Federico II", 2009.

[19] R.C. Tolman. *Relativity, Thermodynamics, and Cosmology*. Oxford: Clarendon Press, 1934. LCCN 340-32023. Reissued (1987) New York: Dover ISBN 0-486-65383-8.

[20] R.A. Alpher and R.C. Herman. On the relative abundance of the elements. *Phys. Rev.*, 74:1737 – 1742, 1948.

[21] A. McKellar. Evidence for the molecular origin of some hitherto unidentified interstellar lines. *PASP*, 52(307):187, 1940.

[22] W.S. Adams. What lies between the stars. *PASP*, 53(312):73, 1941.

[23] J.F. Denisse, E. Le Roux, and J.C. Steinberg. *Comptes Rendus de lAcademie des Sciences*, 244, 1957. (in French).

[24] A.G. Doroshkevich and I.D. Novikov. *Sov. Phys. Dokl.*, 9:111, 1964.

[25] G.F. Smoot, C.L. Bennett, A. Kogut, E.L. Wright, J. Aymon, and N.W. Boggess. Structure in the cobe differential microwave radiometer first-year maps. *ApJ*, 396(L1), 1992.

[26] J.M. Kovac, E.M. Leitch, C. Pryke, J.E. Carlstrom, N.W. Halverson, and W.L. Holzapfel. *Nature*, 420:772, 2002.

[27] http://cmb.phys.cwru.edu/boomerang/.

[28] http://www.rssd.esa.int/index.php?project=planck.

[29] http://cosmology.berkeley.edu/group/swlh/acbar/.

[30] http://www.archeops.org/.

[31] http://pole.uchicago.edu/.

[32] http://en.wikipedia.org/wiki/Clover_(telescope).

[33] http://quiet.uchicago.edu/site/index.html.

[34] http://lambda.gsfc.nasa.gov/product/cobe/firas_overview.cfm.

[35] D.J. Fixsen, E.S. Cheng, D.A. Cottingham, R.E. Eplee, Jr, R.B. Isaacman, J.C. Mather, S.S. Meyer, P.D. Noerdlinger, R.A. Shafer, R. Weiss, R.L. White, C.L. Bennett, N.W. Boggess, T. Kelsall, S.H. Moseley, R.F. Silverberg, G.F. Smoot, and D.T. Wilkinson. Cosmic microwave background dipole spectrum measured by the cobe firas instrument. *AJ*, 420:445449, 1994. doi:10.1086/173575.

[36] A.H. Guth. Inflationary universe: A possible solution to the horizon and flatness problems. *Phys. Rev. D*, 23(2):347–356, 1981.

[37] T.W.B. Kibble. Some implications of a cosmological phase transition. *Phys. Rept.*, 67:183, 1980.

[38] P. Brax, C. van de Bruck, and A.C. Davis. Brane world cosmology. *Rept.Prog.Phys.*, 67:2183–2232, 2004. hep-th/0404011v1.

[39] S. Sarangi and S.H.H. Tye. Cosmic string production towards the end of brane inflation. *Phys. Lett. B.*, 536:185, 2002. hep-th/0204074.

[40] N.T. Jones, , H. Stoica, and S.H.H. Tye. The production, spectrum and evolution of cosmic strings in brane inflation. *Phys. Lett. B.*, 563(1-2):6–14, 2003. hep-th/0303269.

[41] E.J. Copeland, R.C. Meyers, and J. Polchinski. Cosmic f- and d-strings. *JHEP*, 0406(013), 2004. hep-th/0312067.

[42] J. Polchinski. hep-th/0412244.

[43] T. Goto. Relativistic quantum mechanics of one-dimensional mechanical continuum and subsidiary condition of dual resonance model. *Prog. Theor. Phys.*, 46(5):1560–1569, 1971.

[44] Y. Nambu, 1970. lectures given at the Copenhagen Summer School.

[45] A. Vilenkin. Cosmic string dynamics with friction. *Phys. Rev. D*, 43(4):1060–1062, 1991.

[46] J. Garriga and M. Sakellariadou. Effects of friction on cosmic strings. *Phys. Rev. D*, 48:2502–2515, 1993.

[47] D. Austin, E.J. Copeland, and T.W.B. Kibble. Evolution of cosmic string configurations. *Phys. Rev. D*, 48(5594), 1993.

[48] J.M. Alcalá, M. Pannella, E. Puddu, M. Radovich, R. Silvotti, A. Arnaboldi, M. Capaccioli, G. Covone, M. Dall'Ora, A. Grado, G. De Lucia, G. Longo, A. Mercurio, I. Musella, N. Napolitano, M. Pavlov, A. Rifatto, V. Ripepi, and R. Scaramella. The capodimonte deep field i - presentation of the survey and first follow-up studies. *Astron. and Astrophys.*, 428:339–352, 2004.

[49] M.V. Sazhin, M. Capaccioli, G. Longo, M. Paolillo, and O. Khovanskaya. Further spectroscopic observations of the csl-1 object. *Ap. J. Lett.*, 636:L5–L8, 2006. astro-ph/0506400.

[50] J.R. Gott. Gravitational lensing effects of vacuum strings - exact solutions. *The Astrophysical Journal*, 288:422, 1985.

[51] T. Vachaspati. Gravitational effects of cosmic strings. *Nucl. Phys.*, B(277):593, 1986.

[52] A. Vilenkin. Looking for cosmic strings. *Nature*, 322:14, 1986.

[53] D.R. Stinebring, M.F. Ryba, J.H. Taylor, and R.W. Romani. The cosmic gravitational wave background: Limits from millisecond pulsar timing. *Phys. Rev. Lett.*, 65:285, 1990.

[54] P. Bhattacharjee. Cosmic strings and ultrahigh-energy cosmic rays. *Phys. Rev. D*, 40(3968), 1989.

[55] A.D. Sakharov. Cp symmetry violation, c-asymmetry and baryonic asymmetry of the universe. *Pisma Zh. Eksp. Teor. Fiz.*, 5:32, 1967.

[56] S. Weinberg. Baryon- and lepton-nonconserving processes. *Phys. Rev. Lett.*, 43:1566–1570, 1979.

[57] E. Morgason, P. Marshall, T. Treu, T. Schrabback, and R.D. Blandford. Direct observation of cosmic strings via their strong gravitational lensing effect: Ii. results from hst/acs image archive. arXiv: astro-ph/0908.0602, 2009.

[58] V. Vanchurin, K. Olum, and A. Vilenkin. Cosmic string scaling in flat space. *Phys. Rev. D*, 72, 2005. 063514.

[59] M. Fukugita, T. Ichikawa, J.E. Gunn, M. Doi, K. Shimasaku, and D.P. Schneider. The sloan digital sky survey photometric system. *AJ*, 111:1748, 1996.

[60] K. Abazajian and f.t. Sloan Digital Sky Survey. The seventh data release of the sloan digital sky survey. *ArXiv e-prints*, 2008.

[61] J.K. Adelman-McCarthy and f.t. Sloan Digital Sky Survey. The sixth data release of the sloan digital sky survey. *ApJS*, 175:297–313, 2008.

[62] T. Budavári, S. Heinis, A.S. Szalay, M. Nieto-Santisteban, J. Gupchup, B. Shiao, M. Smith, R. Chang, J. Kauffmann, P. Morrissey, D. Schiminovich, B. Milliard, T.K. Wyder, D.C. Martin, T.A. Barlow, M. Seibert, K. Forster, L. Bianchi, J. Donas, P.G. Friedman, T.M. Heckman, Y.-W. Lee, B.F. Madore, S.G. Neff, R.M. Rich, and B.Y. Welsh. Galex-sdss catalogs for statistical studies. *ApJ*, 694:1281–1292, 2009.

[63] X. Fan, M.A. Strauss, D.P. Schneider, J.E. Gunn, R.H. Lupton, R.H. Becker, M. Davis, J.A. Newman, G.T. Richards, R.L. White, J.E. Anderson, Jr, J. Annis, N.A. Bahcall, R.J. Brunner, I. Csabai, G.S. Hennessy, R.B. Hindsley, M. Fukugita, P.Z. Kunszt, Ž Ivezić, G.R. Knapp, T.A. McKay, J.A. Munn, J.R. Pier, A.S. Szalay, and D.G. York. High- redshift quasars found in sloan digital sky survey commissioning data. iv. luminosity function from the fall equatorial stripe sample. *AJ*, 121:54–65, 2001.

[64] G.T. Richards, X. Fan, H.J. Newberg, M.A. Strauss, D.E. Vanden Berk, D.P. Schneider, B. Yanny, A. Boucher, S. Burles, J.A. Frieman, J.E. Gunn, P.B. Hall, Ž Ivezić, S. Kent, J. Loveday, R.H. Lupton, C.M. Rockosi, D.J. Schlegel, C. Stoughton, M. SubbaRao, and D.G. York. Spectroscopic target selection in the sloan digital sky survey: The quasar sample. *AJ*, 123:2945–2975, 2002.

[65] R. D'Abrusco, A. Staiano, G. Longo, M. Brescia, M. Paolillo, E. De Filippis, and R. Tagliaferri. Mining the sdss archive. i. photometric redshifts in the nearby universe. *ApJ*, 663:752–764, 2007.

[66] A. Krogh and J. Vedelsby. *Neural network ensembles, cross validation, and active learning*, pages 231–238. MIT Press, 1995.

[67] N. Ueda and R. Nakano. *Neural Networks*, chapter Generalization error of ensemble estimators, pages 90–95. IEEE, 1996.

[68] B. Rosen. Ensemble learning using decorrelated neural networks. *Connection Science*, 8:373–384, 1996.

[69] C.M. Bishop. *Neural Networks for Pattern Recognition*. Oxford University Press, Inc., 1995. ISBN 0198538642.

[70] A.S. Weigend, M. Mangeas, and A.N. Srivastava. Nonlinear gated experts for time series: Discovering regimes and avoiding over fitting. 1995.

[71] N.M. Ball, R.J. Brunner, A.D. Meyers, N.E. Strand, S.L. Alberts, and D. Tcheng. Robust machine learning applied to astronomical data sets. iii. probabilistic photometric redshifts for galaxies and quasars in the sdss and galex. *ApJ*, 683:12–21, 2008.

[72] A.J. Connolly, I. Csabai, A.S. Szalay, D.C. Koo, R.G. Kron, and J.A. Munn. Slicing through multicolor space: Galaxy redshifts from broadband photometry. *AJ*, 110:2655, 1995.

[73] M.A. Weinstein, G.T. Richards, D.P. Schneider, J.D. Younger, M.A. Strauss, P.B. Hall, T. Budavári, J.E. Gunn, D.G. York, and J. Brinkmann. An empirical algorithm for broadband photometric redshifts of quasars from the sloan digital sky survey. *ApJS*, 155:243–256, 2004.

[74] G.T. Richards, M.A. Weinstein, D.P. Schneider, X. Fan, M.A. Strauss, D.E. Vanden Berk, J. Annis, S. Burles, E.M. Laubacher, D.G. York, J.A. Frieman, D. Johnston, R. Scranton, J.E. Gunn, Ž Ivezić, R.C. Nichol, T. Budavári, I. Csabai, A.S. Szalay, A.J. Connolly, G.P. Szokoly, N.A. Bahcall, N. Benitez, J. Brinkmann, R.J. Brunner, M. Fukugita, P.B. Hall, G.S. Hennessy, G.R. Knapp, P.Z. Kunszt, D.Q. Lamb, J.A. Munn, H.J. Newberg, and C. Stoughton. Photometric redshifts of quasars. *AJ*, 122:1151–1162, 2001.

[75] G.T. Richards, A.D. Meyers, A.G. Gray, R.N. Riegel, R.C. Nichol, R.J. Brunner, A.S. Szalay, D.P. Schneider, and S.F. Anderson. Effcient photometric selection of quasars from the sloan digital sky survey. ii. ∼1,000,000 quasars from data release 6. *ApJS*, 180:67–83, 2009.

[76] N.M. Ball, R.J. Brunner, and A.D. Meyers. Robust machine learning applied to terascale astronomical datasets. ArXiv e-prints, 2007.

[77] W.D. Penny and S.J. Roberts. Neural network predictions with error bars. *IEEE Transactions on Neural Networks*, 1997.

[78] R. D'Abrusco, G. Longo, and N.A. Walton. Quasar candidates selection in the virtual observatory era. ArXiv e-prints, 2008.

[79] `http://healpix.jpl.nasa.gov/`.

[80] `http://www.cfa.harvard.edu/~mzaldarr/CMBFAST/cmbfast.html`.

[81] O.S. Sazhina, M.V. Sazhin, and V.N. Sementsov. Cosmic microwave background anisotropy induced by a moving straight cosmic string. *Journal of Experimental and Theoretical Physics*, 133(5):1005, 2008.

[82] `http://space.gsfc.nasa.gov/astro/cobe/skymapinfo.html`.

[83] U. Seljak and M. Zaldarriaga. A line-of-sight integration approach to cosmic microwave background anisotropies. *AJ*, 469:437–444, 1996.

[84] `http://www.thphys.uni-heidelberg.de/~robbers/cmbeasy/`.

[85] I. Foster, C. Kesselman, and S. Tuecke. The anatomy of the grid: Enabling scalable virtual organizations. *Intl. J. Supercomputer Applications*, 2001.

[86] O.S. Sazhina, M.V. Sazhin, V.N. Sementsov, M. Capaccioli, G. Longo, G. Riccio, and G. D'Angelo. Cmb anisotropy induced by a moving straight cosmic string. In *Quarks'08*, 2008.

[87] A. Achúcarro and C.J.A.P. Martins. Cosmic strings. astro-ph/0811.1277v1, 2008.

[88] A. Challinor and H. Peiris. Lecture notes on the physics of cosmic microwave background anisotropies. arXiv:0903.5158v1 [astro-ph.CO].

[89] D. Samtleben, S. Staggs, and B. Winstein. The cosmic microwave background for pedestrians: A review for particle and nuclear physicists. *Ann.Rev.Nucl.Part.Sci.*, 57:245–283, 2007. arXiv:0803.0834v1.

[90] R. Durrer. Cosmological structure formation with topological defects. astro-ph/0003363, 2000.

[91] M.B. Hindmarsh and T.W.B. Kibble. Cosmic strings. *Rept.Prog.Phys.*, 58:477–562, 1995. hep-ph/9411342.

[92] A. Kosowsky. *Modern Cosmology*, chapter The Cosmic Microwave Background. IOP Publishing, Bristol and Philadelphia, 2002. astro-ph/0102402v1.

[93] G. Riccio, G. D'Angelo, M.V. Sazhin, O.S. Sazhina, G. Longo, and M. Capaccioli. Simulations of cosmic strings signatures in the cmb. In *FINAL WORKSHOP OF GRID PROJECTS, "PON RICERCA 2000-2006, AVVISO 1575"*, 2008.

[94] M. Sakellariadou. *Quantum Simulations via Analogues: From Phase Transitions to Black Holes*, volume 718, chapter Cosmic strings, page 42. Springer Lecture Notes in Physics, 2008. arXiv:hep-th/0602276.

[95] M.V. Sazhin, O.S. Sazhina, M. Capaccioli, G. Longo, M. Paolillo, and G. Riccio. Gravitational lens images generated by cosmic string. in preparation.

[96] T. Vachaspati. Lectures on cosmic topological defects. hep-ph/0101270v2, 2001.

[97] T. Vachaspati and A. Vilenkin. Gravitational radiation. *Phys. Rev. D*, 31(12):3052–3058, 1985.

[98] J. Urrestilla and A. Vilenkin. Evolution of cosmic superstring networks: a numerical simulation. *Journal of High Energy Physics*, 02(037), 2008.

[99] G. Hinshaw, J.L. Weiland, R.S. Hill, N. Odegard, D. Larson, C.L. Bennett, J. Dunkley, B. Gold, M.R. Greason, N. Jarosik, E. Komatsu, M.R. Nolta, L. Page, D.N. Spergel, E. Wollack, M. Halpern, A. Kogut, M. Limon, S.S. Meyer, G.S. Tucker, and E.L. Wright. Five-year wilkinson microwave anisotropy probe (wmap) observations: Data processing, sky maps, and basic results. *ApJS*, 180:225–245, 2009. arXiv:0803.0732.